EMBRY-RIDDLE
Aeronautical University™
SCHOLARLY COMMONS

Dissertations and Theses

5-2015

Aerodynamic and Structural Design of a Winglet for Enhanced Performance of a Business Jet

Nicolas El Haddad

AERODYNAMIC AND STRUCTURAL DESIGN OF A WINGLET

FOR ENHANCED PERFORMANCE OF A BUSINESS JET

A Thesis

Submitted to the Faculty

of

Embry-Riddle Aeronautical University

by

Nicolas El Haddad

In Partial Fulfillment of the

Requirements for the Degree

of

Master of Science in Aerospace Engineering

May 2015

Embry-Riddle Aeronautical University

Daytona Beach, Florida

AERODYNAMIC AND STRUCTURAL DESIGN OF A WINGLET
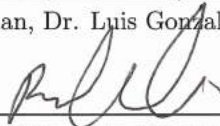# FOR ENHANCED PERFORMANCE OF A BUSINESS JET

by

Nicolas El Haddad

A Thesis prepared under the direction of the candidate's committee chairman, Dr. Luis Gonzalez-Linero, Department of Aerospace Engineering, and has been approved by the members of the thesis committee. It was submitted to the School of Graduate Studies and Research and was accepted in partial fulfillment of the requirements for the degree of Master of Science in Aerospace Engineering
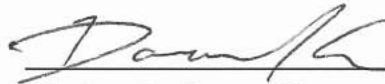
THESIS COMMITTEE

Chairman, Dr. Luis Gonzalez-Linero

Member, Dr. Reda Mankbadi

Member, Dr. Daewon Kim

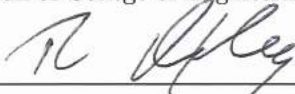Graduate Program Coordinator, Dr. Yi Zhao

4/17/15

Date

Dean of College of Engineering, Dr. Maj Mirmirani

4/17/15

Date

Associate VP for Academics, Dr. Robert Oxley

4-17-2015

Date

ACKNOWLEDGMENTS

TABLE OF CONTENTS

LIST OF TABLES

LIST OF FIGURES

SYMBOLS

a	Speed of sound
A	Cross sectional area
b	Wing span
c	Specific fuel consumption
C_{Do}	Parasite drag
C_{DoWL}	Parasite drag of the winglet
$C_{Dviscous}$	Parasite drag coefficient of the original aircraft, tail-off
C_f	Friction coefficient
C_L	Lift coefficient
C_{Lo}	Lift coefficient at zero° in angle of attack
d	Stiffeners flange width
$dC_L/d\alpha$	Lift curve slope
e_{min}	Minimum stiffener fastened flange width
E_t	Tangent modulus
g	Gravitational acceleration
h	Stiffeners height
I	Inertia
k	End fixity constant
K	Form factor
K_g	Dynamic gust alleviation factor
K_{WL}	Winglet form factor
L	Length
M	Mach number
n_{gust}	Sharp edge gust limit load factor
R	Range
$Re_{Winglet}$	Winglet Reynolds number
S	Surface area
S_{wet}	Winglet wetted area
S_{ref}	Winglet reference area
t	Thickness
u_τ	Friction velocity
U_{DE}	Derived equivalent gust speed
V_A	Design maneuvering speed
V_C	Design cruise speed
V_D	Design dive speed
V_{EAS}	Aircraft equivalent airspeed
W_G	Aircraft gross weight

y^+	Normalized wall spacing
α	Angle of attack
ϵ	Strain
μ_g	Mass parameter
μ_w	Dynamic viscosity at the wall
ρ	Radius of gyration
ρ_{SL}	Air density at standard sea level
ρ_w	Air density at the wall
σ	Normal stress
σ_{cr}	Critical buckling stress
σ_{max}	Maximum normal stress
σ_{ult}	Material tensile strength
τ_{max}	Maximum shear stress
τ_w	Viscous stress at the wall
$\varnothing_{rivet}$	Rivet diameter

ABBREVIATIONS

CFD	Computational Fluid Dynamics
FAR	Federal Aviation Regulations
FEA	Finite Element Analysis
FEM	Finite Element Method
KIAS	Indicated Airspeed in Knots
MTOW	Max Takeoff Weight
MZFW	Max Zero Fuel Weight
RANS	Reynolds Averaged Navier-Stokes
SA	Spalart-Allmaras
SFC	Specific Fuel Consumption
VLM	Vortex Lattice Method
WL	Winglet
WL1545	Winglet with 15% span and 45°cant angle

ABSTRACT

El Haddad, Nicolas MSAE, Embry-Riddle Aeronautical University, May 2015. Aerodynamic and Structural Design of a Winglet for Enhanced Performance of a Business Jet.

The preliminary design of a winglet to improve the range and fuel burn of the Falcon 10 business jet is presented. Twelve candidate geometries were studied varying the cant angle and the span. The configuration offering the best compromise between induced drag reduction, profile drag increase and weight increase due to the winglet structure and necessary wing structural reinforcement was selected. More refined analysis was performed for that winglet with Reynolds averaged Navier-Stokes computational fluid dynamics and finite element analysis. Range and fuel burn were finally calculated for a typical mission using these refined results. The selected winglet, with a span of 3.219 ft, a cant angle of 45º and a sweep angle of 40º increases range by 3.3% and saves about 3.8% of fuel on a 1200 Nm mission.

1. Introduction

1.1 Objectives

The goal of this project is to study the benefit of a wingtip device for retrofitting the Dassault Falcon 10. The expected benefits are an increased range and lower fuel burn. Well designed winglets reduce drag at high and low speeds, potentially allowing shorter takeoff distances, reduced takeoff noise, increased range and cruise speed. This design is the result of the compromise between the reduction in induced drag and the increase in profile drag and structural weight. Winglets constitute a relatively low cost alternative for improving an aircraft performance, particularly compared to other solutions such as engine upgrades.

1.2 Baseline Aircraft. Dassault Falcon 10

The winglet in this thesis is proposed for the Dassault Falcon 10 that entered into service in 1973 (*Mystère-Falcon 10-100*, 2015). It has a ceiling of 45,000ft and a maximum operating Mach number of 0.87. Its range is 2000 Nm carrying four passengers at Mach 0.75 and an altitude of 35,000 ft without fuel reserves (Avions Marcel Dassault - Breguet Aviation, 1993).

A total of 226 Falcon 10 and Falcon 100, a variant of the Falcon 10, were produced between 1973 and 1989 (*Mystère-Falcon 10-100*, 2015) of which about 140 are still active today (M. Lavanant, personal communication, April 16, 2015). Table 1.1 presents a summary of the aircraft design weights and the geometry is shown in Figure 1.1.

Table 1.1. Summary of Falcon 10 weights

Max. Takeoff Weight	18300 lb
Max. Zero Fuel Weight	12460 lb
Min. Flight Weight	9920 lb
Typical Empty Weight	11460 lb

1.3   Induced Drag and Wingtip Devices

1.3.1   Review of Induced Drag

Induced drag is caused by the generation of lift. A wing generates high pressures on its lower surface and low pressures on its upper surface. The resultant of those pressures is an upward force. However, because of that pressure differential, a swirling motion is established at the tip with air moving from the high pressure region towards the upper surface. This movement combined with the streamwise velocity of the air, and amplified by the downwash generated by each wing section along the span, generates vortices emanating from the tips and trailing streamwise. A spanwise velocity component is created all along the wing, oriented from root to tip on the
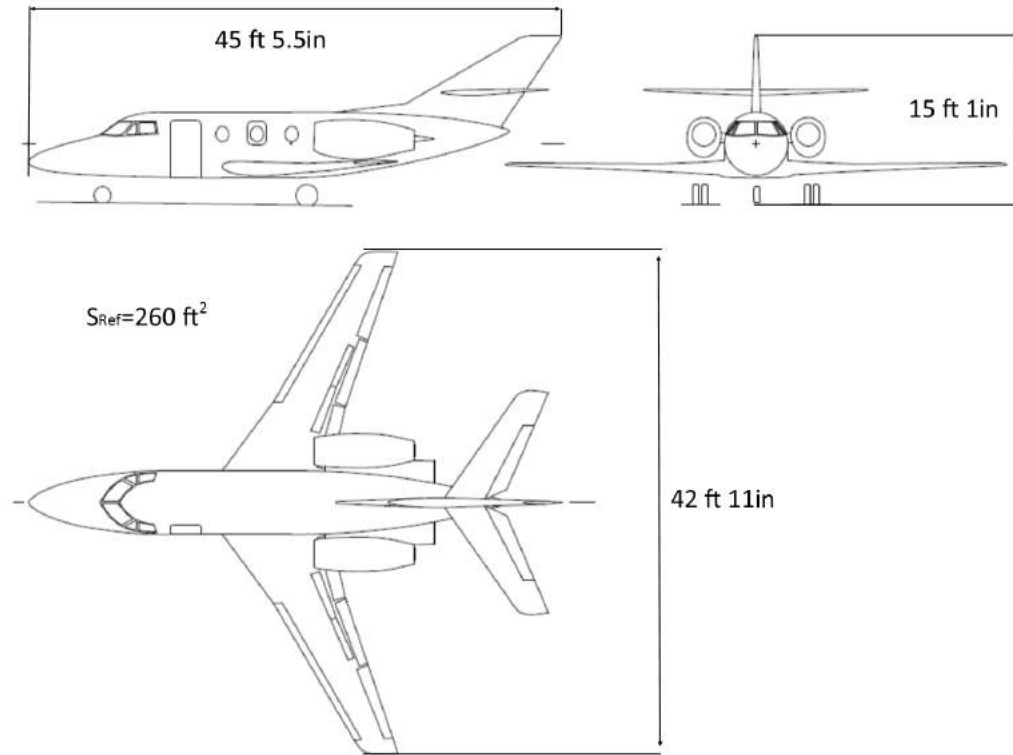
Figure 1.1. Dassault Falcon 10 3-view drawings

lower surface and from tip to root on the upper surface. The resulting discontinuity in spanwise velocity between the upper and lower surfaces of the wing creates a thin shear layer behind the wing called vortex sheet, which will end up rolling around the tip vortices, feeding them with additional vorticity.

The tip vortices affect the motion of the entire flow field around the wing, thus modifying the pressure field around it, and as a result, the aerodynamic forces acting on it. A downward velocity component is generated along the wingspan, locally changing the effective angle of attack and tilting the lift vector backwards, therefore

the effective lift vector has a component in the direction of the freestream velocity, which is known as the induced drag or lift dependent drag.

It is possible to calculate the induced drag from the integration of the flow velocity distributions on a plane far downstream perpendicular to the flow direction known as the Trefftz plane. At a given lift coefficient, the induced drag is a function only of the aspect ratio, or more generally of the shape of the trailing vortices wake and of the spanwise lift distribution. As the aspect ratio increases, the wing gets closer to an ideal infinite span wing for which the induced drag is zero. The spanwise lift distribution is related to the induced angle of attack and thus to the induced drag. For a planar wing, the minimum induced drag is obtained when the spanwise lift distribution is elliptical (Anderson, 2011). However, the total drag includes also the parasitic drag, a function of the wetted area, pressure drag and wave drag. Thus induced drag can be reduced with higher aspect ratios, however that increases the profile drag and will also result in higher bending moments that may require structural reinforcements, hence higher weights adversely affecting the overall aircraft performance.

Accordingly the aircraft range and fuel burn will only be improved with a compromise of all these competing effects.

1.3.2 Different Wingtip Devices and their Effect on Induced Drag

Over the last decades, engineers have dealt with the problem of induced drag reduction by designing various types of wingtip extensions. Some attempts were first made by adding vertical flat plates at the wingtip with the intention of preventing

the tip vortices formation. However, any induced drag reduction produced, mostly at high lift coefficients, was compensated by a large increase in friction drag near cruise conditions giving a zero net improvement or even a total drag increase (Whitcomb, 1976).

Whitcomb set a benchmark in the design of wingtip devices by adding two nearly vertical small wings to the tip of a wing, one upwards and the other downwards as shown in Figure 1.2(a). Contrary to vertical end-plates, winglets are designed to generate a normal force inward and affect the overall lift distribution along the wingspan. The winglet can be considered as a non-horizontal wing span extension, that, in addition to increasing the effective aspect ratio, allows tailoring of the span-wise lift distribution making it closer to ideal, thereby reducing induced drag. The ideal spanwise lift distribution for such a configuration is different from the elliptic lift distribution, ideal for a planar wing, and several authors (e.g., Kroo, 2005; Cone, 1962) have focused on its calculation for non-planar wing configurations, showing the benefit of a non-planar tip extension.

As a general rule, the larger the length of the added device, the larger the reduction in induced drag but that improvement is partially limited by the increase in other drag components such as viscous or wave drag. Moreover, the addition of a wingtip device increases the structural loads, in particular the bending moments, resulting in added weight due to the necessary wing reinforcement, in addition to the winglet weight itself.

(a) Whitcomb style winglets on the MD-11 (Picture by Phil Rademacher, reproduced with permission).
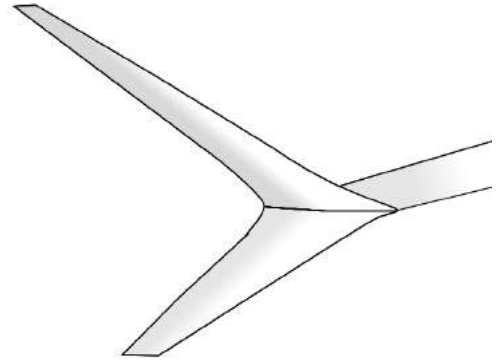
(b) Boeing 737 Max Advanced Technology Winglets.

(c) Falcon 2000S blended winglet (Picture by author).

(d) Airbus A320 wingtip fence (Wikimedia Commons, 2014).
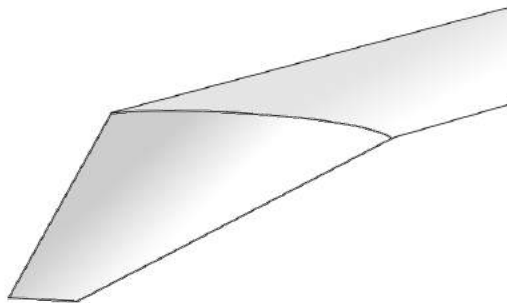
(e) Anhedral winglet.

(f) Boeing 777 raked wingtip (Picture by Phil Rademacher, reproduced with permission).

Figure 1.2. Different wingtip extensions.

Whitcomb's winglet was used as a reference for retrofit of the DC-10. The lower part was initially designed to reduce the induced velocities on the upper winglet in order to minimize the undesirable effects of the interference between the wing and winglet (Whitcomb, 1976). This effect was verified during wind tunnel and flight tests. However, it was also found that the lower winglet encountered stall at lower lift coefficients than the rest of the wing, which propagated to the upper winglet, thus mitigating its beneficial effect (Shollenberger, Humphreys, Heiberger, & Pearson, 1983; Taylor, 1983).

More recent aircraft feature split winglets such as the Boeing 737 Max equipped with Advanced Technology Winglets (Figure 1.2(b)) or Split Scimitar Winglets. When properly designed, split winglets can produce up to 90% of the induced drag reduction of a single winglet of the same height for half the wetted area (McLean, 2005).

Blended winglets are used on several current civil and business aircraft such as the Boeing 737 NG, Airbus A320, Hawker 800, Falcon 2000, etc. The use of a large smooth fillet between the wingtip and winglet root (Figure 1.2(c)) reduces the induced drag benefit compared to a sharp canted winglet (McLean, 2005) but the benefits in terms of viscous drag and reduced interference compensate that shortfall (McLean, 2005; Thomas, 1985).

Another type of wingtip device is a highly swept and tapered planar tip extension (raked wingtip) such as used on the Boeing 777 (Figure 1.2(f)). As noted earlier, the use of a winglet has an effect similar to that of increasing the wing span of an aircraft. According to McLean (2005), a horizontal tip extension offers twice as much reduction

in induced drag as a vertical extension of the same size but adding nearly twice as much weight to the wing structure. Van Dam (1987) showed that for a planar wing with elliptical lift distribution, the induced drag can be further reduced by gradually sweeping the wing aft in a crescent-moon-like shape. The raked wingtip combines that effect with an increased wing aspect ratio. The use of horizontal tip extensions is limited in practice due to airport compatibility considerations and in general, it is not the preferred option for retrofit because it is likely to require significant structural reinforcement.

Recent works have studied the effects of large anhedral winglets alone (Figure 1.2(e)) showing that they can produce similar drag reductions to that of large upper winglets with lower bending moments (Mann, 2006). However, as with Whitcomb, problems with separation were encountered at low speeds (Büscher, Streit, & Rohardt, 2006) and also ground clearance is problematic with this configuration.

C-shaped winglets were inspired by research on box wings. Kroo (2005) showed that when the horizontal span of a wing is limited, the configuration leading to the minimum induced drag is a box plane but this configuration produces an important friction drag due to the wetted area. In contrast, a C-shaped wing-winglet achieves similar induced drag reductions to those of the box plane but for a much lower wetted area. Furthermore, the optimal lift distribution for a C-shaped wing corresponds to a downward lift component on the winglet horizontal extension, and therefore lower bending moments. However, the presence of two corners suggests possibly significant interference which would mitigate the achievable drag benefits. Moreover,

this configuration presents bad aeroelastic properties that could result in an increase in weight. The significant changes in the wing structure, that a C-winglet would require, prevent it from consideration for retrofit of an existing aircraft.

The wingtip fences (Figure 1.2(d)) are smaller devices, whose effect on aircraft drag is small compared to larger winglets but the increase in bending moment is also reduced such that structural reinforcement is minimized. Therefore, they are particularly good candidates for the retrofit of an existing aircraft. Wingtip fences generate a side force by the development of a leading edge vortex due to their high sweep angle (similar to a delta wing). Wingtip fences can reduce aircraft drag in cruise by 1.5% (Poisson-Quinton, 1985). More recent research proved that using a small downward pointing winglet could further improve the aircraft take-off lift to drag ratio by 2% with similar cruise performance and structural impact (Mann, 2006).

1.4 Winglet Geometry for the Falcon 10

The previous chapter introduced the necessary tradeoff to be made between drag reduction and weight increase, when designing a wingtip device. It was noted that wingtip fences are interesting for retrofit due to their low weight penalty but they can only achieve small drag reductions. Dassault, together with other sources (Huber, 2012), suggests that the Falcon 10 may have non-negligible structural margins that would allow larger wingtip devices to be installed. However, the aft-swept low wing present on this aircraft greatly limits the use of a downward pointing device because

of ground clearance. The use of a blended type winglet then appeared as a good choice due to its simplicity and to the fact that this concept has been successfully used for many aircraft, including other Falcon aircraft. That type of Wingtip device was hence considered in this work.

Whitcomb (1976) defined a set of good aerodynamic practices for the design of an effective winglet. Those rules were used as a reference for the winglets tested in this work. Details of the winglet geometries considered are given next.
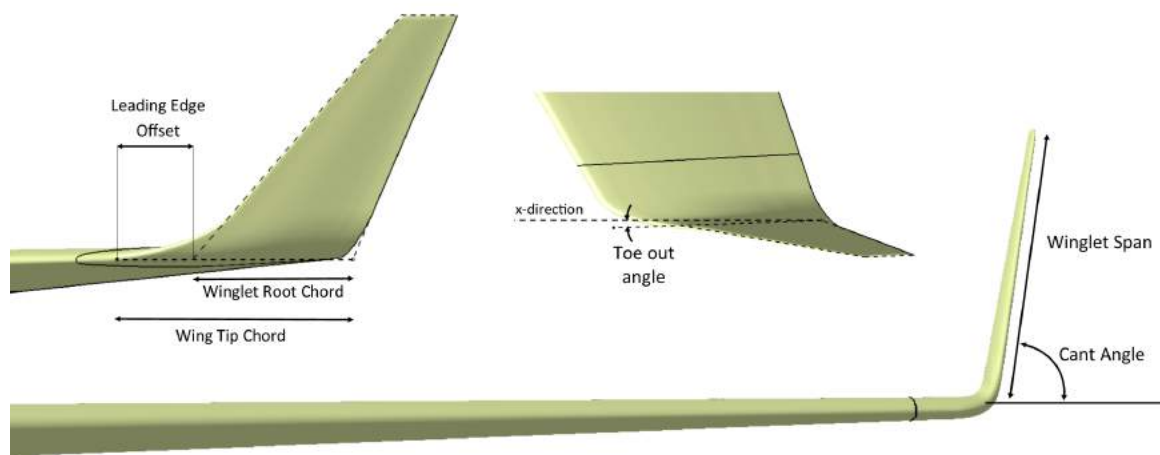
Figure 1.3. Winglet geometry parameters

1.4.1 Planform

For aerodynamic efficiency, the winglet must be tapered in the same way a wing would be (Whitcomb, 1976). A taper ratio of 0.35 was selected based on Figure 1.4, for minimum induced drag. The winglet sweep must be similar to that of the original

wing in order not to alter its effectiveness in the transonic regime. A leading edge sweep of 40° was selected (i.e. slightly higher than the 30.5° outboard sweep of the original wing).
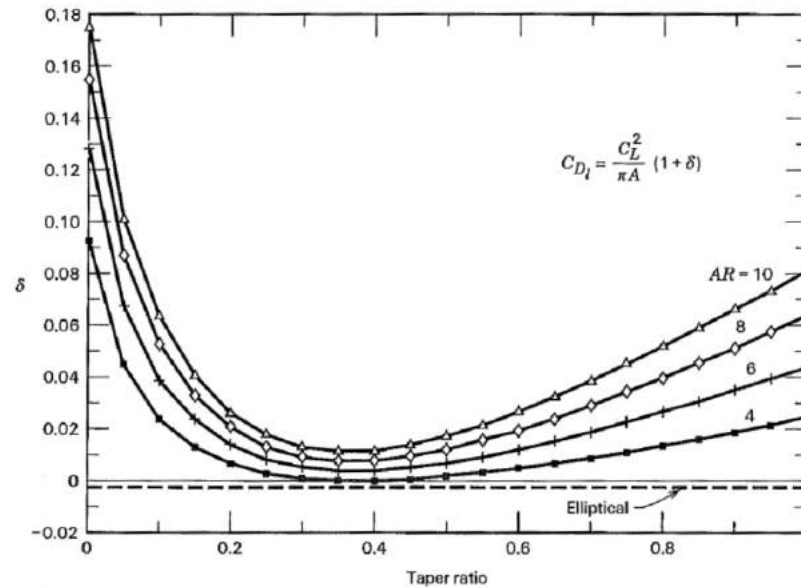
Figure 1.4. Induced drag factor for elliptic and linearly tapered wings (McCormick, 1995).

1.4.2 Position and Chord

The induced drag depends only on the lift distribution in the spanwise direction. According to Munk's stagger theorem (Munk, 1921), shifting the winglet longitudinally does not affect its potential induced drag reduction. To maintain the lift distribution unchanged it may be necessary to adjust parameters such as the twist angle. Thus the use of a winglet with a root chord smaller than the wing tip chord allows the same induced drag reductions as full chord winglet for a smaller added

wetted area, provided the lift distribution remains unchanged. In fact, a full chord winglet may produce detrimental interference effects; the superimposition of the low pressure region over the wing with that over the winglet leads to an early formation of shockwaves, increasing wave drag. Shifting the winglet leading edge aft, the two low pressure regions are separated, thus reducing the detrimental interference effects and avoiding shockwaves. The winglet trailing edge is placed coincident with the wing trailing edge such that there is no discontinuity in the flow.

1.4.3   Blending

The benefits of using smooth fillets at the winglet root were presented in section 1.3 of this thesis. Smooth fillets were used in the winglets designed for this study.

1.4.4   Incidence and Twist

Because of the inflow angle at the upper wingtip, the winglet must be toed out in order to reduce its effective angle of attack. The optimal toe out angle depends on the inflow angle at the tip and on the required winglet angle of attack for optimal spanwise lift distribution, corresponding to the minimum induced drag. The inflow angle is reduced as we move outboard along the winglet span, thus providing some aerodynamic twist. Additional twist can be added to the winglet in order to achieve a desired lift distribution but is not generally required Whitcomb (1976). Optimization of the winglet toe out angle and twist to achieve the optimal lift distribution was not

considered in this study. The Boeing 737NG, winglets were first designed without toe out angle, which resulted in high induced drag reductions but high bending loads. The winglet was later toed out 2º to reduce the loads, this increased the induced drag but decreased other drag components such as wave and profile drag, compensating the induced drag benefit loss (Faye, Laprete, & Winter, 2002). For this work, no geometric twist was imposed and a toe out angle of 2º was set.

1.4.5   Airfoil

The winglet airfoil must provide the required normal force coefficients for optimal spanwise lift distribution without causing flow separation before the original wing does. Additionally, the Falcon 10 cruises at high subsonic speeds and is hence sensitive to the formation of shock waves and its associated wave drag. The winglet airfoil described by Whitcomb (1976) was designed for such operating conditions and is similar to the wingtip airfoil of the Falcon 10. Whitcomb states that to meet the requirements stated earlier, the winglet airfoil camber must be significantly greater than the wing tip airfoil camber. The Falcon 10 wingtip airfoil was hence used for the winglet, with a camber increased to 2.4% as done by Whitcomb.

1.4.6   Size and Cant Angle

Size and cant angle are two of the parameters having the greatest impact on the winglet performance (e.g., Rademacher, 2014; Takenaka, Hatanaka, Yamazaki,

& Nakahashi, 2008). Larger winglets achieve higher induced drag reductions but at the cost of increased friction drag and higher bending moments. As Takenaka et al. (2008) showed, high cant angles lead to increased interference and hence increased wave drag, even when blending is present but they reduce the wing bending moments, hence the weight. On the other hand, low cant angle winglets add to the total lift and hence allow the aircraft to fly at a lower angle of attack thereby reducing its induced drag but at the cost of higher bending moments. The choice of these two parameters results from a tradeoff between different drag components and structural weight.

1.5   Scope of the Study

Rademacher (2014) systematically studied the effect of certain design parameters such as cant angle, sweep angle, taper ratio and span on the performance of winglets for the Falcon 10, albeit with low fidelity methods, in particular, VLM and handbook calculations. However, important effects were left out (shockwaves, viscous effects, structural reinforcement weight) due to limitations of the tools used.

For this thesis, the performance of the aircraft is determined taking into account the aerodynamic and weight effects of the winglet. A literature review allowed to narrow down the winglet design space. A blended winglet inspired by the Whitcomb winglet geometry was considered, with various cant and span angles within a practical range. VLM provided estimations of the effect of winglets on the aircraft drag, for screening purposes. The winglet weight was estimated in a simplified manner using available data, and wing reinforcement was calculated using finite element analysis

(FEA) to estimate the total added weight. Reynolds Averaged Navier-Stokes (RANS) Computational Fluid Dynamics (CFD) simulations were used to accurately estimate aerodynamics of the best winglet, including the effects of shock waves, viscosity and interferences. Aircraft range and fuel burn were finally calculated for a specified mission.

The winglet design approach presented in this thesis does not rely on multidisciplinary design optimization. Changes in the aircraft's flutter characteristics, fatigue, and trim drag were not considered.

2. Methodology

Twelve winglet configurations were considered with cant angles ranging from 45º to 80º, and with winglet spans of 10%, 15% and 20% of the baseline wing semi-span (Figure 1.3). A different value of the offset between the leading edge of the wing tip and leading edge of the winglet was set for each winglet size in order to keep the aspect ratio of the winglet higher than 3.7, as presented in Table 2.1.

Table 2.1. List of winglet parameters used in this study.

Cant Angle	45º	60º	70º	80º
Winglet Span (ft)	2.146	3.219	4.291	
Percentage of Wing Span	10%	15%	20%	
Leading Edge Offset (ft)	1.362	0.984	0.656	
Winglet Aspect Ratio	3.7	4.6	5.3	
Taper Ratio	0.35			
Leading Edge Sweep	40º			

Wind Tunnel and CFD calibrated VLM models were used to quantify the change in lift and induced drag for each winglet configuration, while the change in parasite drag was computed using handbook calculations calibrated with CFD results. The added weight was estimated for every winglet using empirical calculations and finite element simulations. The best winglet was selected and polars were determined using

CFD simulations to finally evaluate its effect on aircraft range and fuel burn, for a specific mission. Details of the different steps are presented here.

2.1 Prediction of the Aircraft Aerodynamic Characteristics

Wind tunnel results for the Falcon 10 at high subsonic speeds were provided by Dassault, but reproducing such wind tunnel experiments for every winglet configuration would be costly, both in terms of time and money. Reliable lift and induced drag estimations can be obtained within minutes using the vortex-lattice method, provided the model is calibrated. However, VLM assumes inviscid potential flow and is hence unable to calculate viscous and wave drag. RANS simulations were used in addition to the VLM results to accurately determine the drag polars, with winglets, incuding the effects of viscosity and shock waves. The different aerodynamic models used in this work are described in the next sections.

2.1.1 Computational Fluid Dynamics Analysis

The aircraft wing aerodynamics were studied using RANS simulations in ANSYS Fluent®. The study of the entire aircraft was initially considered because of the availability of wind tunnel results for validation. However, due to the high memory requirements, the problem was reduced to the study of the wing only. This introduces some discrepancy at the root as shown in figure 2.1 but it can be assumed that the fuselage has minimal effect on the flow near the wingtip and that its aero-
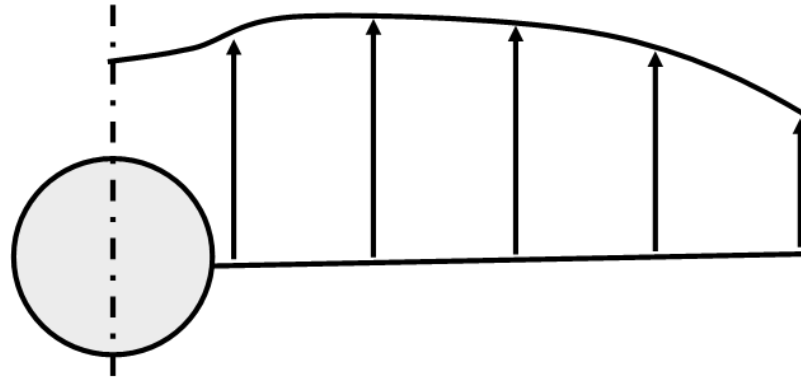
(a) Spanwise lift distribution, in presence of the fuselage (qualitative)
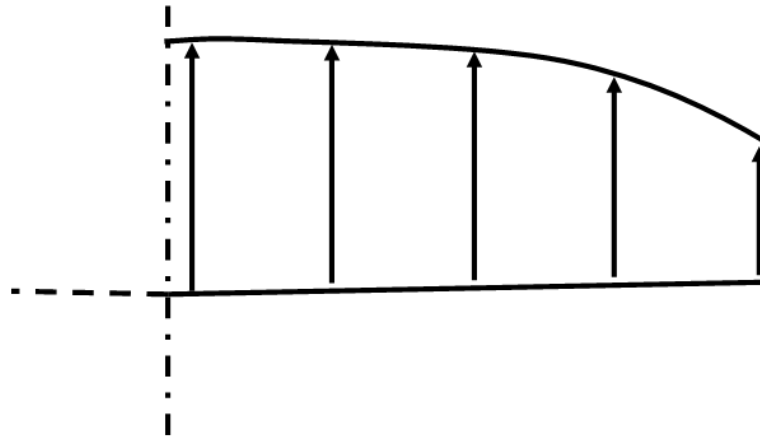
(b) Spanwise lift distribution, without the fuselage (qualitative)

Figure 2.1. Effect of the boundary conditions on the spanwise lift distribution.

dynamic contribution remains unchanged as the winglets are added, thus justifying this simplification.

The baseline wing geometry was modeled and a grid independence study was performed and validated with respect to the wind tunnel data (see section 3.1). Simulations were then run to determine the lift and drag at different angles of attack and Mach numbers. The spanwise lift distribution was extracted and used for calibration of the wing VLM model described in section 2.1.2.

A winglet configuration was arbitrarily chosen within the design space and analyzed at the same angles of attack and Mach numbers as the baseline wing for calibration of the winglet calculations in the VLM model. The results of these simulations were also used to derive a correction factor for the friction drag estimations as it will be explained later.

The design space exploration was carried out with the VLM code because of its quick turnaround time and adequate accuracy once it had been calibrated with regard to the wind tunnel and the RANS results. The VLM results were used together with the weight calculations to find the best candidate. Once it was identified, that configuration was analyzed with RANS at the same angles of attack and Mach numbers as the baseline wing to generate new polars for the aircraft with winglets for the range calculations (see section 2.4).

All physical conditions simulated in ANSYS Fluent® involve symmetrical flow (zero sideslip angle), hence only the left wing was modeled. A symmetry boundary condition was applied at the intersection between the wing and the fuselage ("external root"). An adiabatic, no slip boundary condition was set at the wing surface. Mach number, static pressure and temperature were imposed at the far field through the use of a pressure far-field boundary condition.

The RANS approach relies on the assumption that every variable describing the airflow (e.g., density, velocity, etc.) can be separated into an average term and a fluctuation term. The average flow field is solved and the effect of the fluctuations on the average flow field is buried into the turbulence model equations. For this study,

air was modeled as an ideal gas, viscosity was set as a function of temperature using Sutherland law, and the energy equation was enabled to account for compressibility effects. The 1-equation Spalart-Allmaras turbulence model was used initially during the grid convergence study but the 2-equation $k - \omega$ SST model was later used due to its better accuracy in predicting boundary layers and separation.

The Fluent® second order implicit density based solver was used. For convergence acceleration, a full multigrid initialization was performed for each simulation and a pseudo-time stepping approach was used.

2.1.2 Vortex Lattice Method

The VLM method allows fast estimation of lift and induced drag and was hence a useful tool for this study. However, it does not compute parasite and wave drag. All the VLM simulations run in VLAERO® include a Prandtl-Glauert scaling to account for the effects of compressibility on the aerodynamic forces. The different models used in this work and the results obtained are presented next.

Wing Model

Accurate induced drag prediction requires an accurate estimation of the spanwise lift distribution, which could not be determined from the available wind tunnel results, but could be extracted from the RANS results. Therefore, a first VLM model was created for the same geometry as the one modeled in Fluent®, that is to say only

the wing with a symmetry boundary condition at the external root, and calibrated with respect to the RANS results. The planform of the original wing was reproduced, separated into different parts at the location of the airfoils A to D (see Figure 2.2). Camber and twist were applied to these airfoil sections.
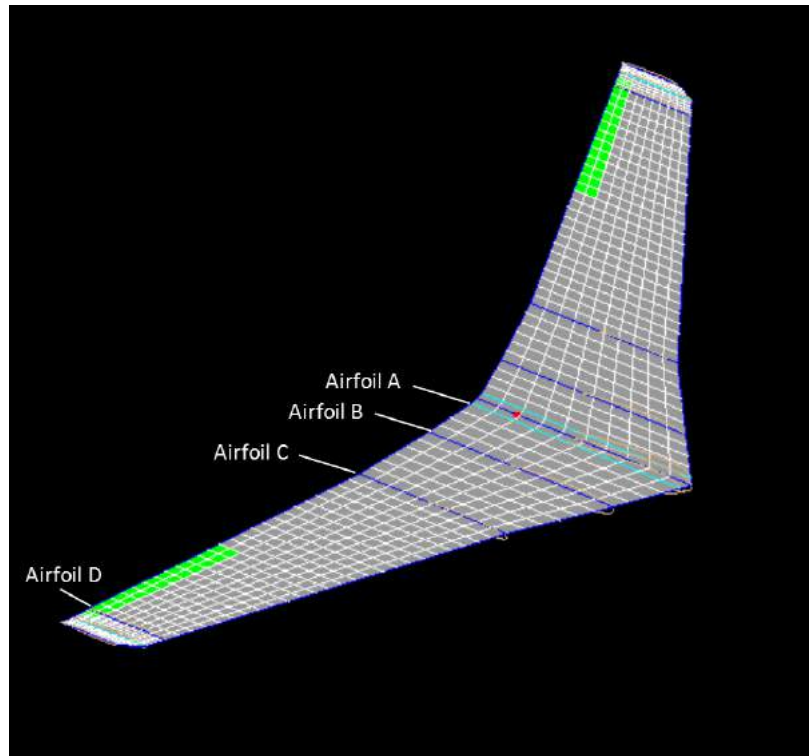
Figure 2.2. Wing VLM model.

The lift and the induced drag of the wing were calibrated to match the CFD results at Mach 0.7. Circulation and incidence correction factors were applied to each part of the wing to reproduce the same lift contribution for each section as the one from RANS. VLAERO® uses the Trefftz-plane theory introduced in section 1.3 to calculate induced drag and a calibration factor ("Trefftz factor") of 1.2 derived in previous work (Rademacher, 2014) also showed good results in this study.

Once the calibration of the baseline wing model was carried out, the geometry of the winglet 1570 (15% span, 70 cant) was created in VLAERO® and added to the wingtip. For consistency with the results on the baseline wing, the calibration factors for the rest of the wing were kept unchanged and the same Trefftz factor of 1.2 was used.

Full Aircraft Longitudinal Model

After the wing was calibrated against the CFD results, the fuselage and engine nacelles were added to the VLM model. This model can also be used for calculations of the trim angle of attack and the trim drag, provided the horizontal tail is added and calibrated. The latter could not be done in this thesis due to the time constraints, however, the full aircraft VLM model drag polars were used for the winglet selection. For calibration, simulations were run at different angles of attack and Mach numbers and the results were compared to the wind tunnel results for the tail-off aircraft.

Simulations were run for different angles of attack, at Mach 0.7 and Mach 0.8, for the 12 candidate winglet configurations, using the calibrated models, to produce the drag polars for the aircraft with and without winglets.

Full Aircraft Lateral Model

The longitudinal model presented before was used for simulating symmetric conditions. For the determination of the loads for a sideslip condition, a different model
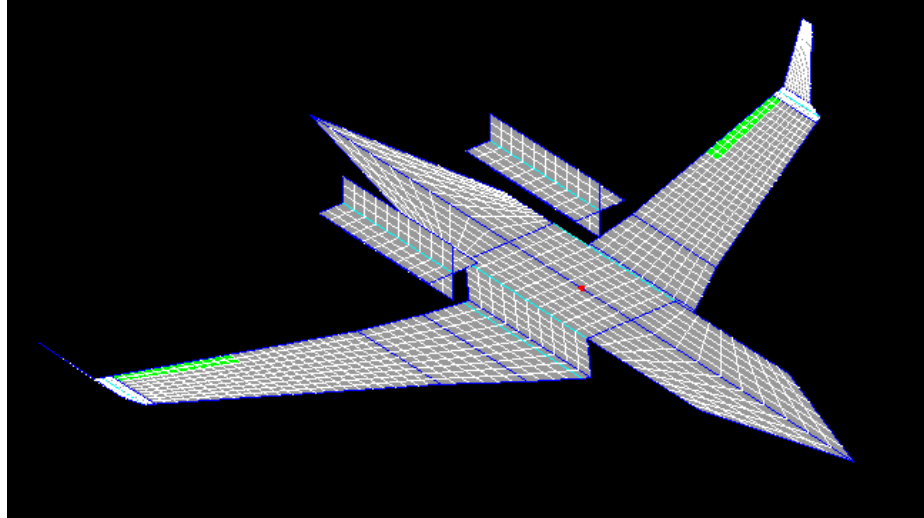
Figure 2.3. Entire aircraft longitudinal VLM model.

was constructed (Figure 2.4). It can also be used for estimation of the aircraft lateral and directional stability. Since no data was available for calibration of this model, the calibration factors determined earlier for the wing, fuselage and nacelles were also used for the lateral model as well.

2.1.3 Parasite Drag Model

The VLM assumes inviscid flow, therefore the parasite drag needs to be estimated separately. For clarity and ease of calculation this term can be broken into two components, the baseline aircraft parasite drag and that of the winglet.

The fuselage and baseline wing parasite drag, $C_{Dviscous}$, was simply estimated by subtracting the VLM predicted induced drag from the total drag determined by wind tunnel tests. It is a function of the angle of attack.
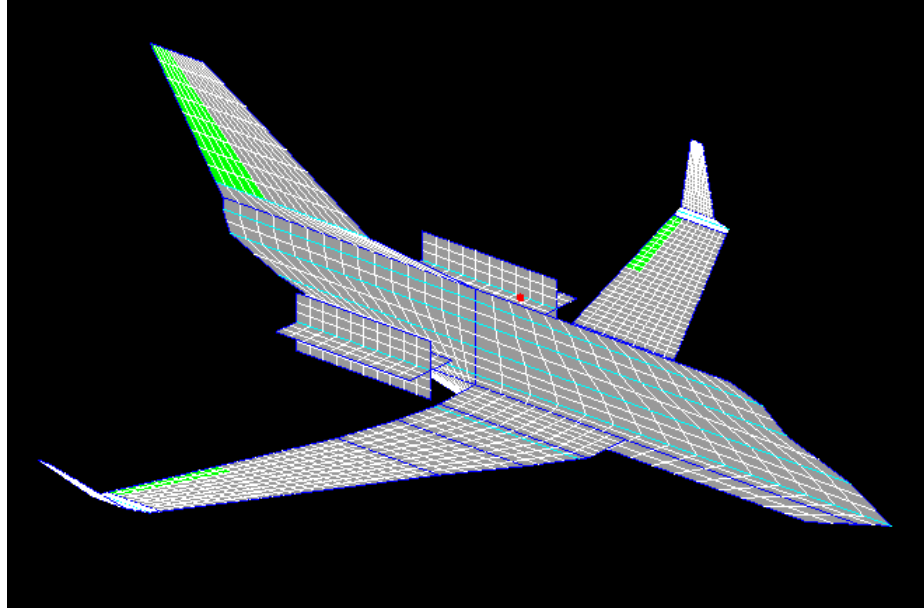
Figure 2.4. Entire aircraft lateral VLM model.

The second term is the winglet's contribution to the total parasite drag due to the added wetted area. It was calculated using a traditional drag buildup method (Bertin & Cummings, 2014):

$$C_{DoWL} = K.C_f.\frac{S_{wet}}{S_{ref}} \qquad (2.1)$$

where K is a form factor including the effect of airfoil thickness and winglet sweep, the friction coefficient C_f is calculated assuming a fully turbulent boundary layer by

$$C_f = \frac{455}{\log\left(Re_{Winglet}\right)^{2.58}} \qquad (2.2)$$

where $Re_{Winglet}$ is the Reynolds number based on the mean aerodynamic chord of the winglet.

If the winglet is to be retrofitted, part of the original wingtip will be removed to be replaced by the winglet and the drag contribution from the removed wingtip can be estimated, using equation 2.1. The net effect of the winglet on the parasite drag is then:

$$\Delta C_{DoWL} = C_{DoWL} - C_{Do\ removed\ tip} \tag{2.3}$$

The results of equation 2.3 were calibrated with respect to the RANS calculations and a correction factor of 2.5 was added such that:

$$\Delta C_{DoWL} = 2.5 \times \left(K_{WL}.C_f.\frac{S_{wet\ WL}}{S_{ref}} - K_{removed\ tip}.C_f.\frac{S_{wet\ removed\ tip}}{S_{ref}} \right) \tag{2.4}$$

The total drag was then calculated using the VLM induced drag $C_{Di_{VLAERO}}$ by:

$$C_{D_{tot}} = C_{Di_{VLAERO}}(\alpha) + C_{Dviscous}(\alpha) + \Delta C_{DoWL} \tag{2.5}$$

2.2   Estimation of the Added Weight

The winglet results in a net weight increase due to its own structure plus the wing structural reinforcement required to sustain the increased loads. The estimation of these two components is presented here.

2.2.1 Winglet Weight

The detailed structural design of the winglet was beyond the scope of this work. However, published data exists for the Hawker 800 and the API winglet for the Boeing 737 NG. For the latter, the weight given was 300 lbs with 75% being the winglet structure (McLean, 2005). For the Hawker, whose size, mission, and therefore design parameters are close to the ones considered here, the weight increase was 115 lbs (*Hawker 800SP & Hawker 800XP2*, 2014). Thus, scaling by planform area and assuming only 75% of the total Hawker added weight, a rough winglet weight can be estimated by:

$$W_{Winglet\ i} = W_{Winglet\ Hawker\ 800}\ \left(\frac{S_{Winglet\ i}}{S_{Winglet\ Hawker\ 800}} \right) \qquad (2.6)$$

2.2.2 Structural Reinforcement Weight

Data was available about the Falcon 10 wingbox structure (Avions Marcel Dassault - Breguet Aviation, 1972) and, therefore, it was possible to determine whether there were sufficient structural margins or whether extra reinforcement was needed. A finite element model of the wingbox was created and calibrated with respect to Dassault's wingbox stress analysis report (1972). The model was used for a set of critical loads with the different winglets. For every winglet configuration, the VLM models were run at these critical conditions and the pressure distributions obtained were used as input for the FEM model. The stresses were calculated and stiffen-

ers were added wherever it was necessary to provide positive margins of safety, for buckling and static strength.

Critical Loads

The baseline wingbox was sized to resist two specific load conditions (Avions Marcel Dassault - Breguet Aviation, 1972): an upward gust condition, critical for the inboard part of the wing and a roll condition, critical for the outboard part of the wing. The stress report provided shear force and bending moment diagrams for each of these conditions in the deformed wing shape.

An additional loading case was studied, corresponding to a sideslip maneuver. Since the maximum symmetric maneuvering load factor was lower than the maximum gust load factor, it was not considered in this study.

Gust Condition The upward gust condition used in Dassault's structural analysis report corresponds to a net load factor of 5, including the lift minus the wing inertia relief. This load factor occurs at an angle of attack of 8° at Mach 0.84 (M_C) and an altitude of 23000 ft (maximum gust load factor altitude according to Torenbeek's gust load factor estimation approach (2013))

Roll Condition For the roll condition, the FAR, Part 25, specify that the aircraft must be able to reach the same roll rate when flying at V_C as it would have with a full aileron deflection at V_A, the design maneuvering speed. Moreover, the aircraft must be able to withstand this roll rate when flying at a load factor of two thirds of the

maximum maneuver load factor, i.e. 2. The ultimate loads are then determined by multiplying the limit loads by a factor of 1.5. The ultimate loads in the deformed wing shape, given in the structural report (Avions Marcel Dassault - Breguet Aviation, 1972) were approximated in this study by applying a factor of 1.1 to the aerodynamic loads occurring for max aileron deflection at V_C for a load factor of 2, at 10000 ft (maximum dynamic pressure at V_C), at MTOW. Inertia relief due to the wing weight and fuel weight at a load factor of 2 were also considered.

Sideslip Condition The FAR, Part 25, specify that the aircraft must be able to withstand loads resulting from a full rudder deflection during unaccelerated flight at speeds from V_{MC} to V_D. Although this sideslip maneuver condition is in general not critical for a wing, the presence of close to vertical winglets at the tip can result in high bending moments that may cause those maneuvers to become critical (Faye et al., 2002).

The equilibrium sideslip angle of $\pm 16.5^{\circ}$ resulting from a full rudder deflection ($\pm 35^{\circ}$) at V_D was determined using the lateral VLM model described in section 2.1.2. The weight considered for this loading case was the MTOW at the altitude corresponding to the maximum dynamic pressure at the design dive speed. These conditions result in the highest pressure loads on the wing. The angle of attack associated with level flight in these conditions is 2°. The wing structure and its fuel weight were added to the pressure loads and the total loads were finally multiplied by 1.5 to represent the ultimate sideslip loading conditions.

Baseline Wing Structure

A model of the wing structure was created in CATIA®, based on the data made available by Dassault, comprising the wing skin, 19 ribs, a front, mid and rear spar and a tip fairing.

As shown in Figure 2.5, the front and rear spar both extend from the center wingbox attachement to rib 16, whereas the mid-spar extends only to rib 3. The front and mid-spars are attached to the center wingbox. The rear spar is attached to the mid spar through ribs 2 and 3. Details of the attachment at the root and between
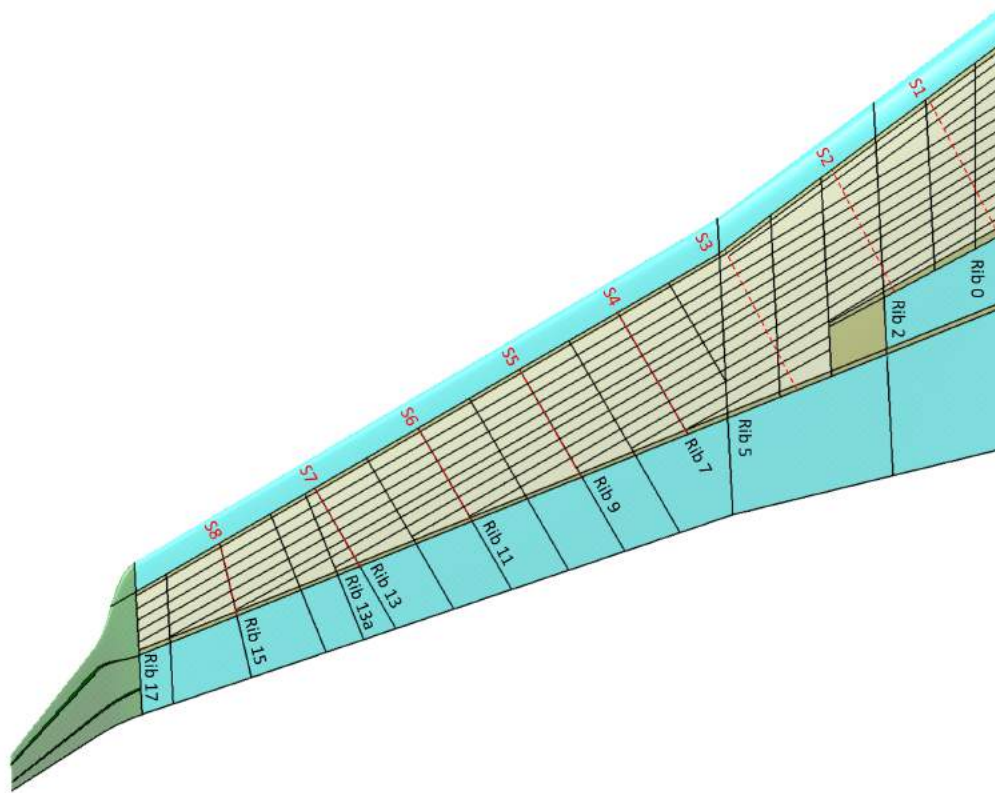
Figure 2.5. Diagram of the wing structure.

the aft spar and mid spar were not available for this study. However, it appears that rib 2 and 3 were reinforced for proper load transfer. To account for this fact, ribs 2 and 3 were thickened in the FEM.

The wing comprises a wingbox (made up by the spars, ribs and skin), which is the principal load bearing element, plus a leading and trailing edge. The wingbox has a cutout on its lower skin for the landing gear, delimited by the rib 0, rib 2 and the mid and aft spars for the landing gear.

The wingbox skins are reinforced by integrally machined stiffeners. Not all of them extend the entire wing span. The skin thickness is increased at each stiffener end to avoid stress concentrations. However, for the sake of simplicity, this was not modeled in the current study and in the model the stiffeners were ended at their intersection with the closest rib. The stress concentrations in the simulations due to these stiffener endings were disregarded. The spar caps were modeled as a skin of increased thickness.

The leading and trailing edges were modeled as simple surfaces having 80% of the thickness of the wingbox skin. This was done to appropriately transfer the whole wing aerodynamic loads into the wingbox (which is the main load bearing element). With this arrangement the FEM was not overstiffened and also the leading and trailing edge skins did not present unrealistically large deformations.

Most of the ribs were only modeled from front to rear spar. The ribs between the kink and the wing tip (5 to 16) were extended until the trailing edge to allow more realistic load transfer to the wingbox for the case of a roll maneuver.

The wingtip and the winglets were modeled with three internal spars: two of them being coincident with the front and aft spars of the wing and the last one further aft. These parts were meshed for the analysis but without intending to represent the actual structure of the winglets. The stress values in these regions were disregarded. The only purpose of their modeling was for transfering the aerodynamic loads to the wingbox.

The entire geometry modeled in ANSYS® with quad SHELL 181 elements comprising a node at each corner, with 6 degrees of freedom at each node. Shell elements are particularly adapted for thin-walled structures such as that of a wing because they allow good accuracy at a low computational cost. The mesh was conformal at every shared edge. The shell elements were given thicknesses matching the geometry in the structural analysis report (Avions Marcel Dassault - Breguet Aviation, 1972). The validation of the wingbox FEA model is presented in section 3.3.

Reinforcement Analysis

After validating the results and showing their mesh independence the complete geometry described in section 2.2.2 was analyzed with the different winglets. The spars were fully clamped at the wing root. The static critical loading conditions corresponding to a gust, roll maneuver and sideslip maneuver were simulated. Pressure loads corresponding to these conditions, determined for every winglet configuration using the VLM models, were mapped to the external wing surface in ANSYS Mechanical®.

Inertia loads were applied as distributed forces and the stresses in the wingbox were determined.

The Falcon 10 wingbox structure is made of aluminum A7U4SG-T651, whose mechanical properties were not explicitly given in the structural analysis report (Avions Marcel Dassault - Breguet Aviation, 1972). However, it was possible to back-calculate the stress-strain behavior from the buckling curve included in that report (Figure 2.6). For the finite element analysis, the plastic behavior was approximated by using a multilinear isotropic stress-strain model, where the stress strain curve is approximated by three linear portions of different tangent modulus as shown in Figure 2.6. The tangent moduli used are given in Table 2.2. The material yield stress is 60.9 ksi (420 MPa) and its ultimate tensile strength is 68.2 ksi (470 MPa).

Table 2.2. Material mulitlinear isotropic model.

σ (ksi)	E_t (ksi)	ϵ (-)
0	10152.6	0
58.0	725.2	0.00571
63.8	60.9	0.01371
68.2	60.9	0.08514

The maximum and minimum principal stresses σ_1 and σ_3 in the structure were compared to the tensile strength of the material and the margin of safety was calculated for each winglet and load condition. At locations where the stresses exceeded the allowable values, reinforcement was made by increasing the thickness of the skin
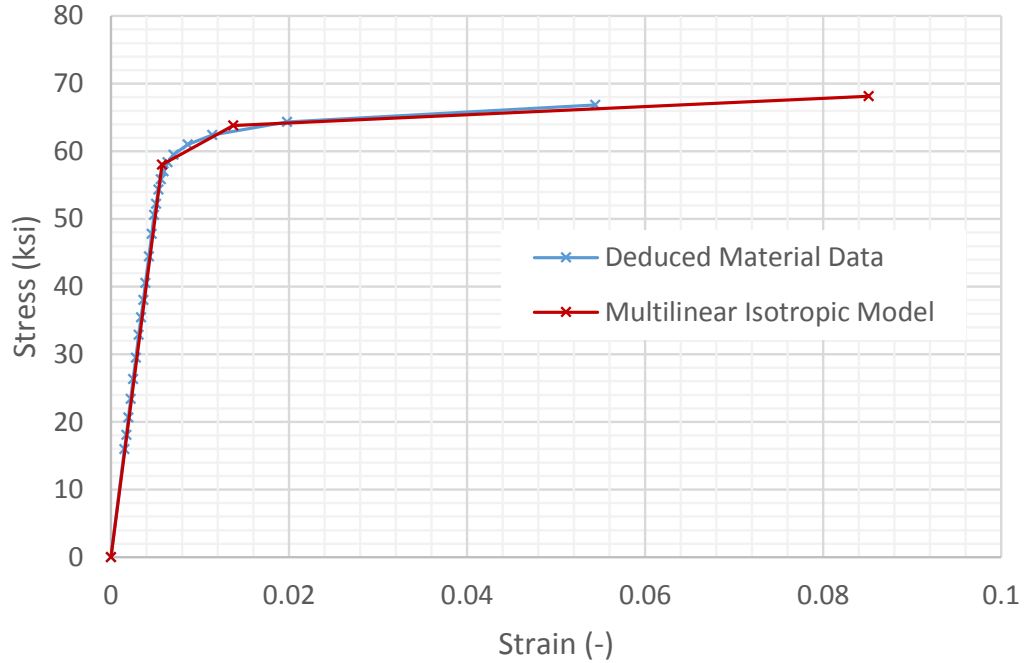
Figure 2.6. A7U4SG-T651 stress-strain behavior.

panels, equivalent to adding skin doublers to the structure. The thickness required was simply estimated using a margin of safety of 18% by

$$t_{required} = 1.18 \times t_{original} \times \frac{\sigma_{max}}{\sigma_{ult}} \tag{2.7}$$

The actual stresses in the reinforced panels were then computed by FEM simulations to verify that the principal stresses were not larger than the allowable values. The weight increase was then calculated using the material density.

The second failure mode considered was buckling. Because of the bending loads, the upper skin is under compression and buckling is likely to occur. In the structural analysis report from Avions Marcel Dassault - Breguet Aviation (1972), the structure

was designed for two buckling modes: general buckling of the upper skin and local buckling of the upper skin stiffeners. Significant margins of safety were found for local buckling while global buckling appeared to be more critical. Because of this, local buckling was ignored in this study.

The buckling curve for aluminum A7U4SG (Figure 2.7) gives critical buckling stresses as a function of the parameter $kL\rho$, where k is an end fixity constant, L the length of the skin panel considered (i.e. the distance between two ribs) and ρ the radius of gyration of the skin panel cross section about its centroid. It is based on the Euler buckling formula and uses the tangent modulus corresponding to every value of the critical buckling stress σ_{cr}.
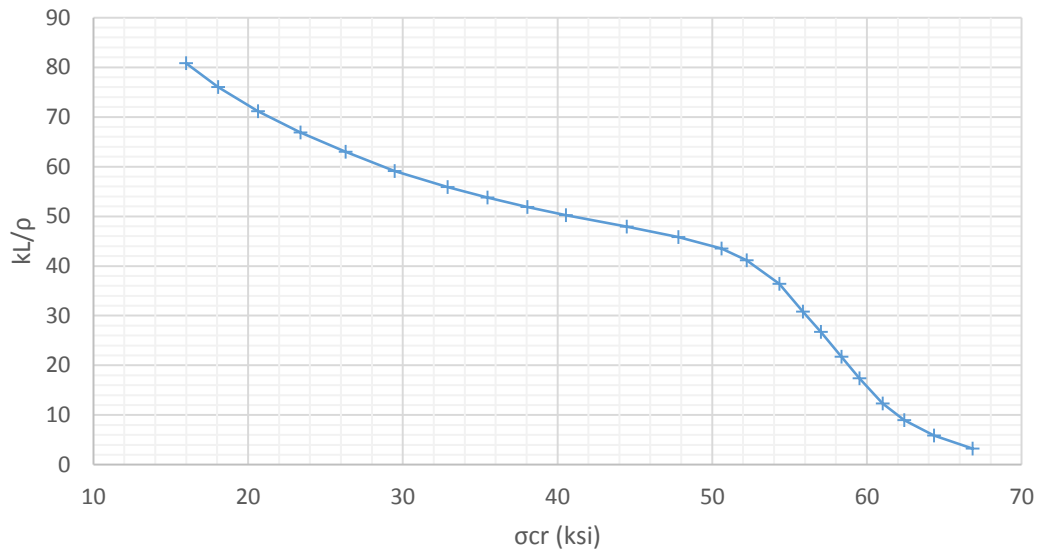
Figure 2.7. Buckling curve A7U4SG from Avions Marcel Dassault - Breguet Aviation (1972).

For each upper skin panel, the radius of gyration was calculated at the panel's most inboard rib (where compressive stresses where higher). The critical stress value was then determined from Figure 2.7 for every panel (i.e. at every rib location). The values for k were those given in the structural analysis report (Avions Marcel Dassault - Breguet Aviation, 1972). The maximum negative principal stresses were extracted from the FEA results at each rib location and compared to the critical stresses and reinforcement was added when $|\sigma_3| > |\sigma_{cr}|$.

Whenever the buckling stress was exceeded Z stiffeners were added. The width of the top flange of the stiffener was fixed to provide room for fasteners. Assuming rivets of 3/32 inches in diameter, the flange width is given by Niu (2006) as :

$$e_{min} = 2 \times \varnothing_{rivet} + 0.03in = 0.2175in \tag{2.8}$$

The width d of the lower flange was set as 2.5 times the height h of the stiffener and the thickness of the stiffeners was set as 1.2 times the local thickness of the skin (Figure 2.8).

The dimensions were determined using an iterative process shown in Figure 2.9, using a margin of safety of 18%.

The new stiffeners were located at the midpoint between the original wingbox stiffeners. The height of the stiffeners was kept lower than the height of the original stiffeners, to limit their impact on the available space inside the wingbox.
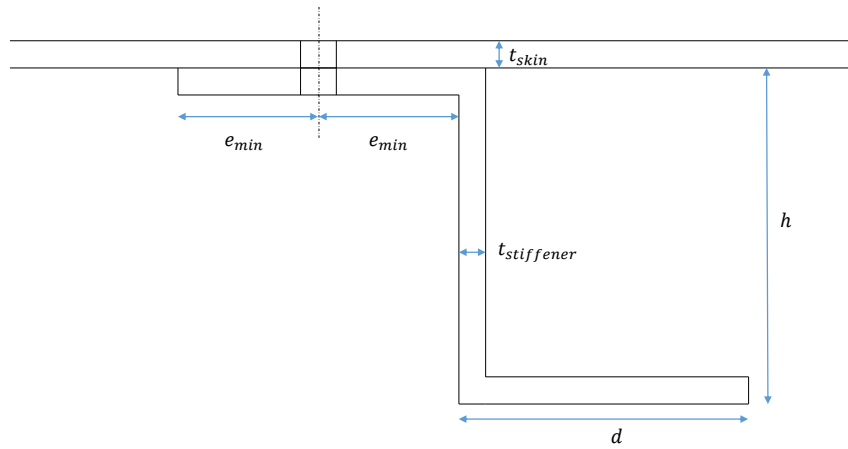
Figure 2.8. Stiffener cross section and dimensions.
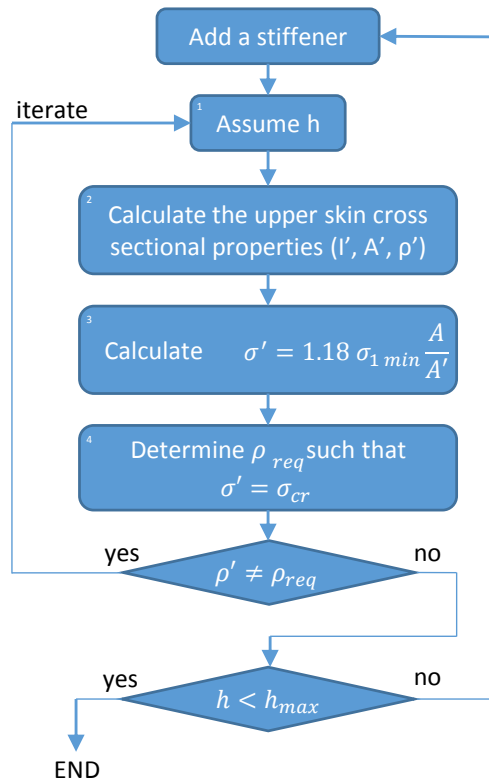
Figure 2.9. Synthetic diagram of the stiffener sizing algorithm.

The volume of all the new stiffeners was computed and multiplied by the material density to calculate the reinforcement weight increase and a factor of 1.5 was applied to account for fasteners (Niu, 1999).

2.3 Winglet Performance Evaluation

The winglets performance was evaluated with respect to their overall impact on the aircraft range, using equation 2.9, integrated numerically for a cruise at constant altitude and Mach number.

$$R = -\int_{W_0}^{W_1} \frac{C_L}{C_D} \, \frac{M.a}{c} \, \frac{dW}{W} \tag{2.9}$$

Here, the initial weight is the MTOW and W_1 was set equal to the max zero fuel weight (MZFW) plus the total weight added due to the winglet and reinforcement. The drag polars used were those discussed in section 2.1.2. The specific fuel consumption c was interpolated for each weight step from tabulated data for the TFE731-2 engines, scaled from the TFE731-1069 engine data available (Nicolai & Carichner, 2010). The range was calculated at 35,000 ft and 40,000 ft for cruise at Mach 0.7 and Mach 0.8.

The winglet resulting in the best range was selected for a more refined analysis.

2.4 Full Mission Analysis

To estimate the overall benefit over the baseline aircraft, a full mission analysis was performed for both the baseline aircraft and the aircraft equipped with the selected winglet. The mission profile used is shown in Figure 2.10.

Cruise : Constant Mach and altitude

Descent : Constant Mach
and rate of descent

200 Nm

Hold 30 min

Climb :
Max continuous thrust
Constant Airspeed for
Optimum rate of Climb
(260 kts)

Destination

Alternate

Taxi : 10 min Idle Thrust
Takeoff : 1 min Max Static Thrust

Range

Reserves
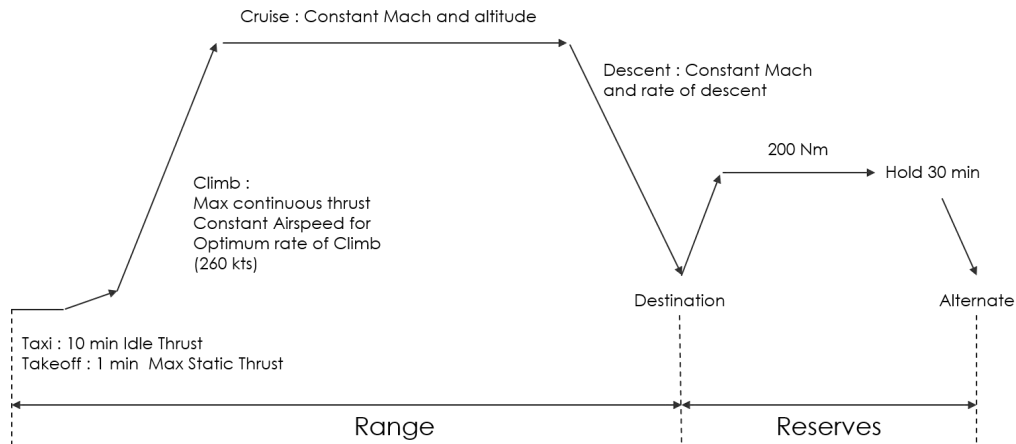
Figure 2.10. Mission profile used for overall performance evaluation.

The aircraft takes off from standard sea level at MTOW with a crew of 2 (170 lb each) and 4 passengers (165 lb each). During taxi, the amount of fuel burned is that equivalent to 10 minutes at idle thrust. For takeoff, the engine is set to maximum sea level static thrust for 1 minute. The takeoff phase ends at 35 ft height and the aircraft then climbs at maximum continuous thrust until reaching the specified cruise altitude. Under 10,000 ft, the aircraft is in the controlled airspace and its airspeed is limited to 250 KIAS. Above 10,000 ft, the aircraft climbs at 260 KIAS, corresponding to the optimal rate of climb. Once the cruise Mach number is reached, it is held constant for the end of the climb segment until the cruise altitude is reached. Cruise

is made at a constant altitude and Mach number until the top of descent. Descent is then made from cruise altitude down to sea level at a constant rate of descent of 3000 feet per minute. A constant Mach number of 0.8 is held (normal descent (Avions Marcel Dassault - Breguet Aviation, 1993)) until entering the controlled airspace at 10,000 ft. The airspeed is then reduced back to 250 KIAS. The aircraft finally lands with reserves corresponding to a climb and cruise to an alternate airport at 200 Nm, plus 30 minutes of loiter at that airport. The reserves were read from the Falcon 10 operational instructions manual (Avions Marcel Dassault - Breguet Aviation, 1993) and, for simplicity, this amount of fuel was used for both winglet and baseline aircraft.

The entire mission was calculated by numerical integration of the equations of motion. For climb, the integration was carried out in 100 ft increments from 35 ft to the cruise altitude. For descent, the integration was carried out in 100 ft increments, backwards from sea level to cruise altitude. For cruise the stepping variable was the fuel, spent in 20 lb decrements between the previously determined top of climb and top of descent weights.

Thus, the ranges for the baseline aircraft and with winglets were calculated to establish the overall change. Also, the fuel burned by both aircraft to cover a distance of 1200 Nm was computed and the two were compared. For this calculation, both aircraft took off with a crew of 2 and 4 passengers, with the minimum amount of fuel required to reach the specified range, which was found iteratively. Climb and descent were integrated as for the mission analysis and cruise was integrated by increments of 10 Nm up to a total range of 1200 Nm and the fuel burn was calculated. Thus

the efficiency of the winglet can either be presented as a range increase or a fuel consumption reduction.

3. Validation

The different calculation methods were calibrated and validated with measured data as much as it was possible. Each one of them is explained in this section.

3.1 CFD Grid Convergence Study

An initial CFD mesh was first created for the baseline wing and a grid convergence study was performed by changing parameters such as the far field spacing, wake length, wall spacing, etc. All meshes were created using Pointwise®. Simulations were run for an angle of attack of 3 degrees at Mach 0.7. The level of accuracy sought was 10^{-5} for C_D and 10^{-4} for C_L. The results of this study are presented next.

3.1.1 Initial Mesh

A conforming hybrid mesh was created, comprising structured blocks in the vicinity of the wing (later called boundary layer block) and in the wake (later called wake block), and an unstructured block all around. This choice was made to combine the better accuracy and faster resolution associated with a structured mesh (elements aligned with the flow within the boundary layer and the wake, mesh orthogonality at the wall), and the fast and easy generation of an unstructured mesh in the far field, avoiding topology issues and unnecessary refined regions.

First a structured 2D mesh on the wing surface from airfoil Section A to D was generated (Figure 3.1). As suggested by Vassberg, DeHaan, and Sclafani (2003), each airfoil section was divided into approximately 200 nodes. To allow good resolution of the leading edge curvature and associated pressure gradients as well as flow features at the wing base, the mesh was refined in those regions. From section A to D, the mesh contains approximately 210 spanwise sections. Since no wing body interactions occur in the case of this study, there was no need to refine the mesh at the root. At the tip however, there was need for a finer mesh because of the importance of accurately modeling the tip vortices.

Because the shape of the wing tip was rounded, it was broken into 6 different domains (3 on the upper surface and 3 on the lower surface) as shown in Figure 3.1. The upper and lower tip surface contain each an unstructured domain which was created to avoid highly skewed cells near point 1 shown on Figure 3.1 and its corresponding point on the lower surface.

At the trailing edge the wing is cut off straight, forming a 6 mm thick flat base. A structured mesh was applied to most of the base. An unstructured mesh was applied to a small portion of the base located at the wing tip to avoid highly skewed quad cells (Figure 3.2). The average edge length on the overall wing surface was 0.780 in.

Once the surface mesh was created, the upper and lower surfaces of the wing were extruded outwards to form the structured boundary layer block (purple block in Figure 3.3). The two unstructured domains at the tip were extruded similarly to form prism layers. The initial boundary layer block comprised 26 layers grown using
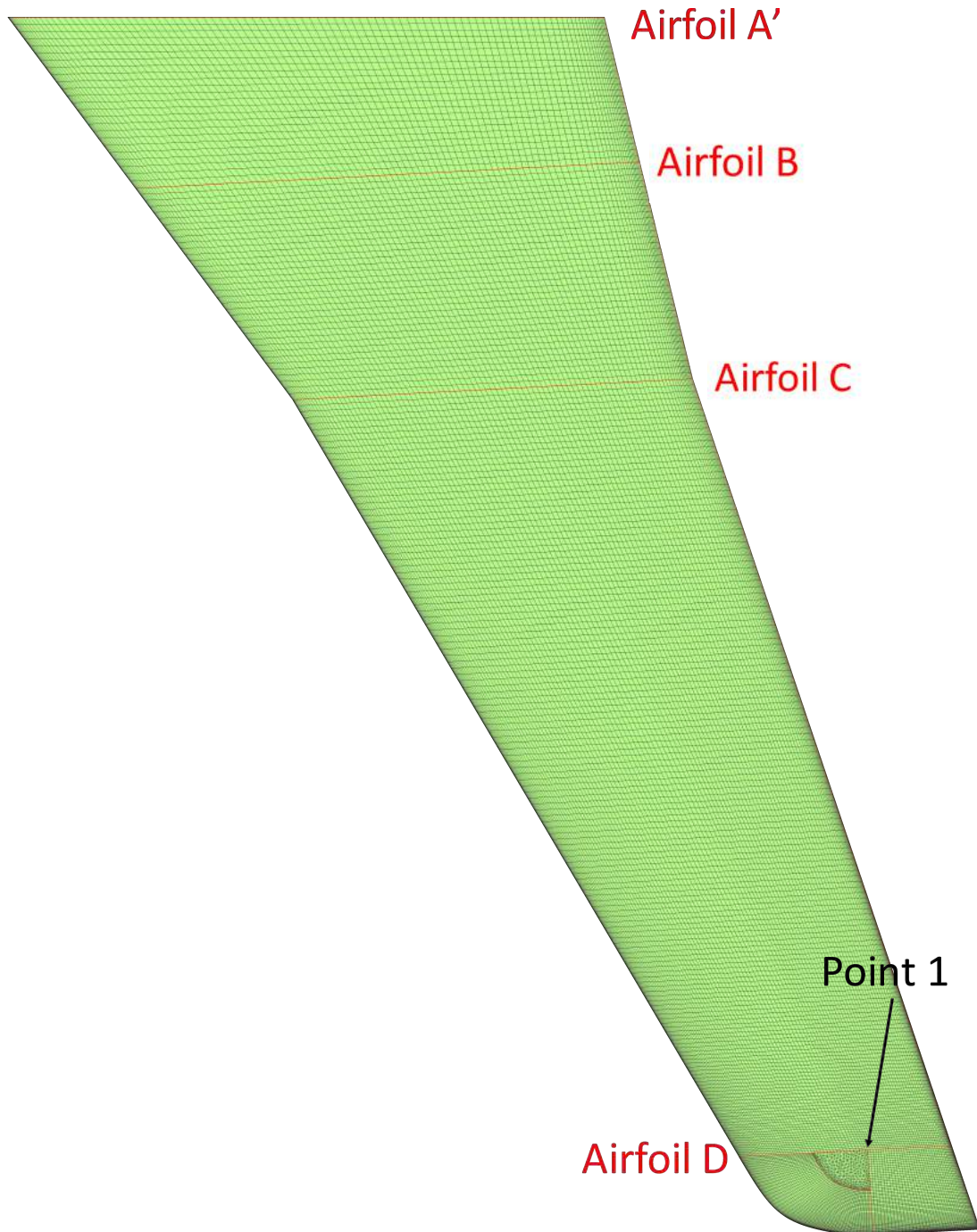
Figure 3.1. Wing surface mesh.
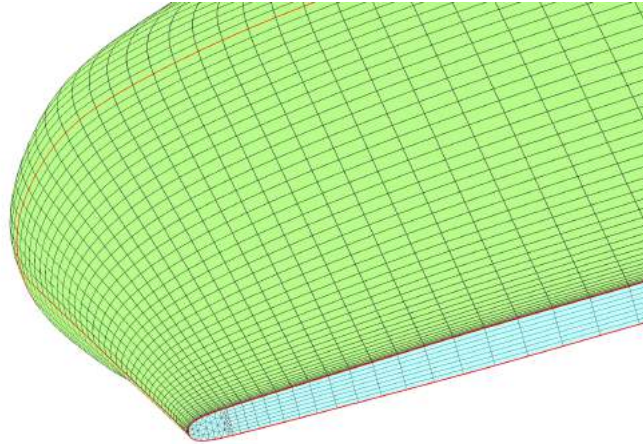
Figure 3.2. Wing tip base mesh.

a wall spacing of 0.00984 in and a spacing growth rate of 1.2. The other meshes used in the convergence study were generated using wall spacings from 0.00984 in to 0.00177 in and growth rates from 1.1 to 1.2 (see tables) but for all baseline wing meshes the boundary layer block was grown up to approximately 4.7 in above and under the wing surface. The wing base domains and the rearward facing domains of the boundary layer block were then extruded 16.4 ft along the x-axis to form the wake block (yellow block in Figure 3.3). The longitudinal spacing was progressively coarsened in the wake from a value of 0.00984 in at the trailing edge base to 0.0984 in at the upper and lower limits of the wake block and to 1.1811 in at the wake end. As seen on Figure 3.3, the mesh spacing changes suddenly at the interface between the boundary layer block and the wake block. That mesh size transition was made smoother for later meshes.
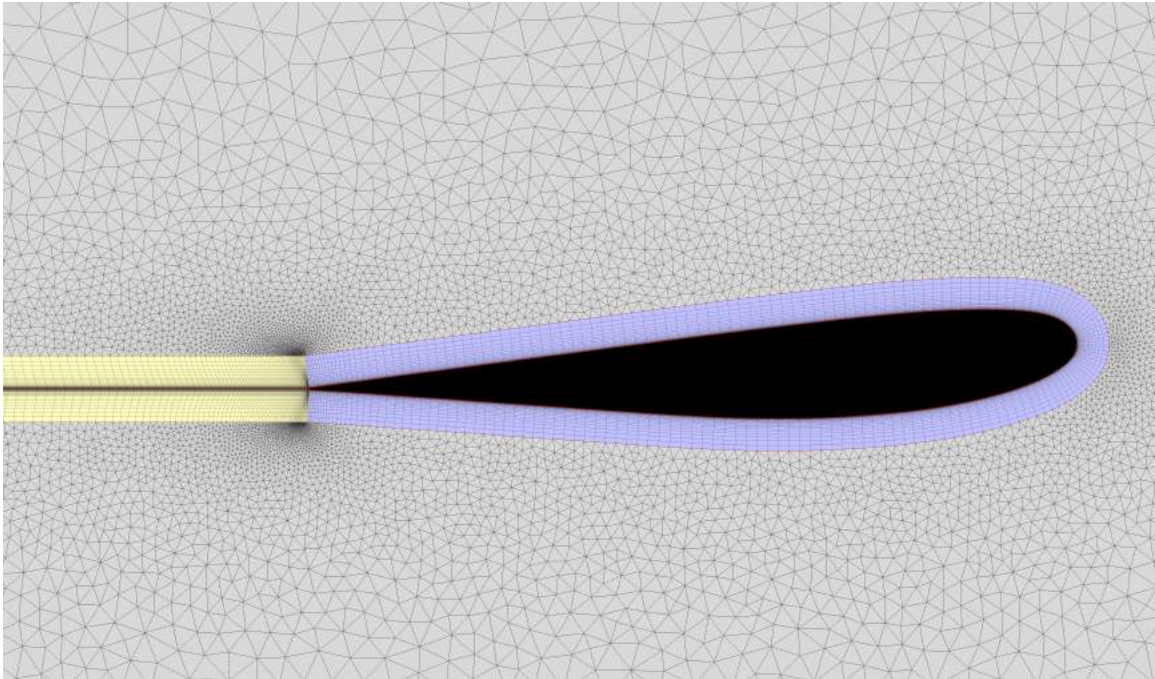
Figure 3.3. Symmetry plane view of the boundary layer and wake blocks.

This mesh topology gives good quality cells, aligned with the flow direction and orthogonal to the wall in the boundary layer and a good quality interface between the boundary layer block and the wake block.

Once satisfactory structured blocks were generated around the wing and in the wake region, an unstructured block was created around them. Vassberg et al. (2003) specify that the far-field boundaries should extend to at least 50 times the reference chord. Thus, a half sphere of 410.1 ft in radius was used as the far field and the unstructured symmetry domain was assembled between the far field and the structured domains at the wing root on the $(x; z)$ plane (Figure 3.4). An unstructured block was then generated, with pyramid elements at interface between the unstruc-

tured and structured meshes and nearly isotropic tetrahedral elements everywhere else. To allow smooth transition from the boundary layer and wake blocks to the far field, a decay factor of 0.85 was used. The resulting mesh contained a total number of 12,236,547 cells among which 7,351,935 were tetrahedral, 4,658,770 hexahedral, 183,932 pyramids and 41,910 prisms.
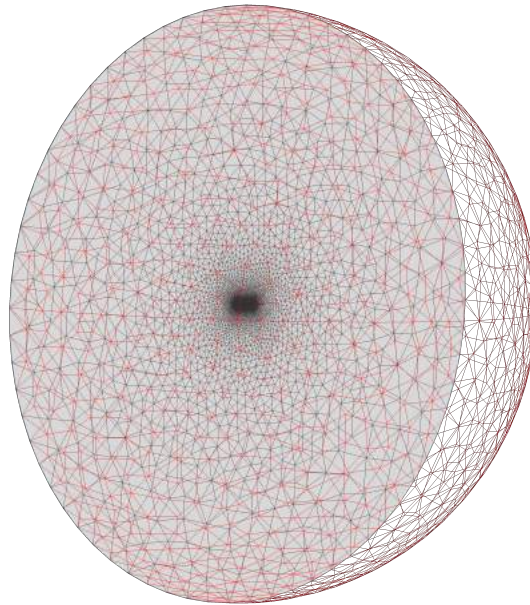
Figure 3.4. Far field view of the baseline wing mesh.

3.1.2 Independence on Chordwise and Spanwise Surface Spacing

To ensure the independence of the results with regard to the chordwise and spanwise spacing on the wing surface, a finer mesh was created by multiplying the spanwise and chordwise number of cells by 1.5 in the structured boundary layer block. The wall spacing was kept unchanged. This approach was preferred as compared to a
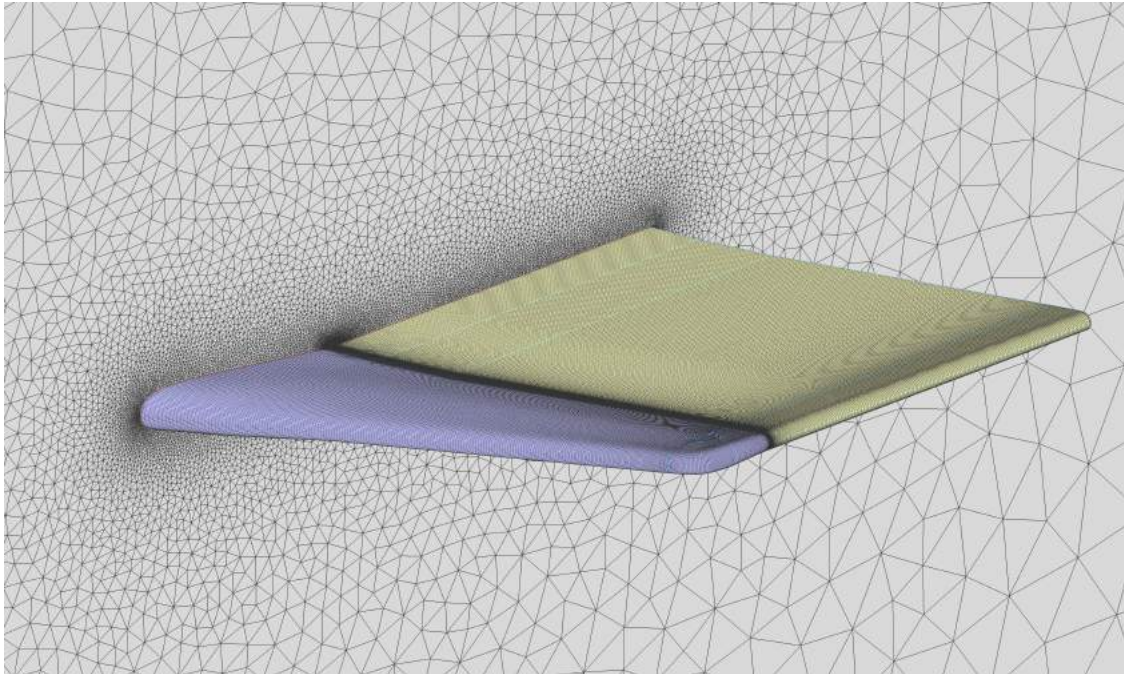
Figure 3.5. Far field view of the baseline wing mesh.

mesh adaption in Fluent® due to the large number of cells in the original mesh. The

lift and drag values calculated were unaffected by that change in mesh density (Table

3.1).

Table 3.1. Grid independence on the wing surface spacing.

	Mesh 0	Mesh 1
Number of Cells	12,236,547	28,113,128
Number of Airfoil Nodes	209	299
Wall Spacing (in)	0.00984	0.00984
Boundary Layer Growth Rate	1.2	1.2
Wake Spacing (in)	0.00984	0.00984
Turbulence Model	SA	SA
C_L	0.0791	0.0791
C_D	0.00371	0.00371

3.1.3 Independence on the Wake Length

Similarlry, the size of the wake block was reduced and its mesh density was modified. It was found that the lift and drag values were unchanged. Thus the 8.2 ft wake block was retained.

Table 3.2. Grid independence on the wake length.

	Mesh 1	Mesh 2
Number of Cells	28,113,128	17,218,888
Wake Length (ft)	16.4	8.2
Wall Spacing (in)	0.00984	0.00984
Boundary Layer Growth Rate	1.2	1.2
Wake Spacing (in)	0.00984	0.00984
Turbulence Model	SA	SA
C_L	0.0791	0.0791
C_D	0.00371	0.00371

3.1.4 Independence on the Wall Spacing

The grid spacing at the solid surfaces is important for boundary layer resolution, especially when turbulence is modeled. Usually, turbulence models require a wall spacing $y^+ \simeq 1$ to accurately solve the boundary layer, y^+ being defined as:

$$y^+ = y\frac{\rho_w u_\tau}{\mu_w} \tag{3.1}$$

where ρ_w is the fluid density at the wall and μ_w is the dynamic viscosity at the wall. The friction velocity u_τ is defined as:

$$u_\tau = \sqrt{\frac{\tau_w}{\rho_w}} \tag{3.2}$$

with $\tau_w = (\tau)_{1,2}$, the value of the viscous stress at the wall. Fluent's® enhanced wall treatment for the Spalart-Allmaras model theoretically allows accurate boundary layer solution for much higher values of y^+ ($1 < y^+ < 30$ included), hence reducing the computational cost. Fluent® still requires the boundary layer to be covered by at least 10 cells normal to the wall. Knowing that, the wall spacing was refined until results no longer changed. The growth rate in the boundary layer block and hence in the wake was progressively refined as well as the wall spacing. The spanwise and chordwise spacing was not changed to keep the number of cells to a minimum. The results of this study are presented in Table 3.3. It should be noted that the first simulations were run using the Spalart-Allmaras turbulence model which was later switched to the k-omega SST turbulence model because of its better accuracy for boundary layer resolution, notably when adverse pressure gradients may cause flow separation, typically the case in this study ("ANSYS Fluent User's Guide", 2011).

Since the wall spacing refinement was performed without adding elements in the chordwise or spanwise directions, the aspect ratio of the cells near the wall increased with every refinement. When the wall spacing reached 0.00177 in, there were convergence problems, probably due to these high aspect ratios. It was thus decided to

Table 3.3. Grid independence on the wall spacing.

	Mesh 0	Mesh 4a	Mesh 4b	Mesh 5a	Mesh 5b	Mesh 6
Number of Cells (Millions)	12.236	17.037	17.037	21.819	21.819	24.023
Wall Spacing (in)	0.00984	0.00590	0.00590	0.00276	0.00276	0.00177
Average Wall y^+	22.7	13.4	13.4	6.4	6.4	3.2
Boundary Layer Growth Rate	1.2	1.15	1.15	1.1	1.1	NA
Wake Length (ft)	16.4	8.2	8.2	8.2	8.2	8.2
Wake Spacing (in)	0.00984	0.00984	0.00984	0.00984	0.00984	0.00984
Turbulence Model	SA	SA	$k\text{-}\omega$ SST	SA	$k\text{-}\omega$ SST	$k\text{-}\omega$ SST
C_L	0.0791	0.0791	0.0788	0.0790	0.0786	0.0786
C_D	0.00371	0.00375	0.00369	0.00378	0.00381	0.00381

refine the mesh using Fluent®'s boundary mesh adaption tool. The 5 layers closest to the wall were adapted isotropically from the 0.00276 in wall spacing mesh, providing a wall spacing of 0.00177 in without significant elements distortion.

As shown in Table 3.3, the results on this last mesh were identical to the results on the 0.00276 in wall spacing mesh. Hence the 0.00276 in was judged fine enough. It corresponds to a y^+ value of the order of 1, as needed for accurate drag predictions.

3.1.5   Results Validation

After completing the grid independence study, Mesh 5b was selected for the remaining simulations with the k-ω SST turbulence model. Simulations were run for Mach 0.7 and 0.8 at angles of attack of -1º, 1º, 3º, 5º and 7º, imposing an accuracy of 10^{-4} for the lift coefficient and 10^{-5} for the drag coefficient. The results are shown in Table 3.4 and plotted in Figures 3.6 and 3.7, together with the wind tunnel data showing good accord. Once more, it is emphasized that the wind tunnel results apply to the entire aircraft, without horizontal tail whereas the CFD model corresponds to the wing only. Hence, the change in C_{Lo} and $dC_L/d\alpha$ can be attributed to the fuselage contribution. Similarly with the zero lift drag delta. It can be noted the good agreement in terms of induced drag.

Table 3.4. CFD results for the baseline wing and the winglet 1570.

	Mach 0.7				Mach 0.8			
	Baseline Wing		Winglet 1570		Baseline Wing		Winglet 1570	
α (deg)	C_L	C_D	C_L	C_D	C_L	C_D	C_L	C_D
-1	-0.1647	0.01035	-0.1720	0.01113	-0.1648	0.01035	-0.1720	0.01113
1	0.0059	0.00624	0.0049	0.00699	0.0059	0.00624	0.0049	0.00699
3	0.1761	0.00861	0.1827	0.00845	0.1761	0.00861	0.1827	0.00845
5	0.3563	0.01579	0.3670	0.01578	0.3563	0.01579	0.3670	0.01578
7	0.5035	0.03994	0.5186	0.04445	0.5035	0.03994	0.5186	0.04445

For calibration purposes, the winglet 1570 was meshed and analyzed in Fluent® for the same Mach numbers and angles of attack. A similar mesh topology to the one used for the baseline wing mesh 5 was used. However a few modifications were however made at the interface between structured and unstructured blocks at the
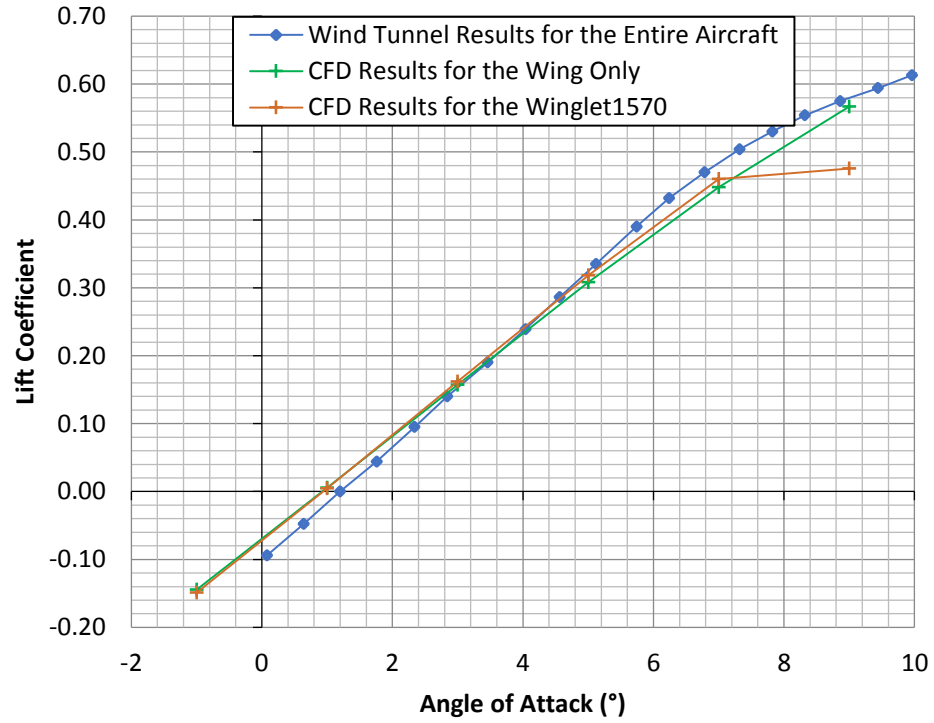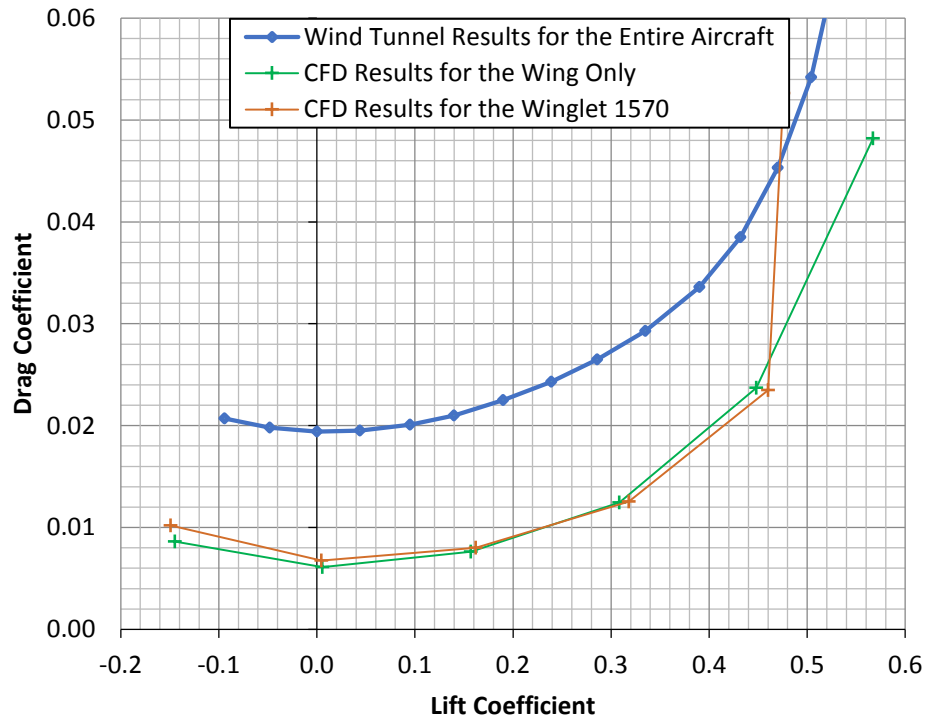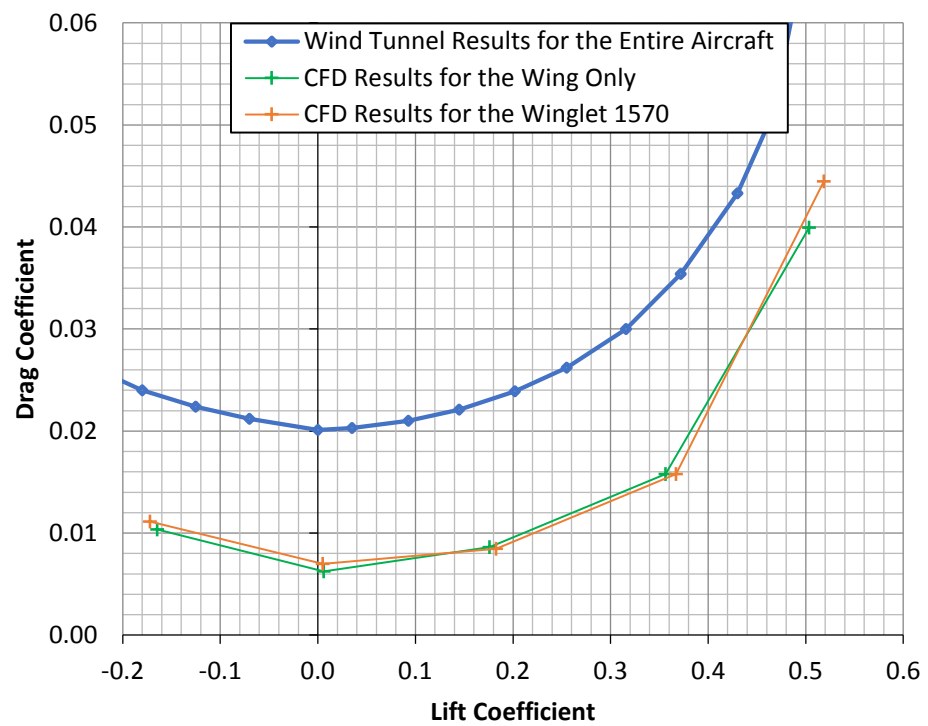
(a) Mach 0.7
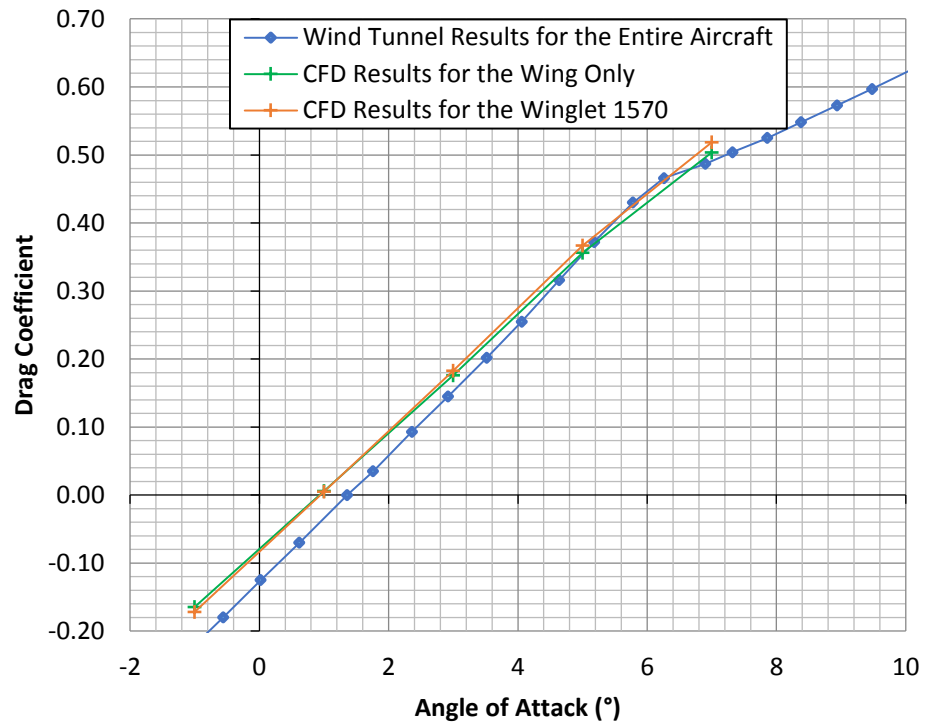
(b) Mach 0.8

Figure 3.6. Lift coefficients vs. angle of attack at Mach 0.7 and 0.8.

(a) Mach 0.7

(b) Mach 0.8

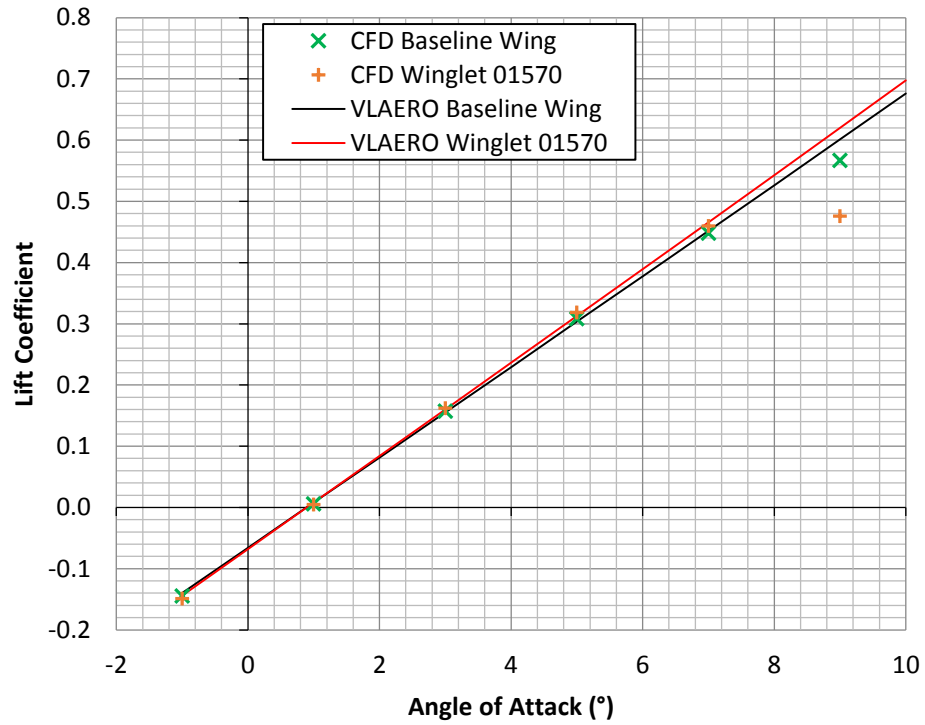Figure 3.7. Drag polars at Mach 0.7 and 0.8.

trailing edge and at the end of the wake block. In order to prevent highly skewed tetrahedrons, a non-conformal mesh was used to transition from the boundary layer block and the wake block to the outer unstructured block. Highly skewed cells were found to increase convergence time significantly. The numerical results obtained for the winglet 1570 are plotted in Figures 3.6 and 3.7. Comparing these results to those of the baseline wing, an increase in the lift curve slope and in the minimum drag due to the winglet are observed. As the angle of attack increases, the winglet offers a slight drag reduction compared to the baseline wing. The winglet beneficial effect is mostly seen on the drag polar. For the same lift coefficient, the winglet reduces drag. It should be noted that the simulations for $\alpha = 7\,\mathrm{deg}$ were not fully converged but that was of no significance since that flight condition is not relevant for the present work.

3.2   VLM Model Calibration

The correction factors for the VLM models were derived from the RANS calculations and wind tunnel results as explained in section 2.1.2.

3.2.1   VLM External Wing Model

Figures 3.8 and 3.9 show the results from VLAERO® compared to those obtained in Fluent® for the wing only.

(a) Mach 0.7
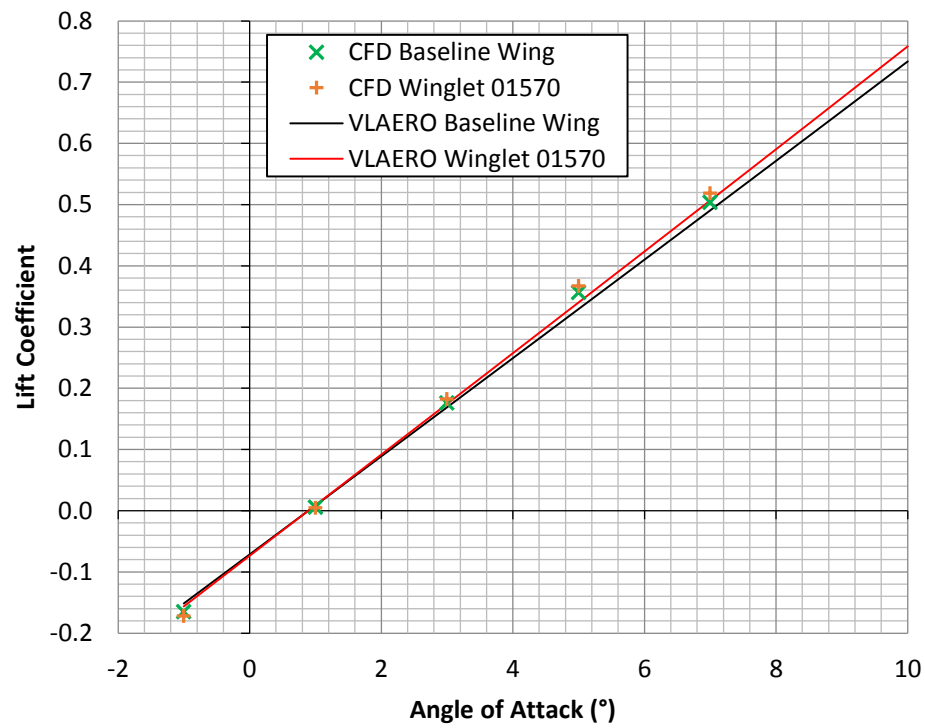
(b) Mach 0.8

Figure 3.8. Lift coefficients vs. angle of attack at Mach 0.7 and 0.8 for the isolated wing (RANS and VLM).
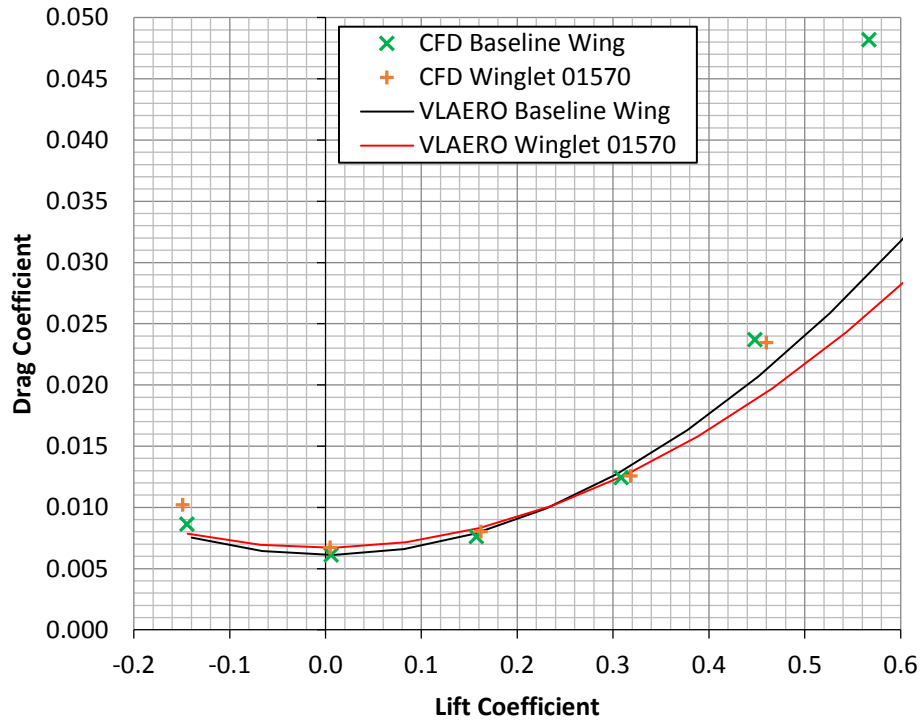
(a) Mach 0.7
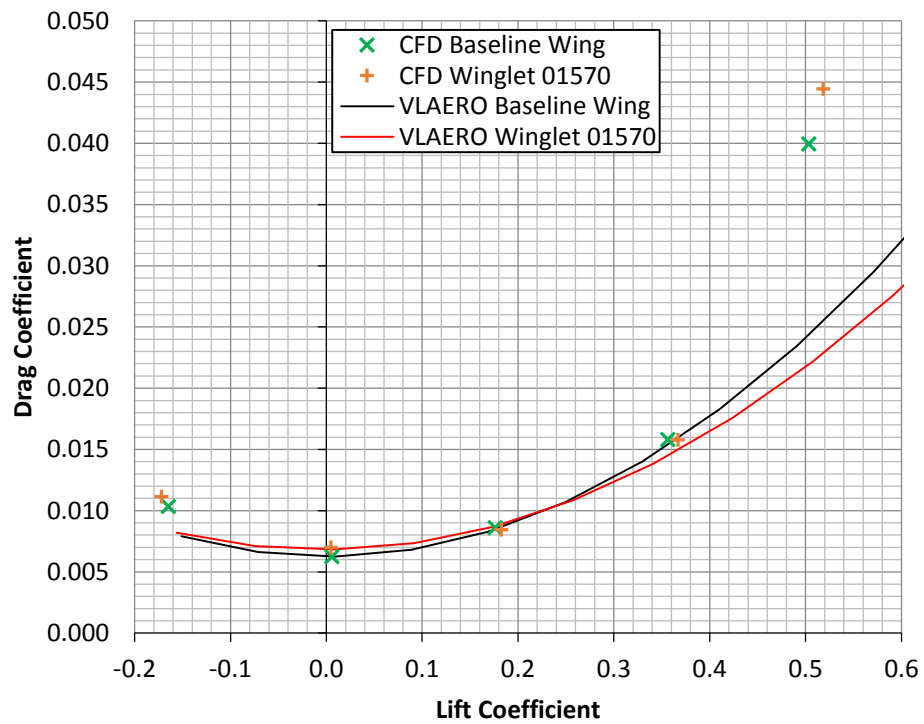
(b) Mach 0.8

Figure 3.9. Drag polars at Mach 0.7 and 0.8 for the isolated wing (RANS and VLM).

The drag coefficients shown in these figures represent the induced drag from VLAERO® to which a constant minimum drag term corresponding to the baseline wing was added. For the Winglet 1570, the additional winglet contribution C_{DoWL} was added (see section 2.1.3).

There was good agreement between the VLM and the RANS results in the operational range of lift coefficients for both Mach 0.7 and 0.8. For the drag, important differences were found at lift coefficients above 0.4 due to the viscous effects and shockwaves.

The correction factor used in the winglet parasite drag estimation (2.1.3) gives satisfactory results both at Mach 0.7 and 0.8 for winglet 1570 and it was hence retained for the other winglet configurations.

3.2.2 Full Aircraft Longitudinal VLM Model

The results obtained for the calibrated aircraft were compared to the wind tunnel results in Figures 3.10 to 3.12. As shown in those figures, the VLM lift and pitching moment predictions agree with the wind tunnel results up to angles of attack of approximately 6º above which shock waves start appearing on the wing. The differences in drag between VLM and wind tunnel for higher lift coefficients can be attributed to regions of separated flow on the wing and fuselage that the VLM does not capture.
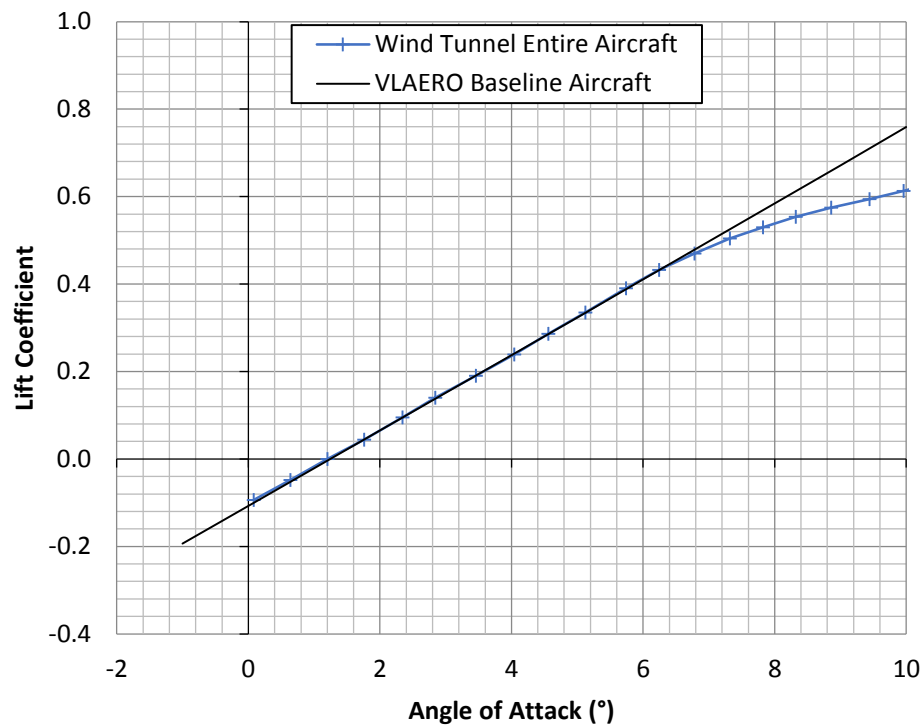
(a) Mach 0.7
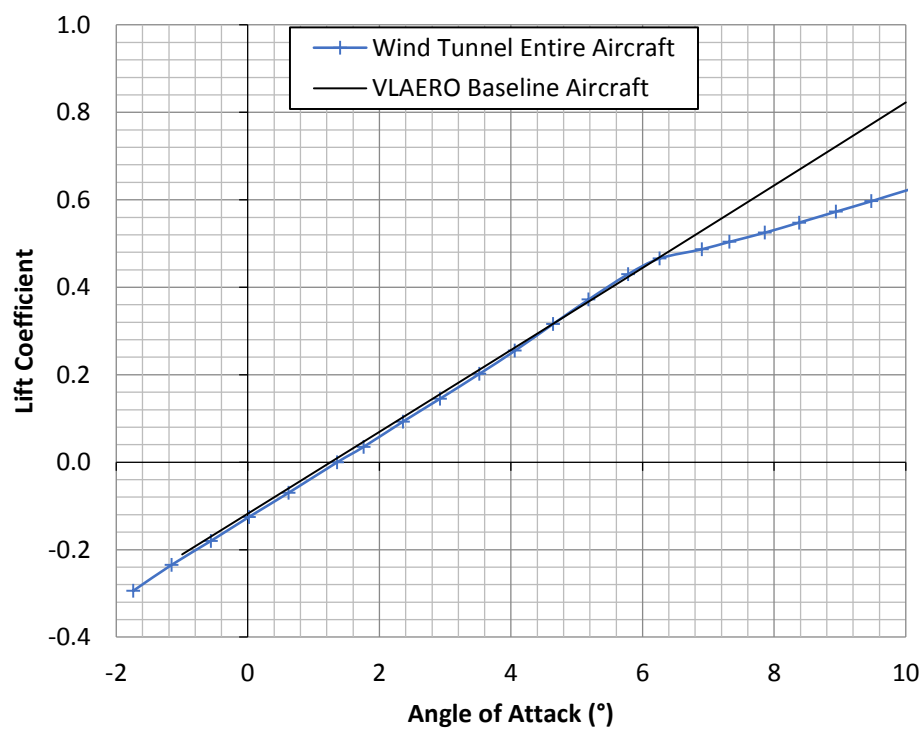
(b) Mach 0.8

Figure 3.10. Lift coefficients vs. angle of attack at Mach 0.7 and 0.8 for the entire aircraft (VLM and wind tunnel).
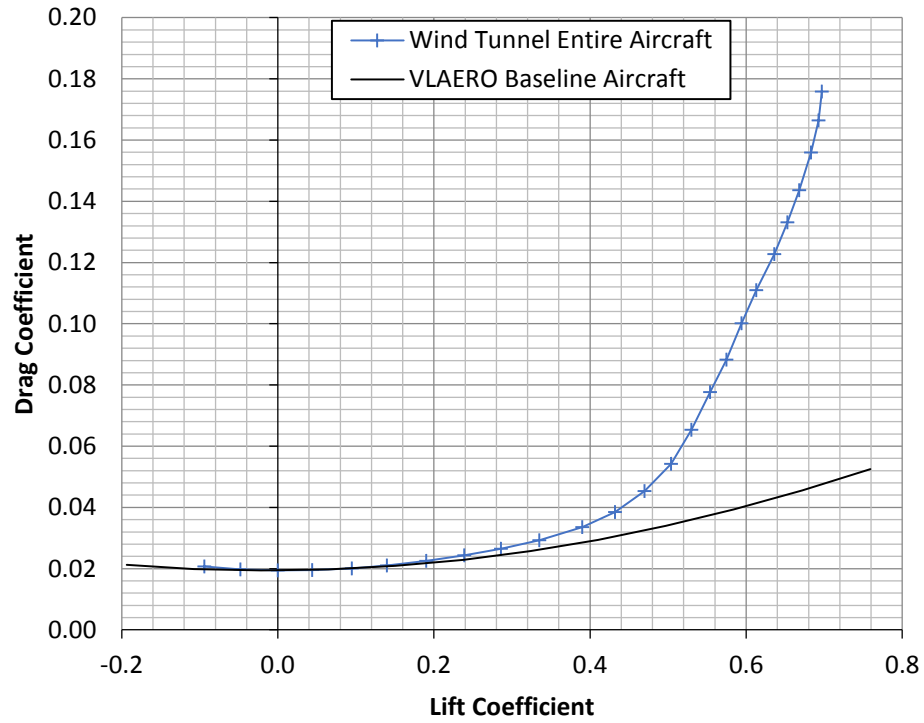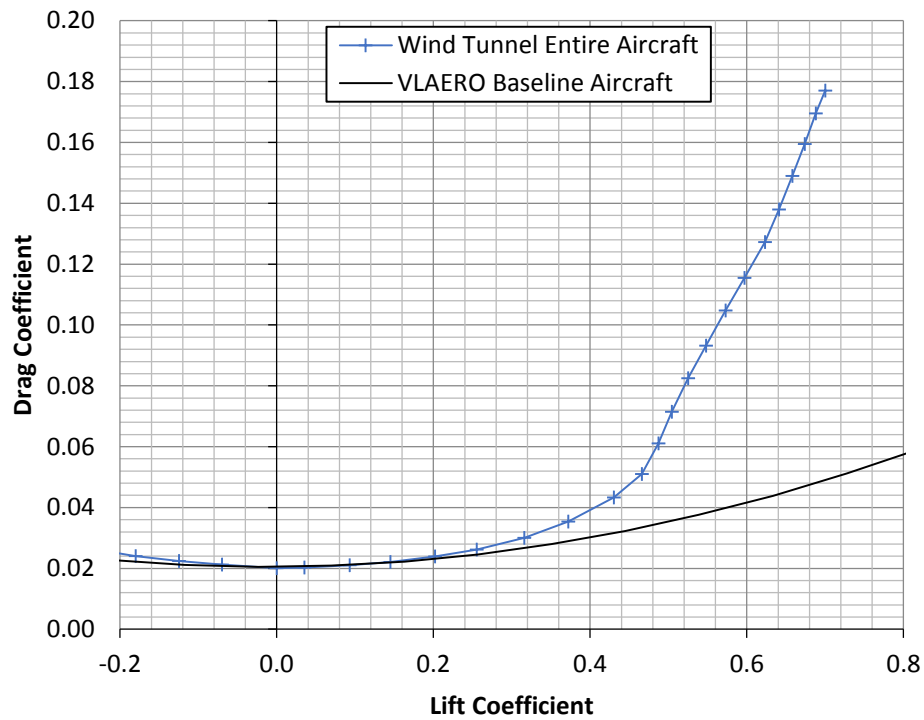
(a) Mach 0.7

(b) Mach 0.8

Figure 3.11. Drag coefficient vs. lift coefficient at Mach 0.7 and 0.8 for the entire aircraft (VLM and wind tunnel).
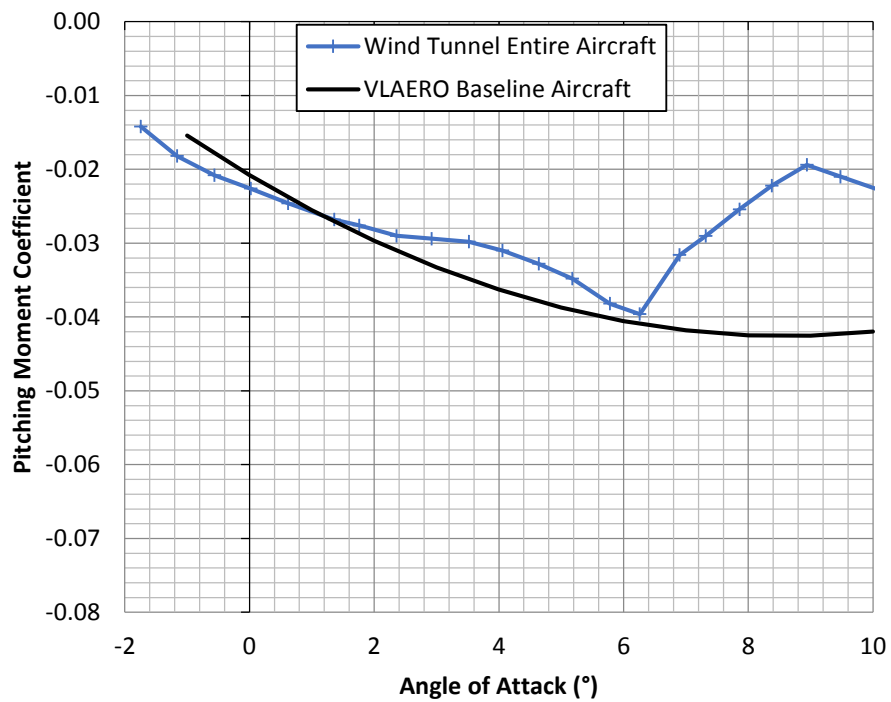
(a) Mach 0.7

(b) Mach 0.8

Figure 3.12. Pitching moment at 25% of the mean aerodynamic chord vs. angle of attack at Mach 0.7 and 0.8 for the entire aircraft (VLM and wind tunnel).

3.3   Wingbox Finite Element Model Validation

Before using the FEM model for further analysis, a grid independence study was performed and validation was made against results given by Avions Marcel Dassault - Breguet Aviation (1972) in which stress calculations at 8 different stations along the span (S1 to S8 in Figure 2.5) wer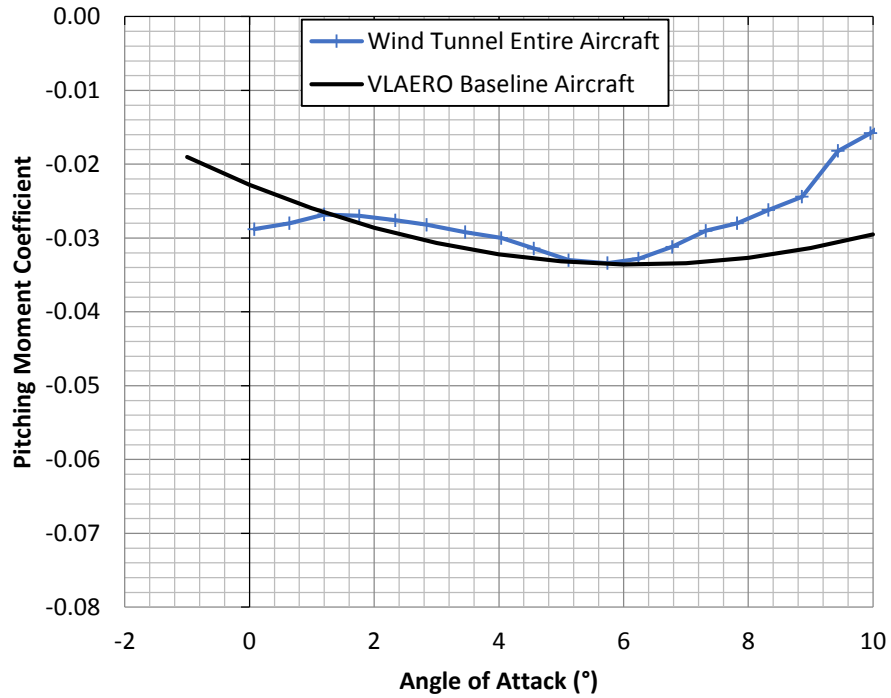e reported for several loading conditions. At each station, the cross section was separated in nodes for which the values of the thickness, normal stress and shear stress were given. Details on the methodology employed for the stress calculations in that report were not available but it would appear that the normal and shear stresses were calculated using thin-walled panel idealizations.

For validation of the FEM model, the loading case F* of the structural analysis report (Avions Marcel Dassault - Breguet Aviation, 1972) was used, which corresponds to a negative gust. A system of distributed pressures and moments were applied to the wing structure in ANSYS® to reproduce the corresponding loads in terms of shear force, bending and twisting moments. The structural analysis report assumes a rigid material. Thus a 29,008 ksi Young's modulus was used in the FEA. All degrees of freedom were fixed at the root, except that the rear spar was left free because the report seemed to imply that all the loads were carried by the portion of the wingbox located between the front and mid spars

The normal and shear stresses resulting from the finite element calculations were extracted at each station and the maximum values were compared with those from the structural analysis report (Avions Marcel Dassault - Breguet Aviation, 1972) for
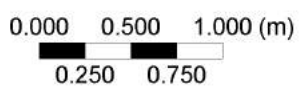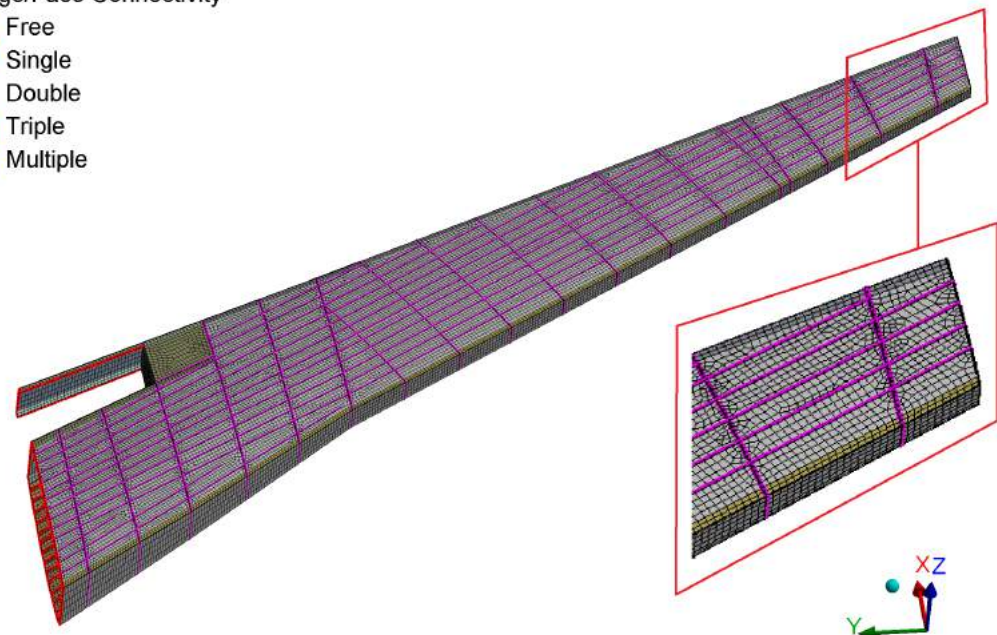
Figure 3.13. Wingbox mesh 2.

four meshes of increasing density. The results are presented in Figure 3.14 below, showing good agreement between the FEM and stress report. The discrepancies at the root and the tip are due to stress concentrations due to boundary conditions and fixity imposed on the model and therefore they were disregarded.

Good agreement was found between the shear stresses of the FEM and the stress report (Avions Marcel Dassault - Breguet Aviation, 1972) for stations 4 to 8. For stations 1 to 3, there are non negligible differences. It must be noted that from section 1 to 2 the aft spar designates the mid spar and from rib 3 to 8, the rear spar. The error hence corresponds to the region where the mid spar takes on part of the wingbox loads to transfer them towards the attachment. In the FEA model, this load transfer is made through ribs 2 and 3 as it is suggested on the aircraft maintenance manual drawings. The upper and lower skin between ribs 2 and 3 and mid spar and rear spar participate in the load transfer. No details were given about the geometry of this attachment in the structural report and it is believed that the report contains simplifying assumptions regarding this attachment that are less accurate than the analysis that can be performed with the FEM. Hence the discrepancies.

For the shear stresses at the front spar, numerical results agree reasonably well with the results of Avions Marcel Dassault - Breguet Aviation (1972). The difference found in the inboard part of the wing can be attributed to some discrepancies in the spar thickness found in the stress report. Several sections of the report have different thickness values.
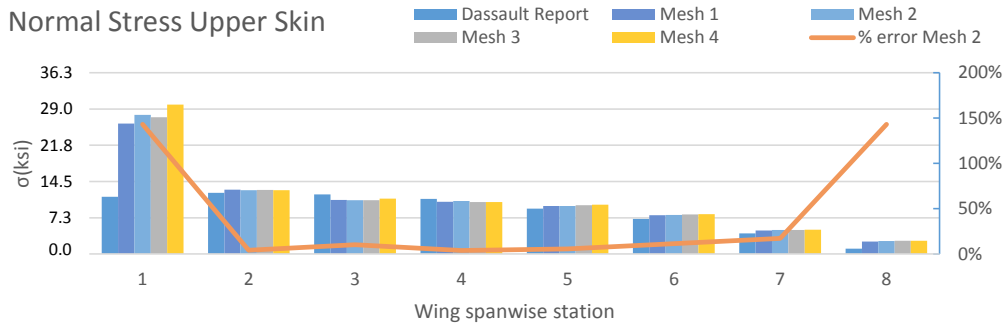
(a) Normal Stress Upper Skin
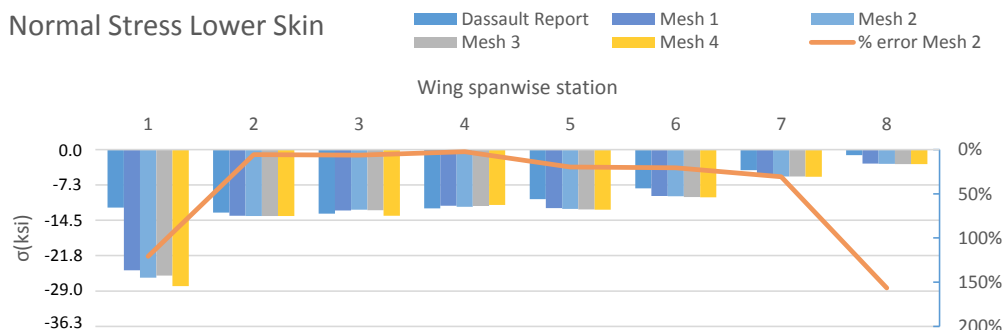
(b) Normal Stress Lower Skin
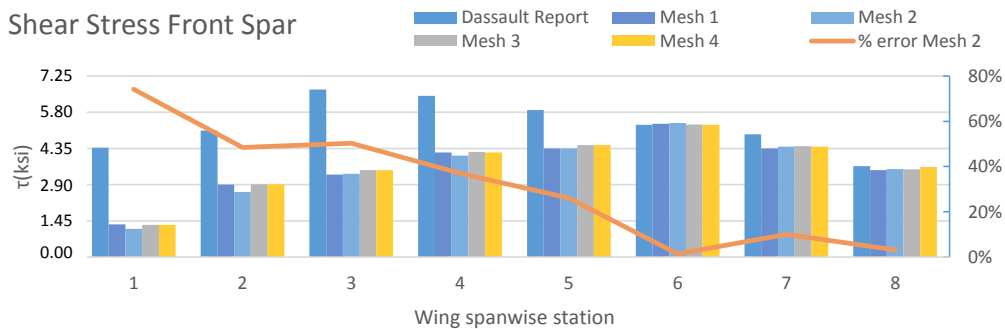
(c) Shear Stress Upper Skin
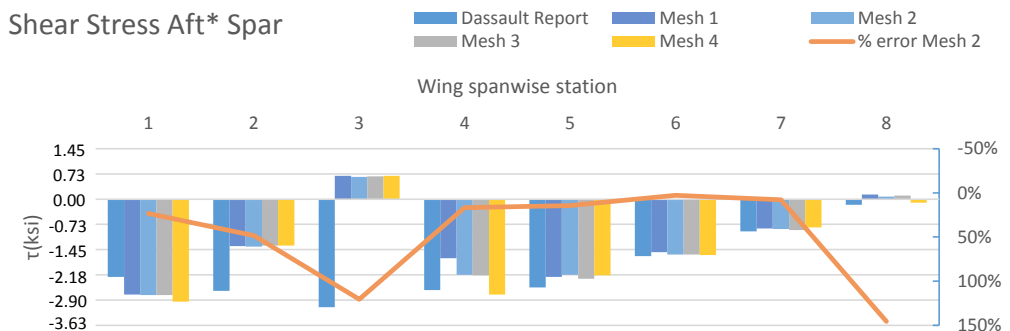
(d) Shear Stress Lower Skin

Figure 3.14. Wingbox stations normal and shear stresses.

C: Static Structural
Equivalent Stress
Type: Equivalent (von-Mises) Stress - Top/Bottom - Layer 0
Unit: Pa
Time: 1
2/27/2015 4:19 PM

2.0769e8 Max
1.3514e8
1.2388e8
1.1262e8
1.0136e8
9.0098e7
7.8837e7
6.7576e7
5.6315e7
4.5054e7
3.3794e7
2.2533e7
1.1272e7
11209 Min

ANSYS
R14.5
Academic

0.000   0.100   0.200 (m)
    0.050   0.150
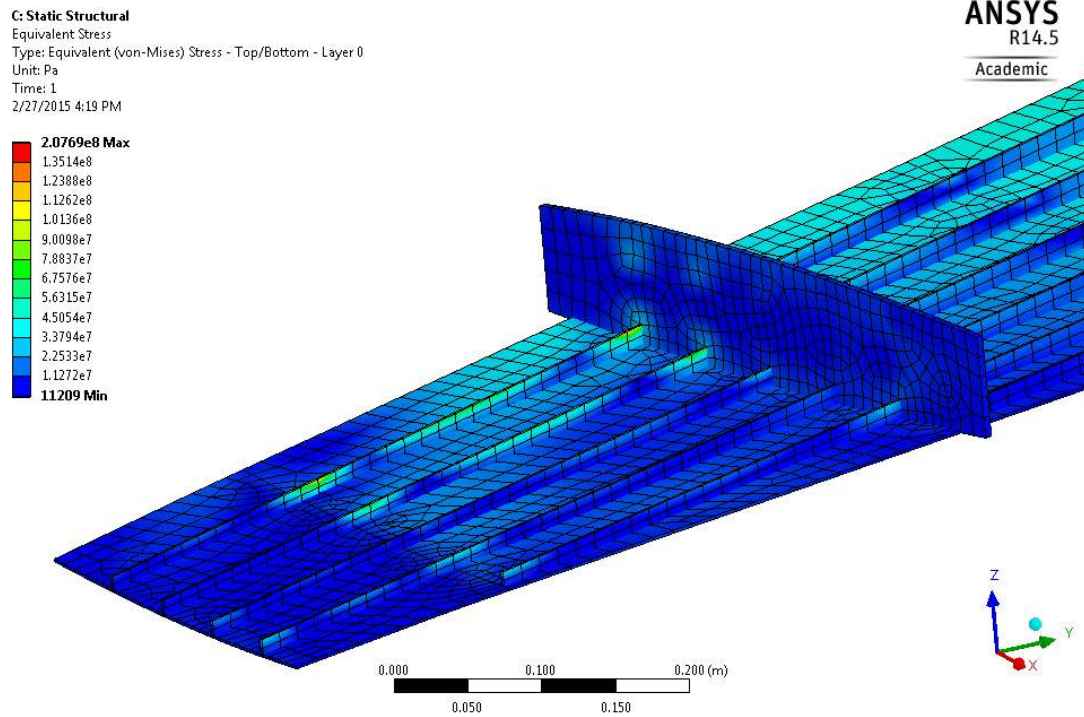
Figure 3.15. Stress concentrations at rib 15.

The differences in the results obtained for the four different meshes are not significant, proving mesh independence. Mesh 2 was chosen for the structural sizing analyses since it provided better accuracy than Mesh 1 at a low computational cost.

3.4   Mission Range Analysis Validation

The Falcon 10 Operational Instructions Manual (Avions Marcel Dassault - Breguet Aviation, 1993) reports a range of 2000 Nm and fuel burn for a mission climbing to 35,000 ft, cruise at Mach 0.75 and descent to the destination airport, taking off at MTOW and landing at MZFW without reserve, being 2000 Nm. Following the procedure described in section 2.4, the numerical calculation in this report gives 2000 Nm.

This good agreement gives confidence in the mission calculation method. However it should be noted that the mission calculated here uses the aerodynamic characteristics of the aircraft without horizontal tail therefore it will be slightly optimistic. A simplified sensitivity analysis shows that, in this calculation, a 1% increase in drag results in a 1% range reduction.

4. Results and Discussion

4.1 Effect of the Winglets on the Total Aircraft Drag

The combined effect of span and cant angle change is presented as carpet plots of change in the total drag $C_{D_{o_{tot}}}$ with respect to the baseline aircraft for lift coefficients representative of the top of climb and top of descent conditions.

The most significant changes are observed at Mach 0.7, top of climb, as this condition corresponds to the highest lift coefficients and thus to the highest induced drag for the baseline aircraft. Reductions in aircraft drag up to 9% are observed for the largest winglets. Reductions of up to 5.3% are obtained at Mach 0.8 top of climb and up to 2.8% at Mach 0.7 top of descent, again with the largest winglets.

Figure 4.2(b) shows that most of the winglets studied have a detrimental effect at Mach 0.8, top of descent, where the lift coefficient is relatively low and therefore the reduction in induced drag is exceeded by the increase in parasitic drag. It should be noted that winglet 2045 is marginally beneficial in terms of drag in that condition.

The results shown here correspond to expectations and published work, i.e. there is a break even point defined by the angle of attack at which the drag with winglet equals the drag without winglet. Under that break even point, the added parasite drag exceeds the induced drag reduction. It can also be seen that lower cant angle winglets tend to give larger drag reductions, favoring planar wingtip extensions. But
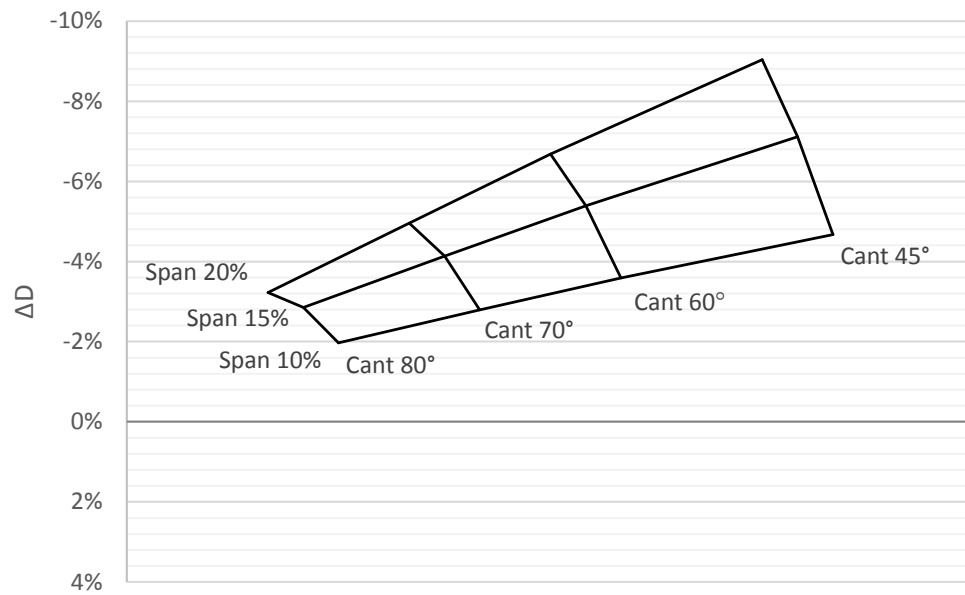
(a) $C_L = 0.40$.
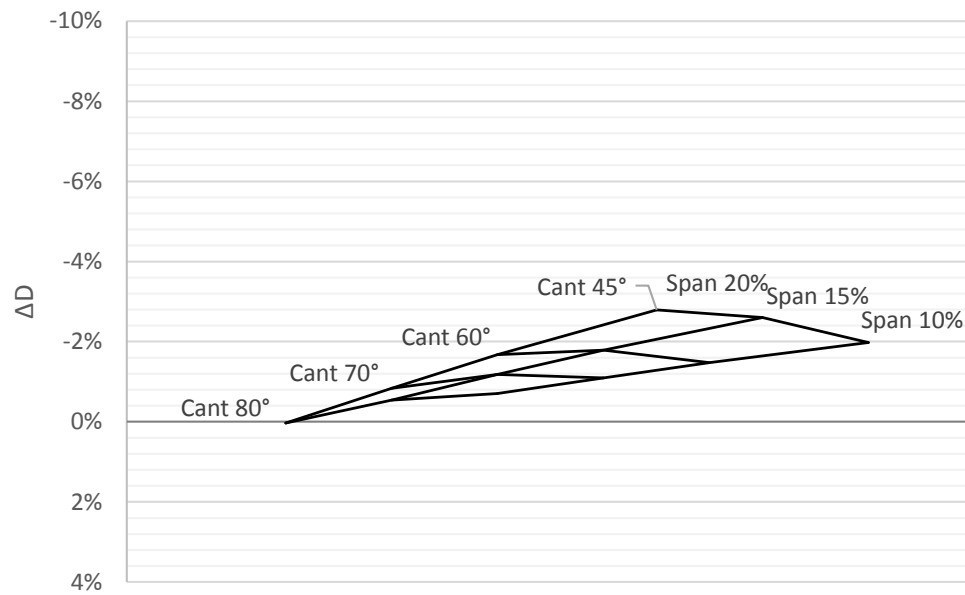
(b) $C_L = 0.29$.

Figure 4.1. Carpet plots of total drag reduction at Mach 0.7, constant C_L.
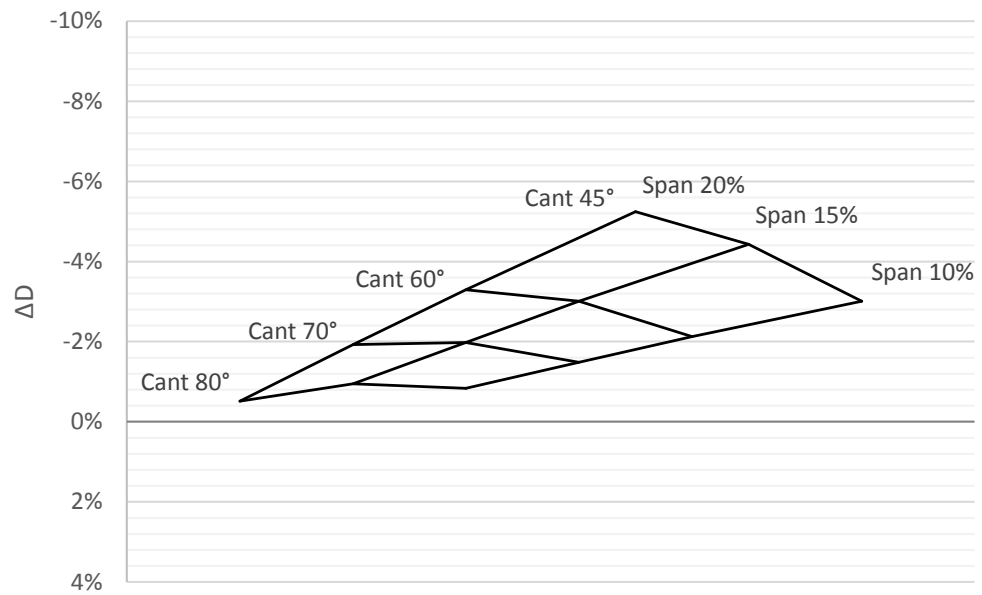
(a) $C_L = 0.32$.
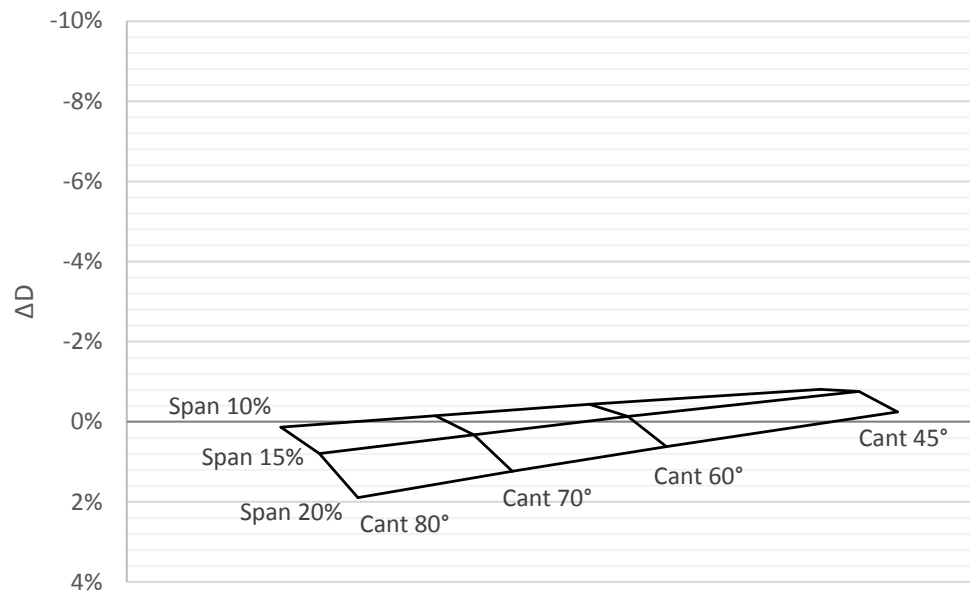
(b) $C_L = 0.25$.

Figure 4.2. Carpet plots of total drag reduction at Mach 0.8, constant C_L.

the total effect evaluation is incomplete without taking into account the changes in bending moments and weights.

4.2   Weight Increase

4.2.1   Winglets Weight

The winglet weights calculated as described in 2.2.1 are presented in Table 4.1. It should be noted that the weight is directly proportional to the winglet area and therefore larger winglets are heavier.

Table 4.1. Summary of winglet weights.

Winglet ID	Winglet Weight (lbs)
1045	62
1060	62
1070	62
1080	62
1545	114
1560	114
1570	114
1580	114
2045	176
2060	176
2070	176
2080	176

4.2.2   Structural Reinforcement

Figures 4.3 and 4.4 show the principal stresses in the wingbox skin for winglet 1545 for the loading conditions described in 2.2.2.

According to these figures, the gust condition is critical for the inboard part of the wing with winglets as found in the case of the baseline wing (Avions Marcel Dassault - Breguet Aviation, 1972). The roll condition however is not critical anymore when winglets are added because larger stresses occur for the outboard wing in the sideslip maneuver case.

The values of maximum principal stresses σ_1 in the upper skin and minimum principal stresses σ_3 in the lower skin are summarized in Table 4.2, where relatively high margins of safety are found for the 10% and 15% winglets. Reinforcement of the skin was only needed between ribs 15 and 16 for the 20% span winglets to meet the static strength requirements in the case of a sideslip maneuver condition.

Table 4.3 shows the new stresses in the reinforced skin panel between ribs 15 and 16. Positive static margins are now found for the 20% span winglets ensuring their ability to withstand the applied loads without failure.

Table 4.4 compares the minimum principal stresses in the skin panels to the critical buckling stresses for the different loading cases and winglets. The skin panels are identified by the rib right inboard of them. As shown on that table, extensive reinforcement was necessary to avoid buckling of the structure under sideslip maneuver loads.
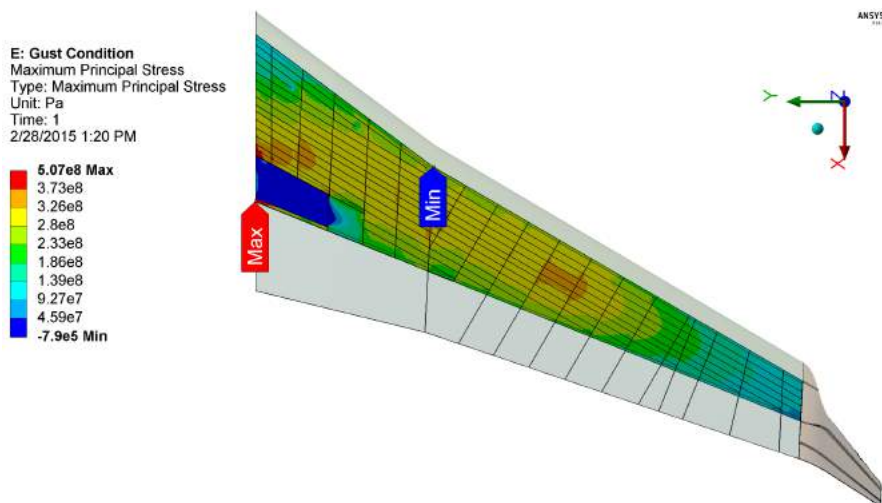
(a) Gust.
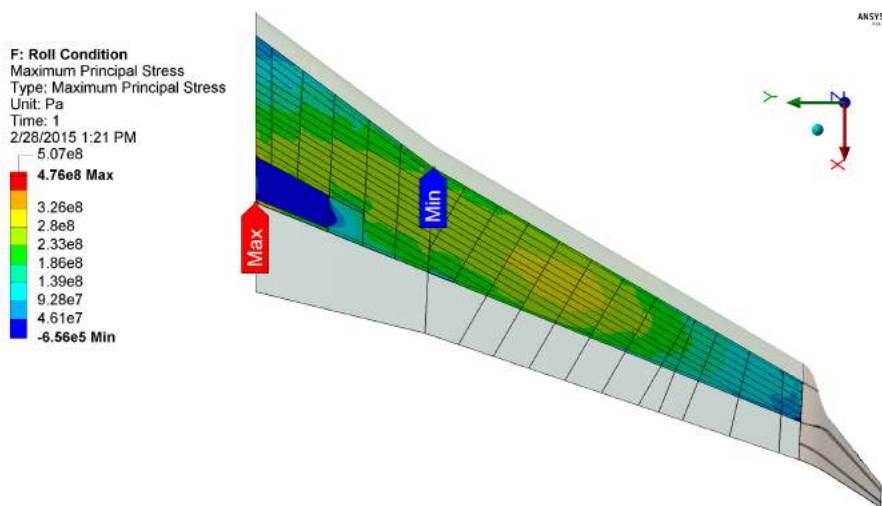
(b) Roll.
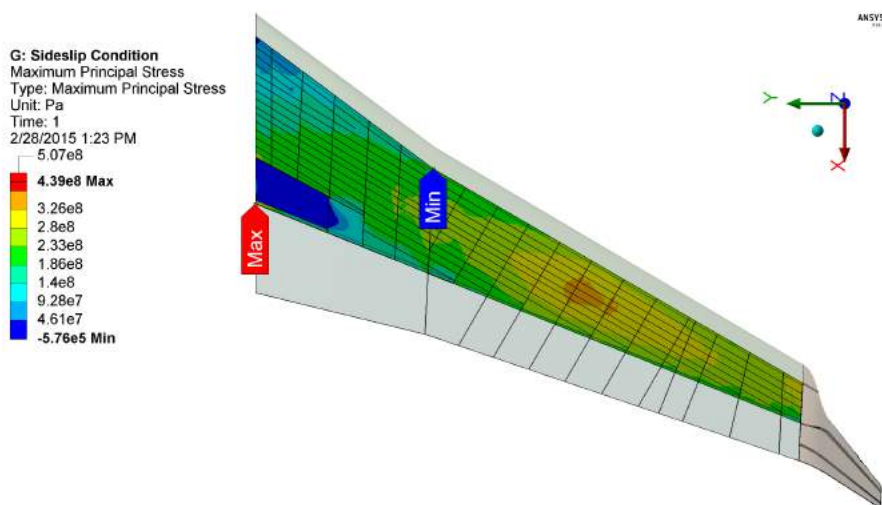
(c) Sideslip.

Figure 4.3. Contours of maximum principal stress for the winglet 1545 (lower skin).

(a) Gust.

(b) Roll.

(c) Sideslip.

Figure 4.4. Contours of minimum principal stress for the winglet 1545 (upper skin).

Table 4.2. Summary of the principal stresses, maximum shear stresses and margins of safety for the different winglets.

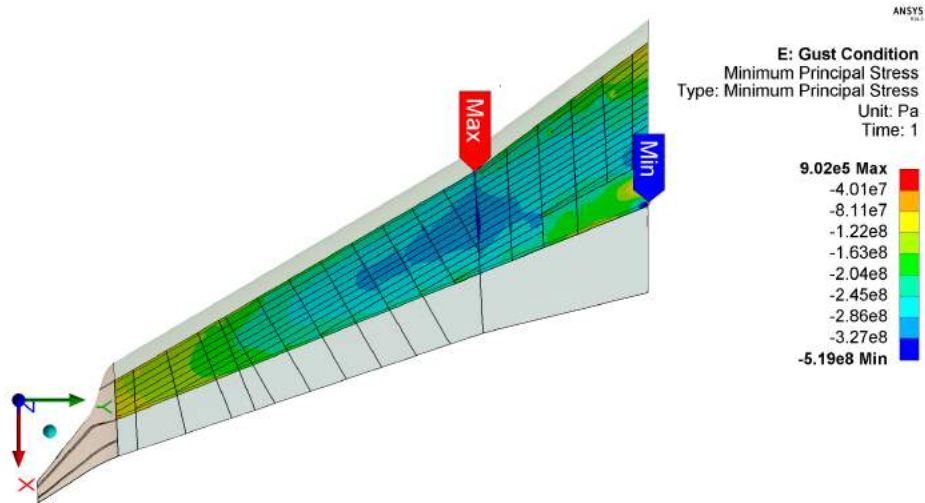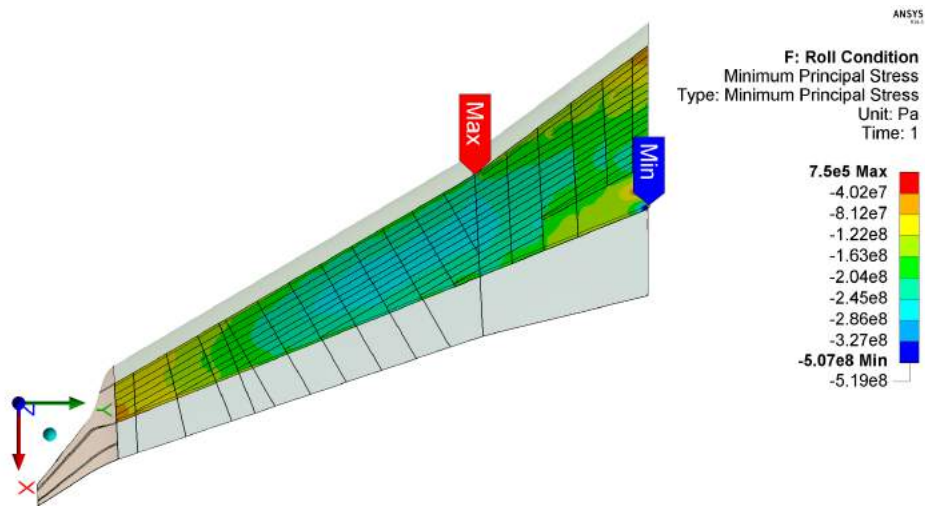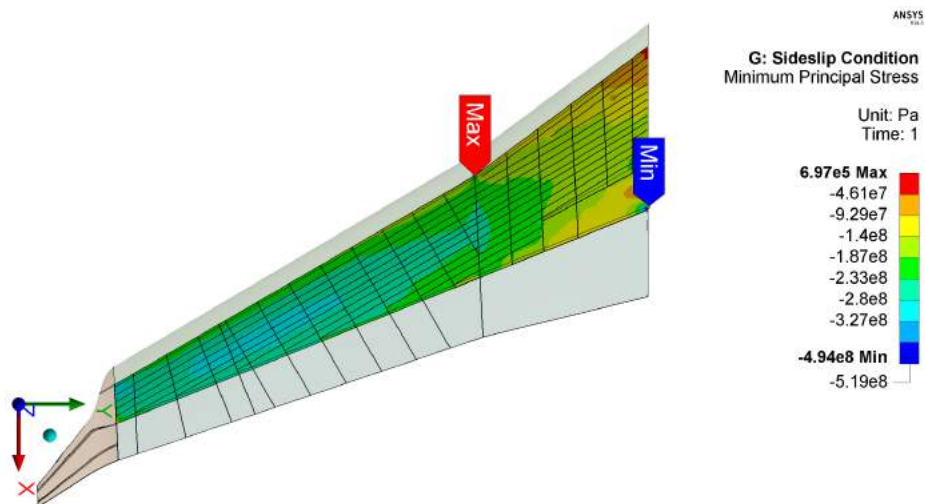|		Upper Skin		Lower Skin		Entire Wingbox	
		$\sigma_{1\ max\ (ksi)}$	MS	$\sigma_{3\ min\ (ksi)}$	MS	$\tau_{max\ (ksi)}$	MS
Tensile strength		68.2	-	-68.2	-	34.1	-
Yield Strength		60.9	-	-60.9	-	30.5	-
1045	Gust	47.6	0.43	-46.15	0.48	23.8	0.43
	Roll	38.9	0.75	-38.46	0.77	19.4	0.75
	Sideslip	31.6	1.16	-32.08	1.12	16.0	1.12
	MAX	✓ 48	✓ 0.43	✓ -46	✓ 0.48	✓ 24	✓ 0.43
1060	Gust	48.3	0.41	-46.89	0.45	24.1	0.41
	Roll	38.9	0.75	-38.90	0.75	19.5	0.75
	Sideslip	33.0	1.07	-33.54	1.03	16.8	1.03
	MAX	✓ 48	✓ 0.41	✓ -47	✓ 0.45	✓ 24	✓ 0.41
1070	Gust	46.6	0.46	-43.16	0.58	23.3	0.46
	Roll	37.7	0.81	-36.28	0.88	18.8	0.81
	Sideslip	30.9	1.20	-28.77	1.37	24.0	0.42
	MAX	✓ 47	✓ 0.46	✓ -43	✓ 0.58	✓ 24	✓ 0.42
1080	Gust	45.5	0.50	-41.13	0.66	22.8	0.50
	Roll	37.0	0.84	-34.86	0.96	18.5	0.84
	Sideslip	26.6	1.56	-25.16	1.71	13.3	1.56
	MAX	✓ 46	✓ 0.50	✓ -41	✓ 0.66	✓ 23	✓ 0.50
1545	Gust	52.5	0.30	-50.33	0.35	26.3	0.30
	Roll	46.8	0.46	-42.50	0.60	23.4	0.46
	Sideslip	56.4	0.21	-61.02	0.12	30.5	0.12
	MAX	✓ 56	✓ 0.21	✓ -61	✓ 0.12	✓ 31	✓ 0.12
1560	Gust	49.8	0.37	-47.87	0.42	24.9	0.37
	Roll	42.4	0.61	-39.47	0.73	21.2	0.61
	Sideslip	57.4	0.19	-58.64	0.16	29.3	0.16
	MAX	✓ 57	✓ 0.19	✓ -59	✓ 0.16	✓ 29	✓ 0.16
1570	Gust	48.0	0.42	-45.78	0.49	24.0	0.42
	Roll	40.1	0.70	-37.83	0.80	20.0	0.70
	Sideslip	53.3	0.28	-55.68	0.22	27.8	0.22
	MAX	✓ 53	✓ 0.28	✓ -56	✓ 0.22	✓ 28	✓ 0.22
1580	Gust	46.4	0.47	-43.51	0.57	23.2	0.47
	Roll	38.5	0.77	-36.52	0.87	19.2	0.77
	Sideslip	49.7	0.37	-48.34	0.41	27.2	0.25
	MAX	✓ 50	✓ 0.37	✓ -48	✓ 0.41	✓ 27	✓ 0.25
2045	Gust	59.5	0.15	-55.30	0.23	29.7	0.15
	Roll	51.6	0.32	-44.72	0.52	25.8	0.32
	Sideslip	85.9	-0.21	-87.39	-0.22	43.7	-0.22
	MAX	✗ 86	✗ -0.21	✗ -87	✗ -0.22	✗ 44	✗ -0.22
2060	Gust	54.6	0.25	-51.57	0.32	27.3	0.25
	Roll	46.3	0.47	-42.32	0.61	23.1	0.47
	Sideslip	90.8	-0.25	-88.01	-0.23	45.4	-0.25
	MAX	✗ 91	✗ -0.25	✗ -88	✗ -0.23	✗ 45	✗ -0.25
2070	Gust	50.9	0.34	-48.16	0.42	25.4	0.34
	Roll	42.9	0.59	-39.56	0.72	21.4	0.59
	Sideslip	88.7	-0.23	-85.79	-0.21	44.4	-0.23
	MAX	✗ 89	✗ -0.23	✗ -86	✗ -0.21	✗ 44	✗ -0.23
2080	Gust	47.9	0.42	-46.83	0.46	23.9	0.42
	Roll	39.6	0.72	-39.21	0.74	19.8	0.72
	Sideslip	81.1	-0.16	-79.36	-0.14	40.6	-0.16
	MAX	✗ 81	✗ -0.16	✗ -79	✗ -0.14	✗ 41	✗ -0.16

Table 4.3. Summary of the principal stresses, maximum shear stresses and margins of safety for the reinforced skin.

ID	Thickness	Load	Upper Skin		Lower Skin		Entire Wingbox	
			$\sigma1$ max (ksi)	MS	$\sigma3$ min (ksi)	MS	τmax (ksi)	MS
2045	Upper Skin	Gust	59.5	0.15	-55.30	0.23	29.7	0.15
	1.8 mm	Roll	51.6	0.32	-44.72	0.52	25.8	0.32
	Lower Skin	Sideslip	65.4	0.04	-66.80	0.02	33.4	0.02
	1.8 mm	**MAX**	65	0.04	-67	0.02	33	0.02
2060	Upper Skin	Gust	54.6	0.25	-51.57	0.32	27.3	0.25
	1.9 mm	Roll	46.3	0.47	-42.32	0.61	23.1	0.47
	Lower Skin	Sideslip	66.6	0.02	-66.59	0.02	32.6	0.05
	1.8 mm	**MAX**	67	0.02	-67	0.02	33	0.05
2070	Upper Skin	Gust	50.9	0.34	-48.16	0.42	25.4	0.34
	1.8 mm	Roll	42.9	0.59	-39.56	0.72	21.4	0.59
	Lower Skin	Sideslip	67.0	0.02	-66.98	0.02	33.5	0.02
	1.8 mm	**MAX**	67	0.02	-67	0.02	33	0.02
2080	Upper Skin	Gust	47.9	0.42	-46.83	0.46	23.9	0.42
	1.7 mm	Roll	19.8	2.45	-39.21	0.74	19.8	0.72
	Lower Skin	Sideslip	67.1	0.02	-65.96	0.03	32.9	0.03
	1.6 mm	**MAX**	67	0.02	-66	0.03	33	0.03

The total reinforcement weight is presented for each winglet configuration in Table 4.5. As expected, the larger the winglet and the larger the cant angle, the heavier the reinforcement needed, since the winglet lift adds up to the bending moments due to the sideslip angle. However, it must however be noted that the maximum cant angle considered here is 45° and that this conclusion may no longer be valid for lower cant angles, as the winglet bending moments due to sideslip will become negligible.

The extent of the reinforcement for winglet 1545 is shown in Figure 4.5, where the added stiffeners are represented in red. Details are given in Table 4.6. It should be noted that the panels between rib 16 and rib 17 are not reinforced, that portion of the wing is part of the tip fairing that would be removed and replaced by the winglet

Table 4.4. Summary of the minimum principal stresses and critical buckling stresses in the upper skin panels (ksi).

		N1	N3	N5	N7	N8	N9	N10	N11	N12	N13	N14	N15
Baseline σcr		-54.1	-55.6	-53.7	-54.1	-53.0	-52.3	-51.4	-44.3	-36.2	-36.6	-25.3	-16.2
1045	Gust	-37.9	-36.8	-46.1	-38.4	-37.9	-38.0	-35.0	-31.9	-27.7	-23.6	-20.4	-20.7
	Roll	-29.7	-29.4	-38.5	-33.8	-33.8	-34.7	-32.6	-29.9	-26.7	-22.9	-19.2	-18.0
	Sideslip	-21.5	-20.6	-26.5	-24.7	-24.7	-26.5	-26.4	-26.4	-26.0	-24.5	-24.4	-32.1
	MAX	-37.9	-36.8	-46.1	-38.4	-37.9	-38.0	-35.0	-31.9	-27.7	-24.5	-24.4	-32.1
1060	Gust	-37.1	-37.1	-46.9	-38.9	-37.3	-37.1	-34.1	-30.7	-26.5	-22.3	-18.4	-18.3
	Roll	-27.7	-29.0	-38.9	-32.8	-32.6	-33.6	-32.1	-29.0	-26.1	-21.9	-17.7	-16.3
	Sideslip	-19.3	-20.3	-26.7	-25.5	-25.7	-27.1	-27.3	-27.0	-26.5	-25.4	-24.8	-33.5
	MAX	-37.1	-37.1	-46.9	-38.9	-37.3	-37.1	-34.1	-30.7	-26.5	-25.4	-24.8	-33.5
1070	Gust	-36.7	-36.4	-43.2	-37.7	-36.0	-35.2	-32.2	-29.0	-25.1	-20.5	-16.6	-15.9
	Roll	-30.2	-28.7	-36.3	-33.1	-32.6	-33.1	-30.6	-29.0	-25.2	-20.9	-16.5	-14.5
	Sideslip	-19.3	-20.2	-25.7	-24.4	-24.4	-24.9	-25.2	-24.5	-24.4	-23.2	-22.5	-28.8
	MAX	-36.7	-36.4	-43.2	-37.7	-36.0	-35.2	-32.2	-29.0	-25.2	-23.2	-22.5	-28.8
1080	Gust	-35.2	-35.2	-41.1	-36.1	-34.5	-32.5	-30.5	-27.0	-23.1	-18.3	-14.6	-13.7
	Roll	-26.8	-28.0	-34.9	-31.5	-31.0	-31.9	-29.3	-27.1	-23.8	-18.9	-15.3	-12.9
	Sideslip	-16.8	-18.3	-22.6	-21.2	-21.2	-22.0	-21.8	-21.0	-20.6	-19.4	-19.0	-25.2
	MAX	-35.2	-35.2	-41.1	-36.1	-34.5	-32.5	-30.5	-27.1	-23.8	-19.4	-19.0	-25.2
1545	Gust	-41.2	-41.2	-50.3	-44.8	-43.5	-44.7	-41.6	-38.3	-35.0	-30.7	-27.4	-30.3
	Roll	-31.3	-32.8	-42.5	-38.9	-38.6	-39.5	-38.0	-36.1	-33.5	-29.0	-24.9	-25.5
	Sideslip	-26.1	-28.6	-37.0	-36.3	-38.1	-41.0	-42.1	-42.8	-43.7	-43.5	-43.5	-61.0
	MAX	-41.2	-41.2	-50.3	-44.8	-43.5	-44.7	-42.1	-42.8	-43.7	-43.5	-43.5	-61.0
1560	Gust	-40.0	-39.2	-47.9	-41.5	-39.9	-39.5	-37.7	-34.8	-30.9	-26.8	-23.2	-25.2
	Roll	-29.9	-30.5	-39.5	-36.0	-35.5	-36.7	-35.1	-33.1	-29.6	-25.4	-21.3	-21.2
	Sideslip	-25.5	-28.6	-37.0	-35.2	-36.0	-39.0	-39.9	-40.6	-41.9	-41.6	-43.1	-58.6
	MAX	-40.0	-39.2	-47.9	-41.5	-39.9	-39.5	-39.9	-40.6	-41.9	-41.6	-43.1	-58.6
1570	Gust	-37.9	-37.3	-45.8	-39.0	-37.7	-37.9	-35.0	-31.6	-27.3	-23.8	-20.2	-21.1
	Roll	-28.3	-29.4	-37.8	-33.1	-33.5	-34.8	-32.9	-30.7	-27.7	-22.9	-19.0	-18.7
	Sideslip	-23.6	-25.1	-32.3	-31.8	-32.8	-35.7	-35.8	-38.0	-37.0	-37.4	-38.9	-55.7
	MAX	-37.9	-37.3	-45.8	-39.0	-37.7	-37.9	-35.8	-38.0	-37.0	-37.4	-38.9	-55.7
1580	Gust	-36.5	-36.0	-43.5	-36.3	-35.2	-35.4	-31.9	-29.2	-25.4	-20.6	-17.0	-17.1
	Roll	-27.7	-28.7	-36.5	-32.1	-31.6	-32.5	-31.3	-28.3	-25.4	-20.9	-16.8	-15.5
	Sideslip	-23.6	-25.2	-32.2	-30.0	-31.2	-33.2	-33.6	-34.2	-34.5	-34.1	-34.5	-48.3
	MAX	-36.5	-36.0	-43.5	-36.3	-35.2	-35.4	-33.6	-34.2	-34.5	-34.1	-34.5	-48.3
2045	Gust	-42.2	-48.0	-55.3	-49.3	-48.2	-49.6	-47.4	-45.8	-43.5	-38.6	-37.4	-34.2
	Roll	-32.6	-34.5	-44.7	-40.3	-40.2	-33.4	-41.0	-41.0	-38.1	-33.4	-31.0	-26.7
	Sideslip	-33.5	-38.0	-51.6	-50.6	-55.1	-59.3	-61.2	-60.6	-61.4	-61.8	-62.8	-66.8
	MAX	-42.2	-48.0	-55.3	-50.6	-55.1	-59.3	-61.2	-60.6	-61.4	-61.8	-62.8	-66.8
2060	Gust	-41.2	-39.2	-51.6	-43.2	-43.2	-44.7	-41.5	-40.0	-36.8	-32.2	-30.1	-27.0
	Roll	-30.6	-31.2	-42.3	-38.1	-37.7	-39.7	-38.1	-36.1	-33.5	-29.3	-25.8	-21.8
	Sideslip	-32.3	-37.4	-50.6	-49.0	-52.9	-57.9	-59.3	-60.6	-60.5	-61.1	-63.5	-66.6
	MAX	-41.2	-39.2	-51.6	-49.0	-52.9	-57.9	-59.3	-60.6	-60.5	-61.1	-63.5	-66.6
2070	Gust	-39.2	-39.2	-48.2	-40.5	-40.5	-38.7	-38.4	-36.0	-32.5	-28.4	-25.6	-22.7
	Roll	-27.3	-29.7	-39.6	-35.4	-34.4	-36.1	-35.7	-32.3	-30.3	-26.1	-22.5	-18.8
	Sideslip	-29.4	-33.8	-46.1	-43.7	-47.7	-51.3	-50.0	-56.9	-60.0	-60.8	-62.2	-67.0
	MAX	-39.2	-39.2	-48.2	-43.7	-47.7	-51.3	-50.0	-56.9	-60.0	-60.8	-62.2	-67.0
2080	Gust	-37.3	-37.4	-46.8	-38.0	-36.7	-36.8	-35.1	-31.8	-27.6	-23.8	-21.0	-18.9
	Roll	-27.8	-29.4	-39.2	-33.1	-32.9	-34.4	-32.8	-30.5	-27.1	-22.9	-19.3	-20.1
	Sideslip	-26.4	-29.2	-39.7	-38.1	-38.7	-43.9	-44.8	-48.7	-50.0	-52.2	-58.6	-66.0
	MAX	-37.3	-37.4	-46.8	-38.1	-38.7	-43.9	-44.8	-48.7	-50.0	-52.2	-58.6	-66.0

structure. The weight of that portion of the wing is hence included in the winglet weight.

Table 4.5. Summary of wing reinforcement weight.

Winglet ID	Stiffeners (lb)	Skin (lb)	Fasteners (lb)	Total (lb)
1045	2.051	0	1.025	3.076
1060	2.087	0	1.044	3.131
1070	1.673	0	0.837	2.510
1080	1.582	0	0.791	2.373
1545	8.334	0	4.167	12.500
1560	7.935	0	3.967	11.902
1570	6.138	0	3.069	9.208
1580	4.119	0.	2.060	6.179
2045	25.557	1.182	13.369	38.926
2060	21.831	1.294	11.563	33.394
2070	14.439	1.207	7.823	22.262
2080	11.615	0.918	6.267	17.882

Table 4.6. Details of wingbox reinforcement for winglet 1545.

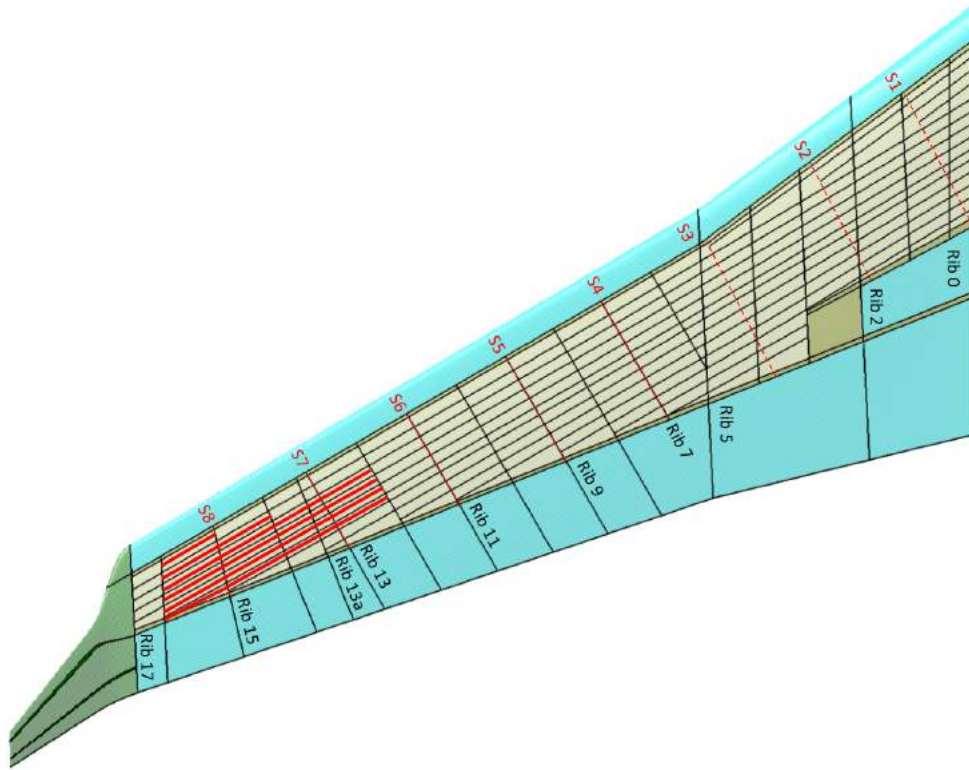| Rib	Nb of Added Stiffeners	Stiffeners Height (in)	Maximum Height (in)	New σ_{cr} (ksi)
15	6	0.795	0.709	-47.22
14	5	0.740	0.768	-37.88
13	4	0.689	0.795	-41.38
12	4	0.780	0.854	-41.61

Figure 4.5. Extent of the wingbox reinforcement for winglet 1545.

4.3 Winglets Cruise Range Comparison

The range was calculated, as described in section 2.3, at altitudes of 35,000 ft and 40,000 ft for cruises at Mach 0.7 and 0.8. The results are presented in the form of carpet plots in Figures 4.6 and 4.7.

The overall shape of these carpet plots is similar to that of the drag reduction carpet plots, however, a few differences are worth mentioning. While the largest winglets give the highest induced drag reduction, they do not necessarily give the highest range increase. At Mach 0.7, 40,000 ft, winglet 2045 outperforms its competitors, but it does not add any benefit compared to winglet 1545 for the other cruise conditions
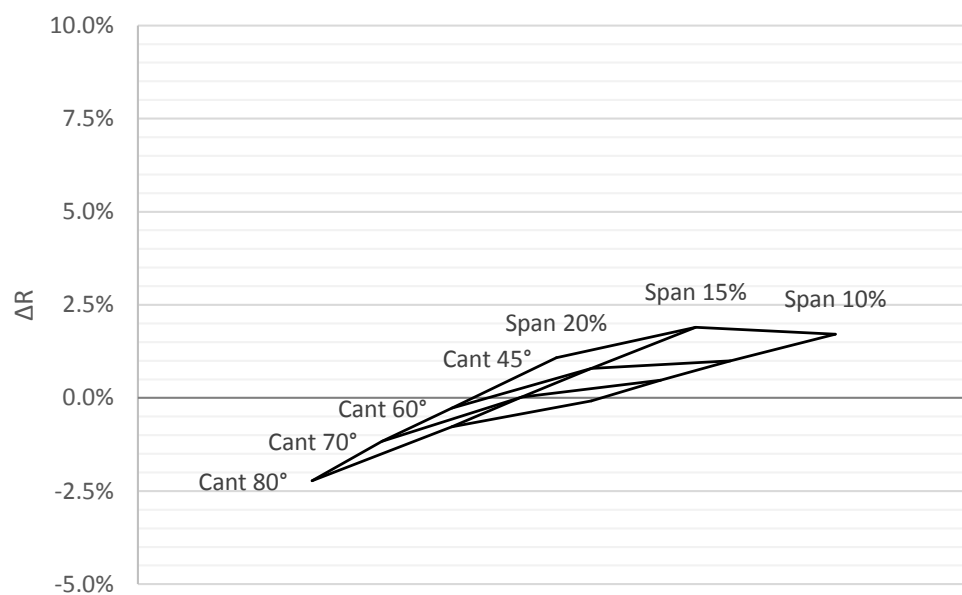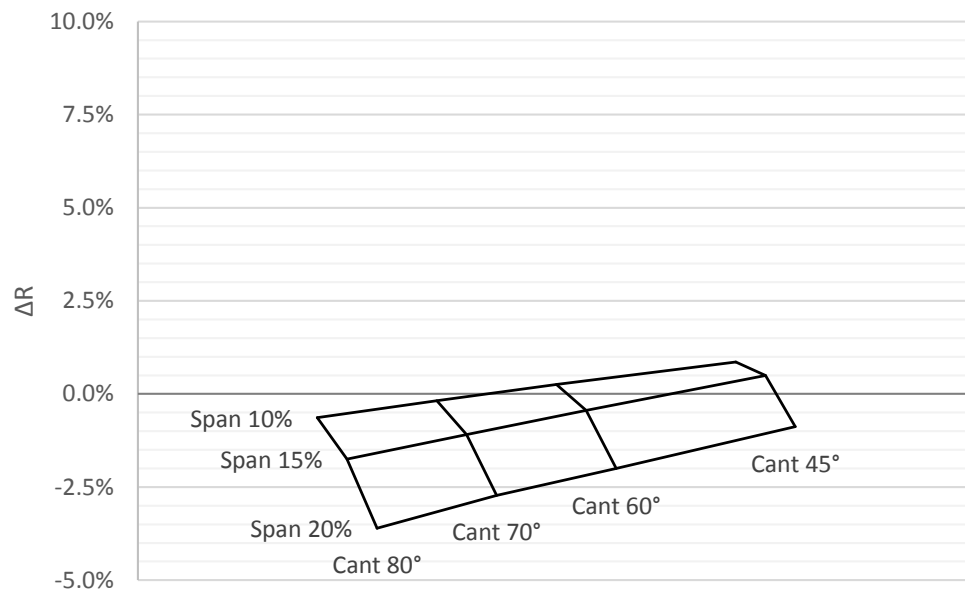
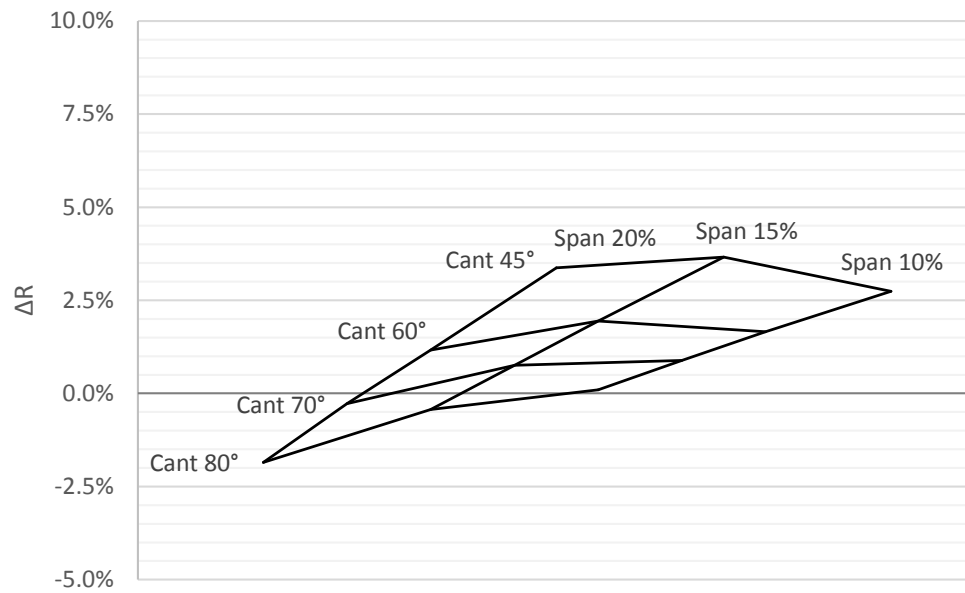(a) Altitude 35,000 ft.
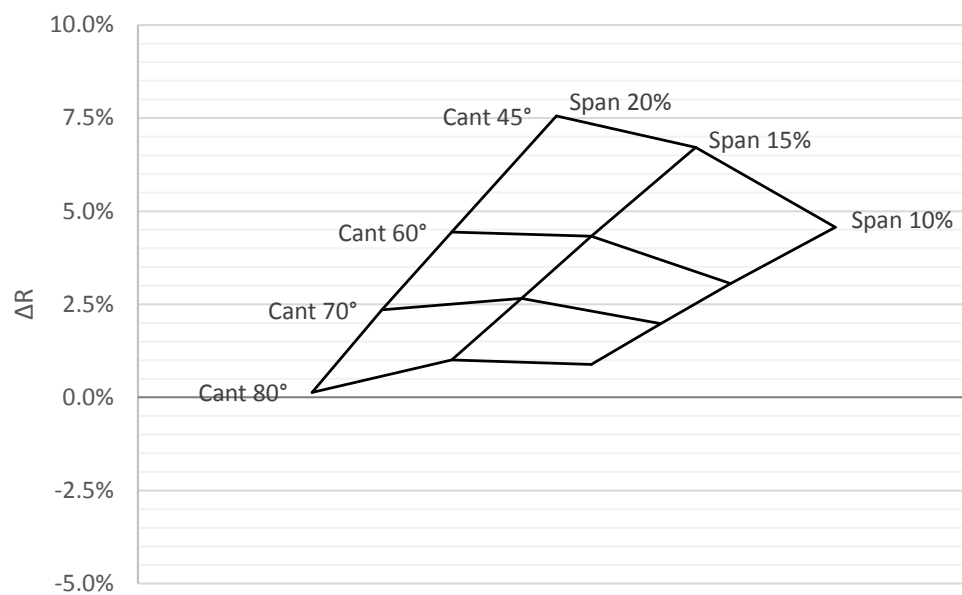
(b) Altitude 40,000 ft.

Figure 4.6. Carpet plots of cruise range increase at Mach 0.7, constant altitude.

(a) Altitude 35,000 ft.

(b) Altitude 40,000 ft.

Figure 4.7. Carpet plots of cruise range increase at Mach 0.8, constant altitude.

evaluated. Furthermore, it is clearly detrimental at Mach 0.8, 35,000 ft, while winglet 1545 has almost a zero net effect.

Additionally, it was shown in section 4.2.2 that winglet 2045 would require extensive reinforcement thus increasing significantly the cost of a retrofit. Therefore, winglet 1545 was selected as the best configuration and for more refined analysis.

4.4 Selected Winglet Geometry

Based on the cruise range analysis presented earlier the best candidate is the winglet 1545, which geometry is presented in Figure 4.8.

4.5 Selected Winglet Aerodynamics

For winglet 1545, detailed RANS analyses were performed at Mach 0.7 and 0.8 for a range of angles of attack to produce accurate drag polars and to determine whether there were any compressibility issues (particularly shockwaves) requiring design refinements.

The results of these simulations are presented in Figures 4.9 and 4.10. For a typical cruise lift coefficient, there is a drag reduction (Table 4.7).

Table 4.7. Net drag reduction at typical cruise lift coefficients - CFD.

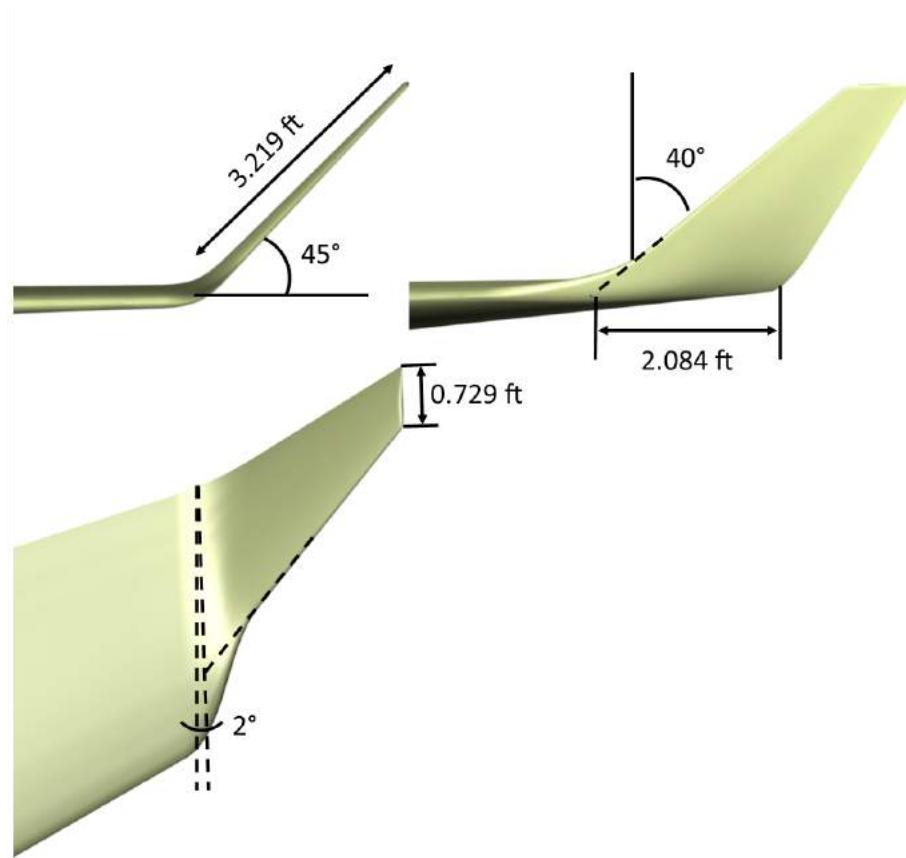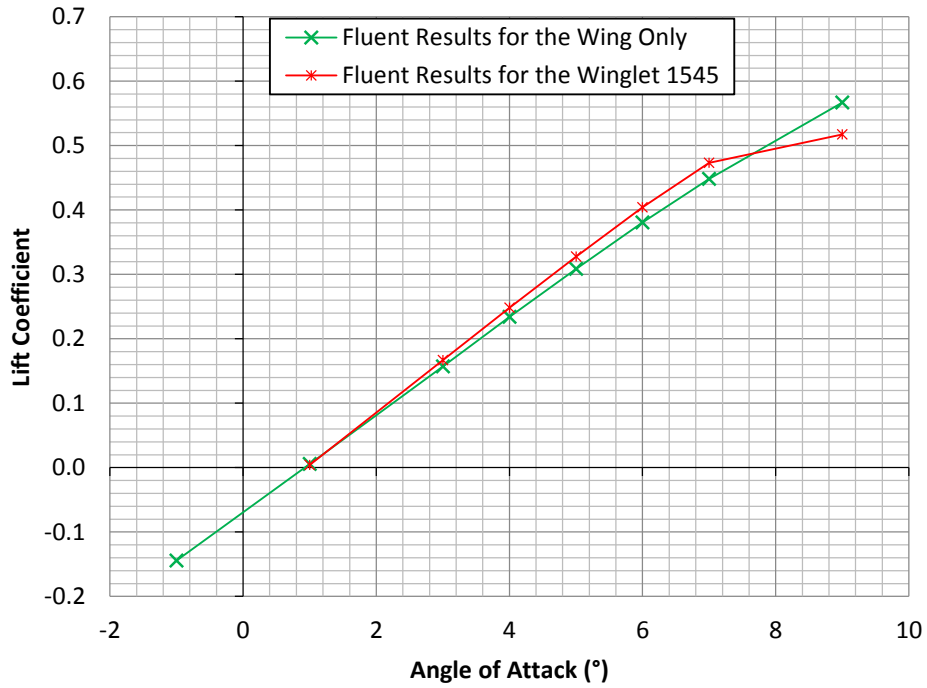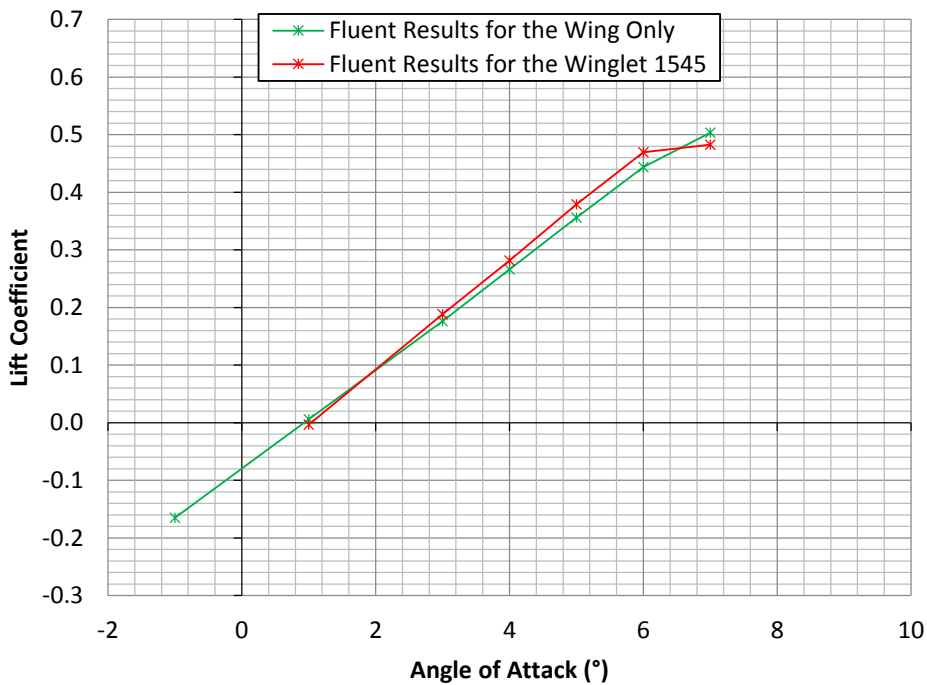| Mach	0.7			0.8		
C_L	0.40	0.345	0.29	0.32	0.285	0.25
ΔC_D	-4.6%	-4.8%	-1.5%	-3.3%	-2.5%	-0.4%

Figure 4.8. Geometry of the best winglet configuration.

No shockwaves or separation occurred on the winglet before appearing on the baseline wing. Figures 4.12 and 4.13 show pressure coefficient contours, streamlines, shockwaves (in red), tip vortex cores (in green), separation and attachment lines (in purple and yellow respectively). At Mach 0.7 a shockwave starts to form on the baseline wing at $\alpha = 5°$ but not on the winglet or on the blend region. A shockwave starts to form on the winglet at $\alpha = 7°$ when the wing shockwave is already well established. Similarly, at Mach 0.8, a shock starts to form on the winglet at $\alpha = 7°$ while the wing shockwave is already large. A region of separation appears behind
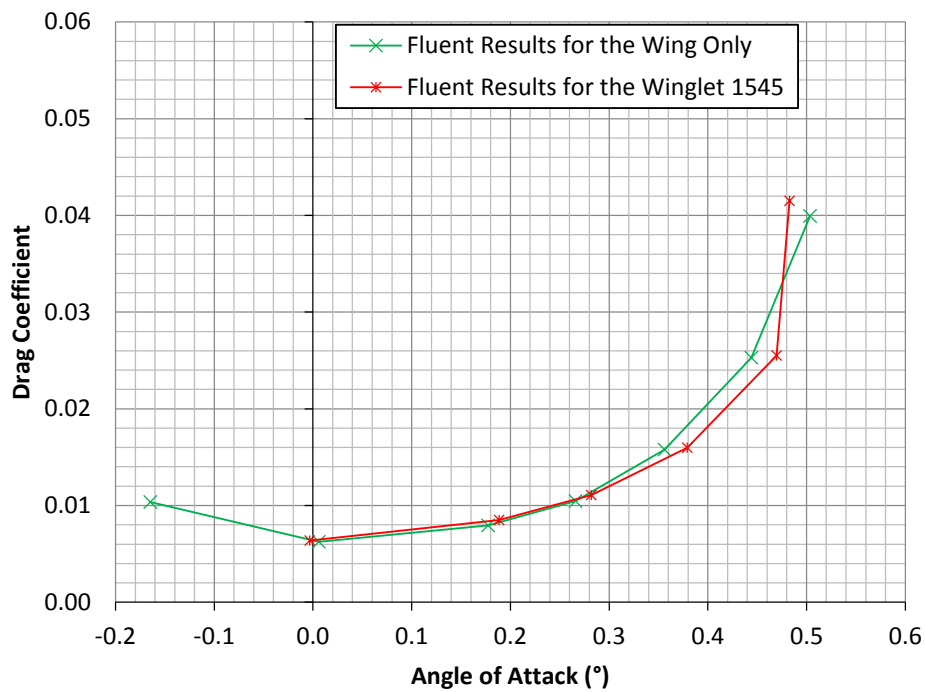
(a) Mach 0.7

(b) Mach 0.8

Figure 4.9. Lift coefficients vs. angle of attack at Mach 0.7 and 0.8 for wing with and without winglet (RANS).
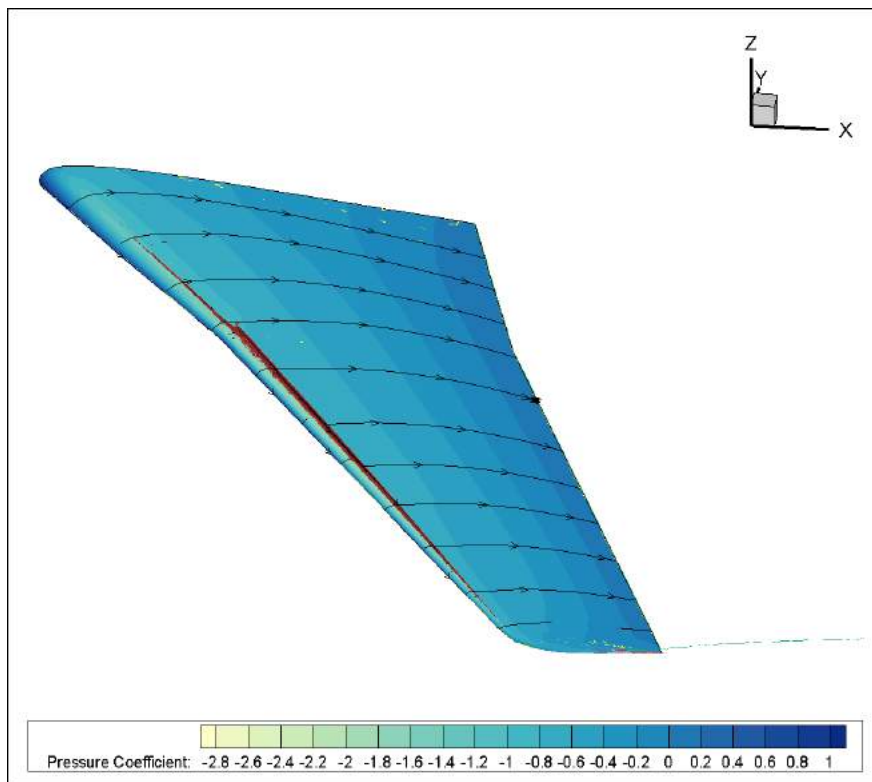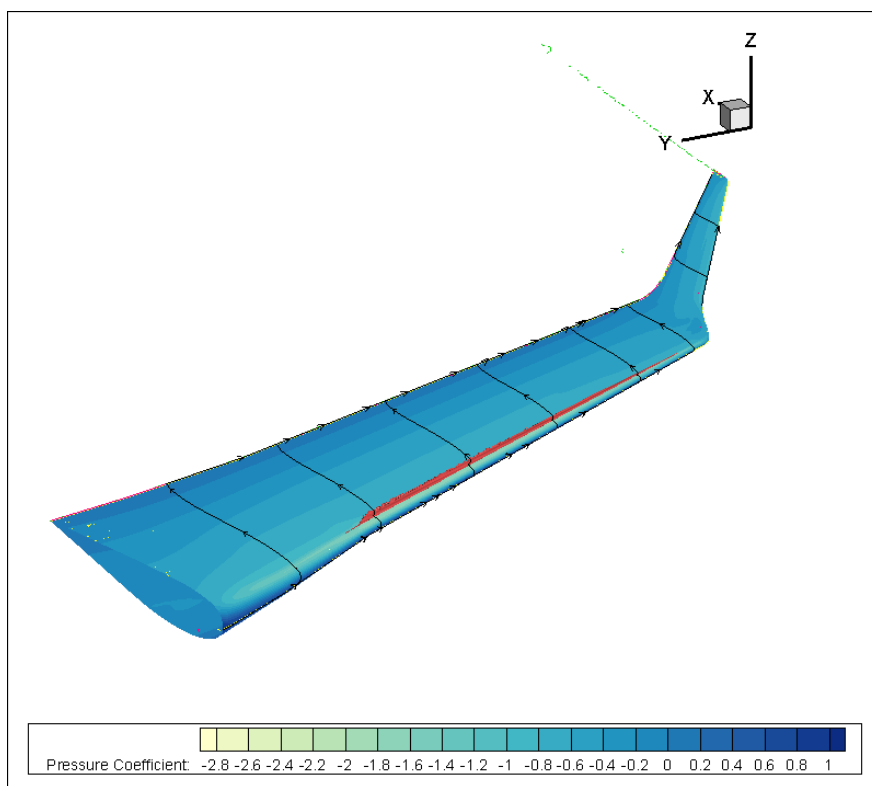
(a) Mach 0.7

(b) Mach 0.8

Figure 4.10. Drag coefficient vs. lift coefficient at Mach 0.7 and 0.8 for wing with and without winglet (RANS).

(a) Baseline wing

(b) Winglet 1545

Figure 4.11. Pressure contours for wing with and without winglet at Mach 0.7, $\alpha = 5\,\text{deg}$ (RANS).
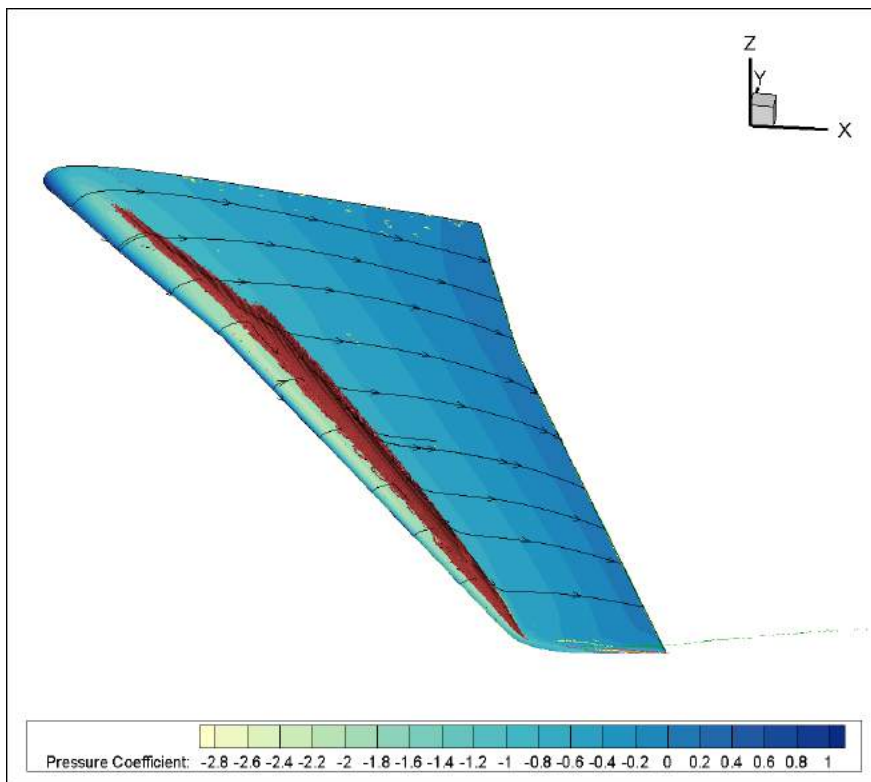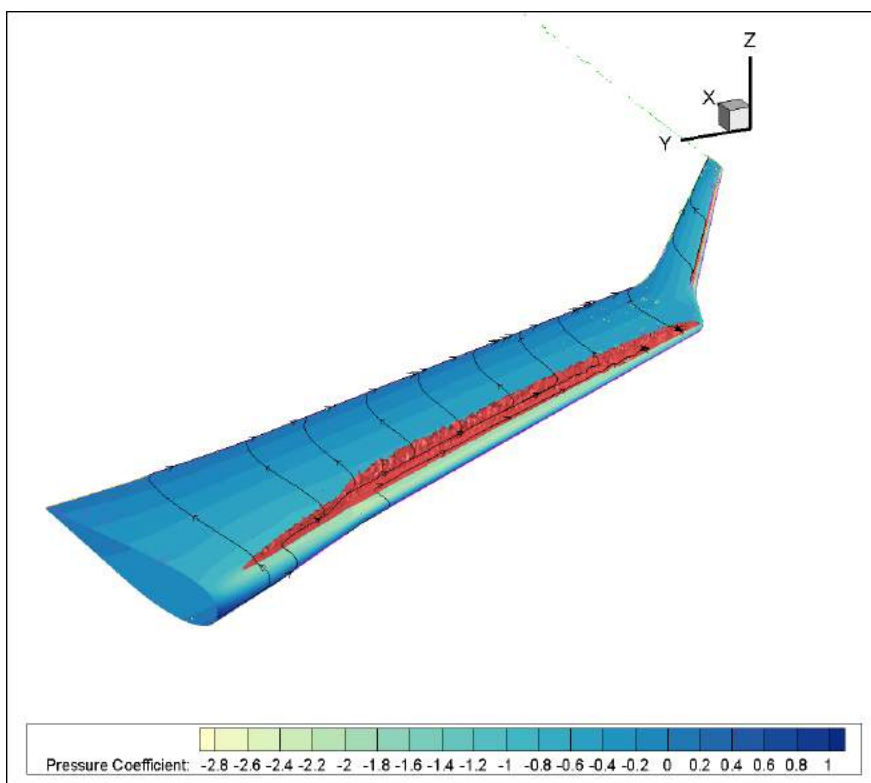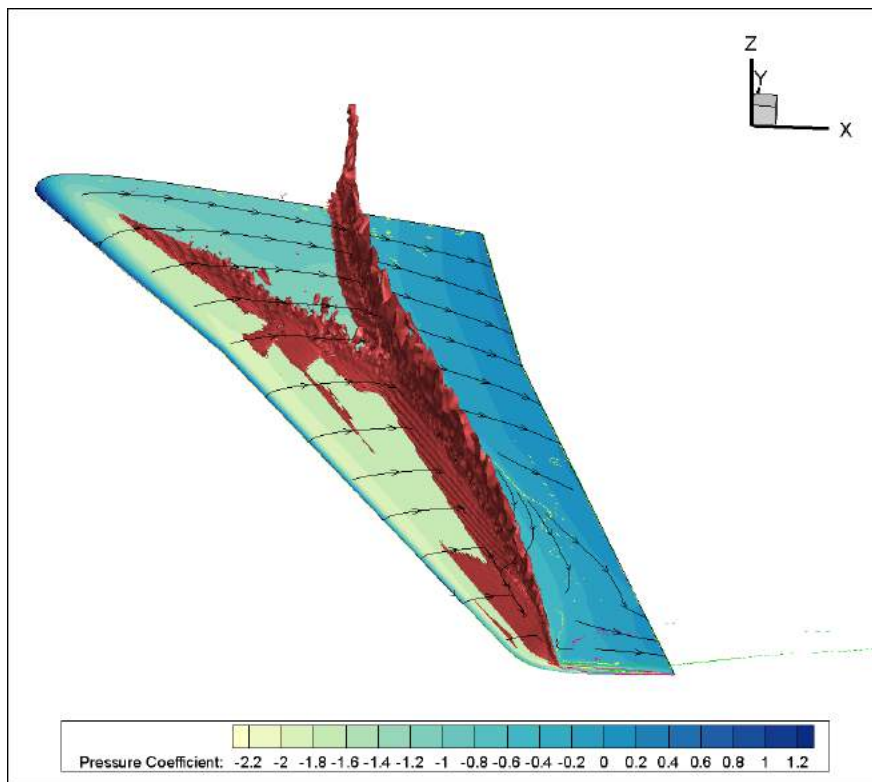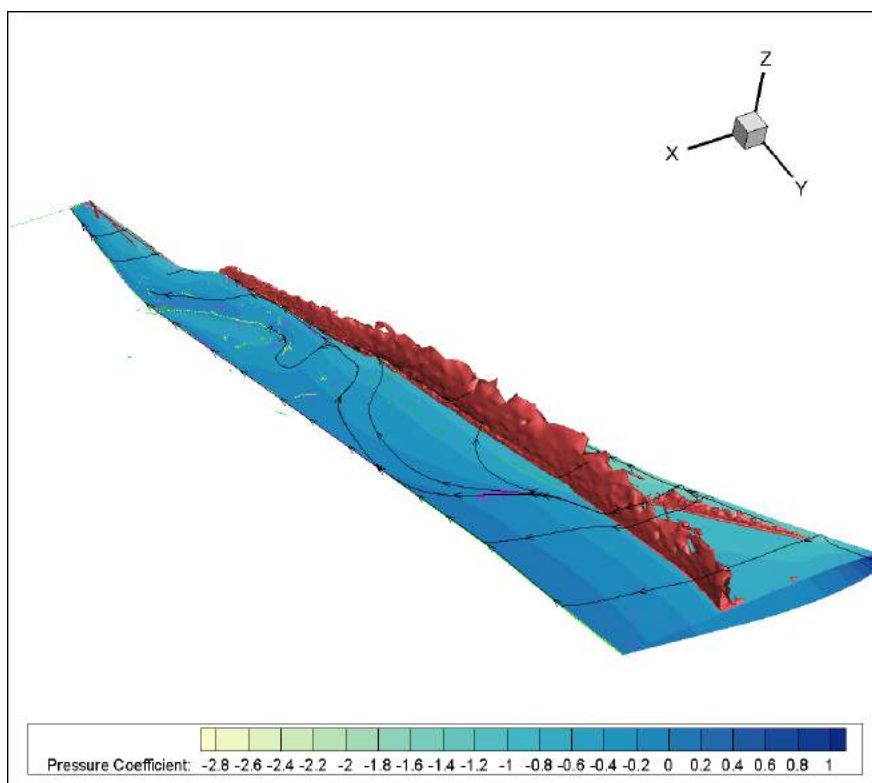
(a) Baseline wing

(b) Winglet 1545

Figure 4.12. Pressure contours for wing with and without winglet at Mach 0.7, $\alpha = 7$ deg (RANS).

(a) Baseline wing

(b) Winglet 1545

Figure 4.13. Pressure contours for wing with and without winglet at Mach 0.7, $\alpha = 7\,\mathrm{deg}$ (RANS).

the shock on the wing but the flow stays attached on the winglet. Therefore, it is concluded that the winglet does not have any detrimental effect due to interference or shock formation at operational Mach numbers.

4.6   Full Mission Analysis

Knowing the change in lift and drag coefficients $\Delta C_L\left(\alpha\right)$ and $\Delta C_D\left(\alpha\right)$ due to the winglets, the mission presented in 2.4 was calculated for the aircraft with and without winglets. The results are summarized in Table 4.6 and in Figure 4.14.

The best range improvement is about 101 Nm, i.e. 7.0% of the original value, for a cruise at Mach 0.7 at 40,000 ft. However, the aircraft would not normally cruise at 40,000 ft when taking off at MTOW. That altitude is close to the aircraft operating ceiling which means that the rate of climb, when approaching 40,000 ft is significantly reduced. The aircraft burns more fuel to reach 40,000 ft reducing the amount of fuel available for cruise. For a cruise at Mach 0.8, the altitude of 40,000 ft is recommended and the winglet increases the aircraft range by 4.4%. For a cruise at 35,000 ft, the winglet slightly improves the aircraft range. The best range is accomplished at Mach 0.7 and 35,000ft. The fuel savings for a 1200 Nm mission, taking off at MTOW, are presented in Table 4.6 and Figure 4.15. The winglet allows the aircraft to save up to 8% of fuel.

Table 4.8. Mission analysis results - range.

	No WL	WL1545	No WL	WL1545	No WL	WL1545	No WL	WL1545
Cruise Mach	0.7	0.7	0.7	0.7	0.8	0.8	0.8	0.8
Cruise Altitude (ft)	35000	35000	40000	40000	35000	35000	40000	40000
Total Range (Nm)	1544	1595	1451	1552	1227	1246	1512	1578
Total time (h)	3.86	3.98	3.66	3.91	2.73	2.77	3.38	3.52
Climb Fuel (lb)	541	513	2759	1949	605	566	2529	1584
Climb distance (Nm)	87	81	738	511	105	96	721	425
Time to climb (min)	14	13	113	79	16	15	98	59
Cruise Fuel (lb)	3908	3937	1675	2487	3844	3884	1905	2851
Cruise distance (Nm)	1382	1438	625	953	1045	1073	702	1084
Cruise time (min)	205	214	93	142	136	140	92	139
Descent Fuel (lb)	150	149	165	163	150	149	165	163
Descent distance (Nm)	76	76	89	89	76	76	89	89
Descent time (min)	12	12	13	13	12	12	13	13
ΔRange (Nm)		51		101		19		66
(%)		3.3		7.0		1.6		4.4

Figure 4.14. Mission analysis results - range.

Table 4.9. Mission analysis results - fuel.

|	No WL	WL1545	No WL	WL1545	No WL	WL1545	No WL	WL1545
Takeoff weight (lb)	17227	17122	17402	17109	18196	18123	17289	17152
Distance (Nm)	1200	1200	1200	1200	1200	1200	1200	1200
Cruise Mach	0.7	0.7	0.7	0.7	0.8	0.8	0.8	0.8
Cruise Altitude (ft)	35000	35000	40000	40000	35000	35000	40000	40000
Total time (h)	3.0	3.0	3.0	3.0	2.7	2.7	2.7	2.7
Climb Fuel (lb)	482	458	1861	767	596	554	1518	852
Climb distance (Nm)	76	71	487	162	103	94	410	194
Time to climb (min)	13	12	75	26	16	15	57	28
Cruise Fuel (lb)	2894	2813	1675	2477	3749	3719	1905	2435
Cruise distance (Nm)	1048	1053	624	949	1021	1030	702	917
Cruise time (min)	156	157	93	142	133	134	92	120
Descent Fuel (lb)	150	149	165	163	150	149	165	163
Descent distance (Nm)	76	76	89	89	76	76	89	89
Descent time (min)	12	12	13	13	12	12	13	13
Total Fuel (lb)	3467	3363	3627	3336	4436	4364	3515	3379
ΔFuel (lb)		104		291		72		136
ΔFuel (%)		3.0		8.0		1.6		3.9
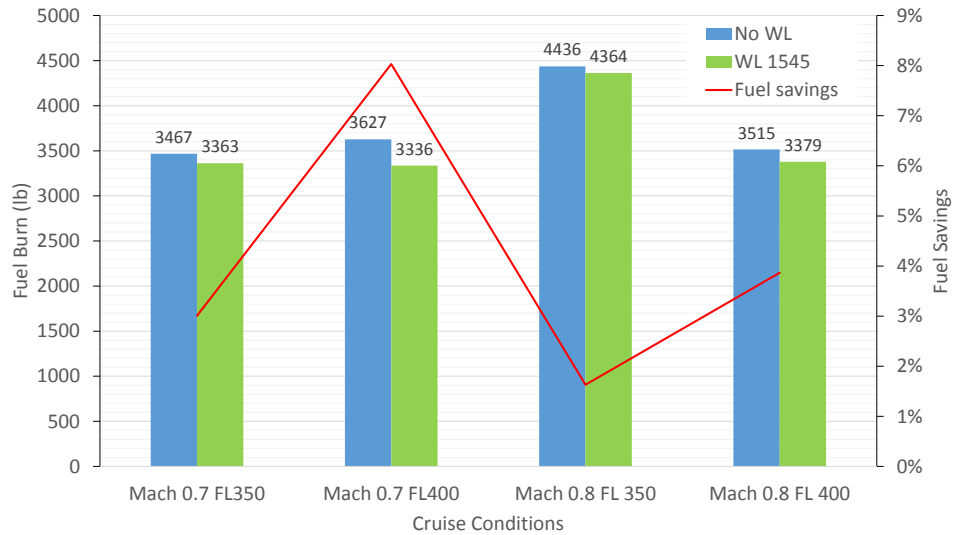
Figure 4.15. Mission analysis results - fuel.

5. Conclusion and Recommendations

The preliminary design of a winglet to improve the performance of the Dassault Falcon 10 aircraft was performed. Based on Whitcomb's design, the final geometry had a 3.2 ft span blended winglet with a cant angle of 45º (Figure 4.8). It is the result of a compromise between the induced drag reduction provided by larger spans and the profile drag increase resulting from larger wetted areas, together with the structural weight increase due to the winglet itself and the wingbox reinforcements due to increased loads.

At the typical cruise lift coefficient, the net drag reduction was 4.8% at Mach 0.7 and 2.5% at Mach 0.8 and the weight increase was estimated to be 127 lb. Thus, when the new aerodynamics and weights are taken into consideration, the range was increased by 66 Nm (4.3%) for a typical mission, cruising at Mach 0.8 at 40,000 ft and carrying 4 passengers with a crew of 2. For a 1200 Nm mission cruising at Mach 0.8 at 40,000ft, the fuel burn is reduced by 3.9%. The maximum range was increased by 3.3% and the minimum fuel burn was reduced by 3.8%.

The analysis included accurate RANS CFD calculations and the reinforcement was determined using FEM. For both instances, the computer models were calibrated with respect to experimental data provided by Dassault. The CFD analysis allowed

to verify that no shockwaves were formed on the winglet before they appeared on the wing.

Although several configurations (in terms of cant and span) were explored, no full fledged optimization was performed.

The FEM analysis revealed that the sideslip condition was critical for the outboard wing in the presence of a winglet, whereas for the baseline wing it was the roll load case. The gust condition is critical for the inboard wing, with and without winglets. However, large structural margins were found in the inboard wingbox such that no reinforcement was necessary for this load case.

Further work should include the structural design of the winglet and a more precise estimation of its weights, including factors such as flutter and fatigue. It is also necessary to study the effects of the winglet on stability and control, both at altitude and in ground effect, and trim drag. It is likely that spanload optimization will further increase the benefit of winglet retrofit.

REFERENCES

Anderson, J. D. (2011). *Fundamentals of aerodynamics* (5th ed.). New York: McGraw-Hill.

ANSYS Fluent user's guide [Computer software manual]. (2011). (Release 14.5)

Avions Marcel Dassault - Breguet Aviation. (1972). *Falcon 10 série, calcul de la voilure première partie.* (Avions Marcel Dassault Technical Report)

Avions Marcel Dassault - Breguet Aviation. (1993). *Falcon 10 operational instructions manual.* (Revision 12)

Bertin, J. J., & Cummings, R. M. (2014). *Aerodynamics for engineers.* Boston, Mass: Pearson.

Büscher, A., Streit, T., & Rohardt, C.-H. (2006). Geometry modifications of nonplanar wing tip design for adaptation to low speed range. In *25th international congress of the aeronautical sciences.*

Cone, C. D. (1962). *The theory of induced lift and minimum induced drag of nonplanar lifting systems* (NASA TR-R-139). NASA.

Faye, R., Laprete, R., & Winter, M. (2002). Blended winglets for improved aircraft performance. In *Aero magazine* (p. 16-31). Boeing.

Hawker 800SP & hawker 800XP2. (2014). Retrieved December 2014 from Aviation Partners Inc. website: http://www.aviationpartners.com/hawker.html.

Huber, M. (2012). *Dassault Falcon 10/100.* Retrieved March 2014, from Business Jet Traveler: http://www.bjtonline.com/business-jet-news/dassault-falcon-10100.

Kroo, I. (2005). Nonplanar wing concepts for increased aircraft efficiency. *VKI lecture series on innovative configurations and advanced concepts for future civil aircraft.*

Mann, A. (2006). The modelling and design of advanced wing tip devices. In *Aeronautics Days 2006 in Vienna.*

McCormick, B. W. (1995). *Aerodynamics, aeronautics, and flight mechanics.* New York: Wiley.

McLean, D. (2005). Wingtip devices: What they do and how they do it. *Performance and Flight Operations Engineering Conference.*

Munk, M. M. (1921). *The minimum induced drag of aerofoils* (NACA Report 121). NACA.

Mystère-Falcon 10-100. (2015). Retrieved March 2015, from Dassault Aviation website: http://www.dassault-aviation.com/en/passion/aircraft/civil-dassault-aircraft/mystere-falcon-10-100/.

Nicolai, L. M., & Carichner, G. (2010). *Fundamentals of aircraft and airship design.* Reston, VA: American Institute of Aeronautics and Astronautics.

Niu, M. C.-Y. (1999). *Airframe stress analysis and sizing* (2nd ed.). Los Angeles, Calif; Hong Kong: Conmilit Press Ltd.

Niu, M. C.-Y. (2006). *Airframe structural design : practical design information and data on aircraft structures.* Los Angeles, Calif; Hong Kong: Conmilit Press Ltd.

Poisson-Quinton, P. (1985). Parasitic and interference drag prediction and reduction [AGARD Report No.723]. In *Aircraft drag prediction and reduction.*

Rademacher, P. R. (2014). *Winglet performance evaluation through the vortex lattice method* (Unpublished master's thesis). Embry-Riddle Aeronautical University.

Shollenberger, C. A., Humphreys, J. W., Heiberger, F. S., & Pearson, R. M. (1983). *Results of winglet development studies for dc-10 derivatives* (NASA CR-3677). NASA.

Takenaka, K., Hatanaka, K., Yamazaki, W., & Nakahashi, K. (2008). Multidisciplinary design exploration for a winglet. *Journal of Aircraft, 45*(5).

Taylor, A. B. (1983). *Dc-10 winglet flight evaluation summary report* (NASA CR-3748). NASA.

Thomas, A. S. (1985). Aircraft drag reduction technology - a summary [AGARD Report No.723]. In *Aircraft drag prediction and reduction.*

Torenbeek, E. (2013). *Advanced aircraft design: Conceptual design, technology and optimization of subsonic civil airplanes.* Chichester, West Sussex, United Kingdom: John Wiley & Sons Inc.

van Dam, C. (1987). Induced drag characteristics of crescent-moon-shaped wings. *Journal of Aircraft, 24*(2).

Vassberg, J. C., DeHaan, M. A., & Sclafani, T. J. (2003). Grid generation requirements for accurate drag predictions based on overflow calculations. In *16th AIAA computational fluid dynamics conference.*

Whitcomb, R. T. (1976). *A design approach and selected wind-tunnel results at high subsonic speeds for wing-tip mounted winglets* (NASA TN-D-8260). NASA.

Wingtip fence Airbus A320. (2014). Retrieved March 2015, from Wikimedia Commons: http://commons.wikimedia.org/wiki/File:Wingtip_Fence_Airbus_A320.JPG.

A. Engine Data

The data for the Falcon 10 TFE731-2 engines was scaled from the TFE731-1069
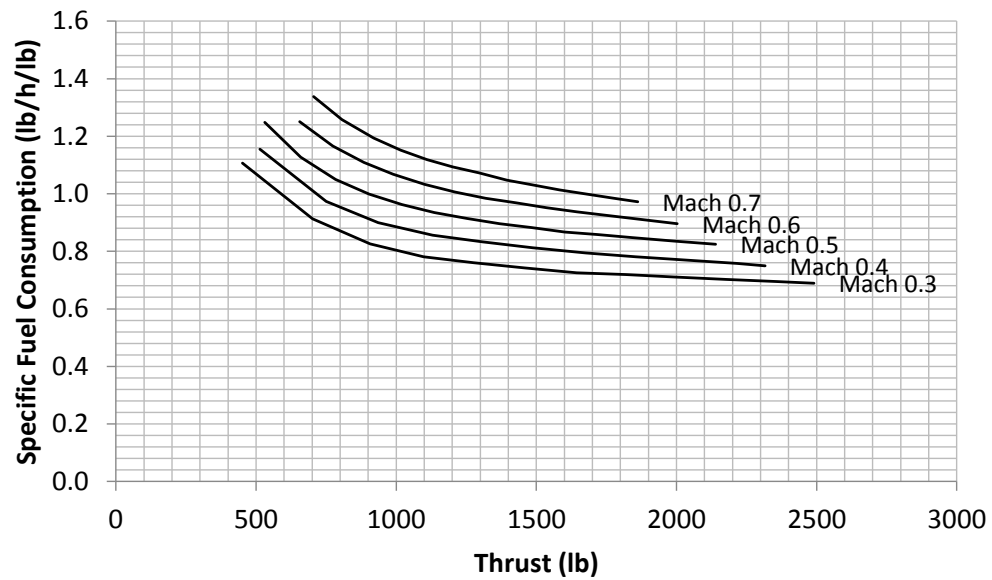engine data available (Nicolai & Carichner, 2010).

Figure A.1. TFE731-2 data at standard sea level (adapted from Nico-
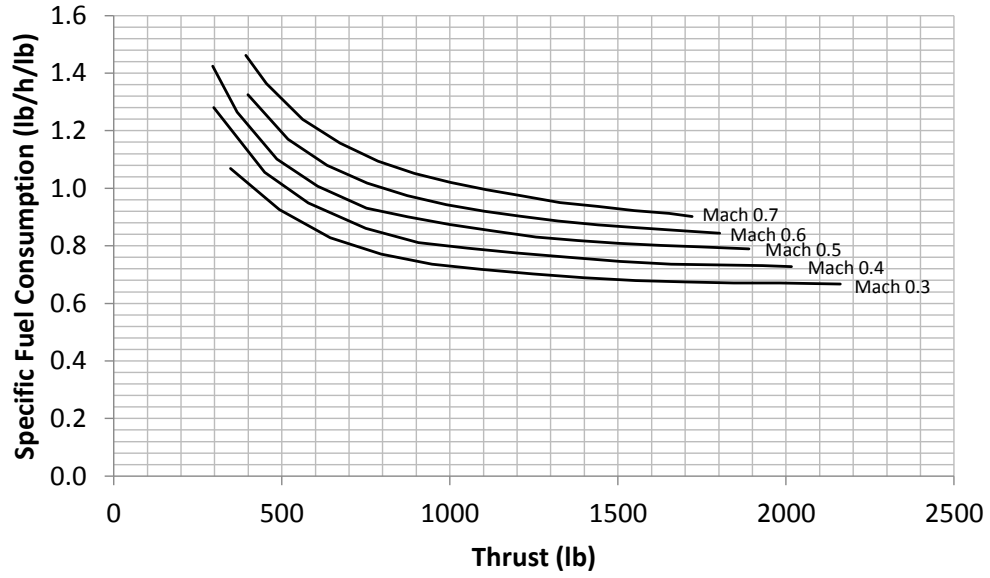lai & Carichner, 2010).

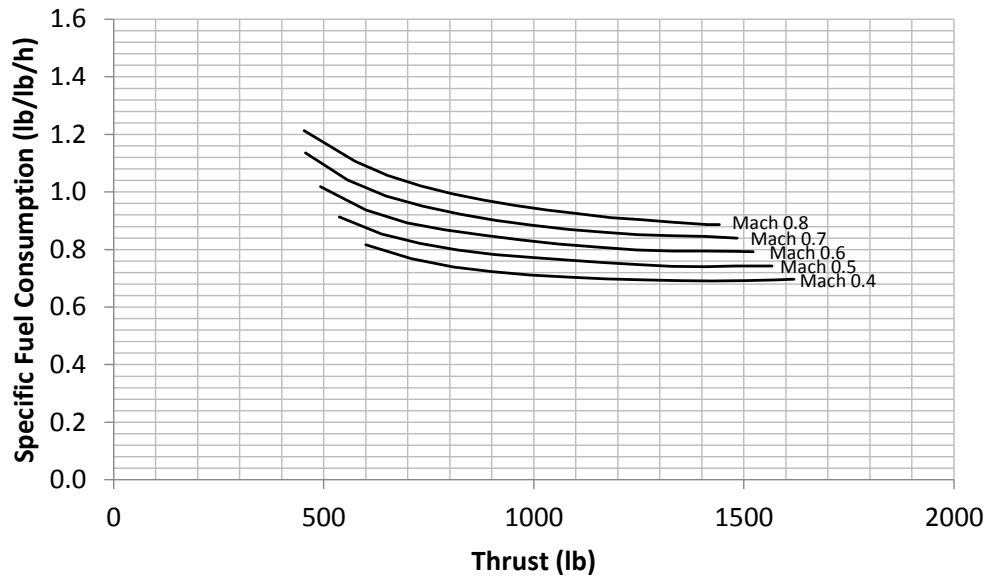Figure A.2. TFE731-2 data at 10,000 ft (adapted from Nicolai & Carichner, 2010).

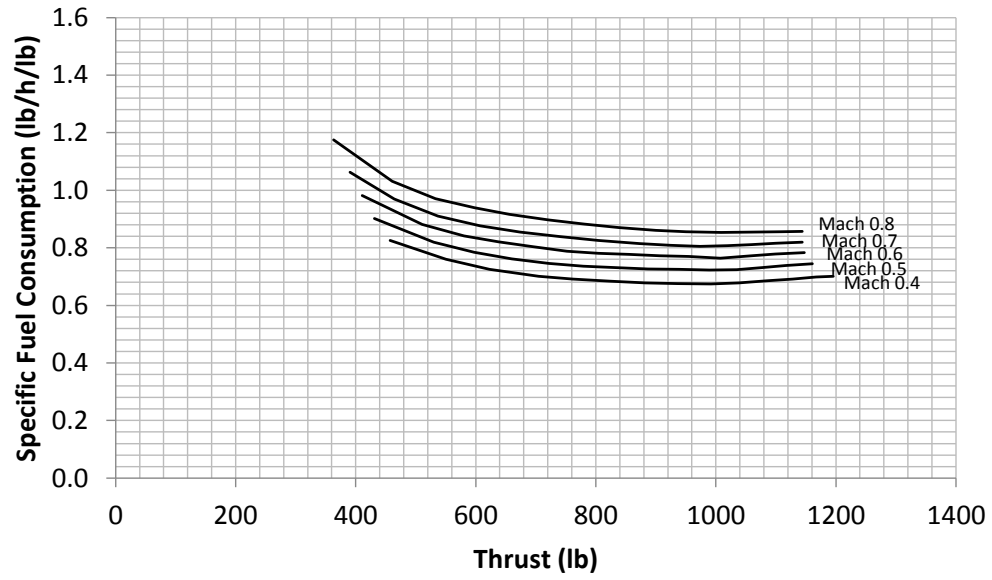Figure A.3. TFE731-2 data at 20,000 ft (adapted from Nicolai & Carichner, 2010).

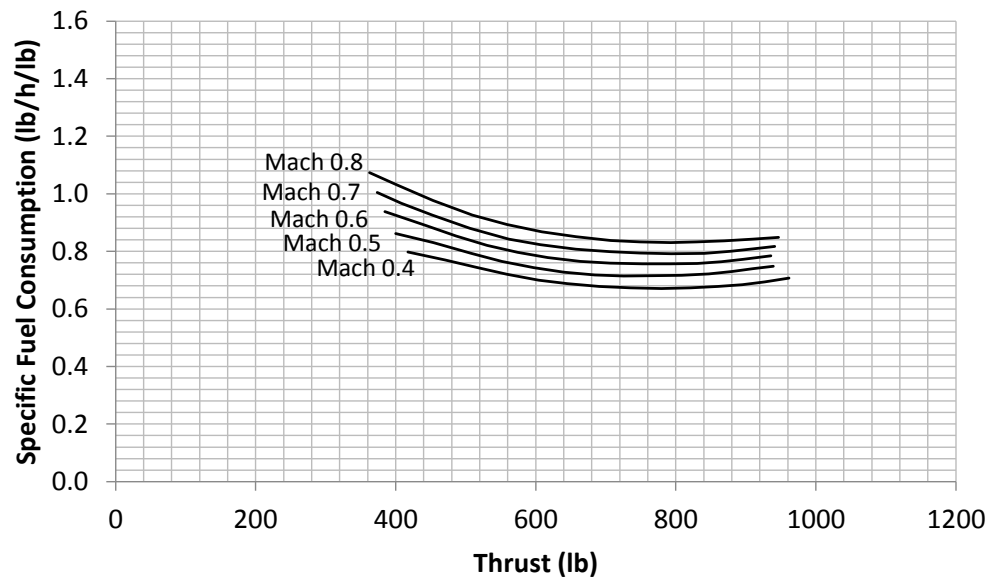Figure A.4. TFE731-2 data at 30,000 ft (adapted from Nicolai & Carichner, 2010).

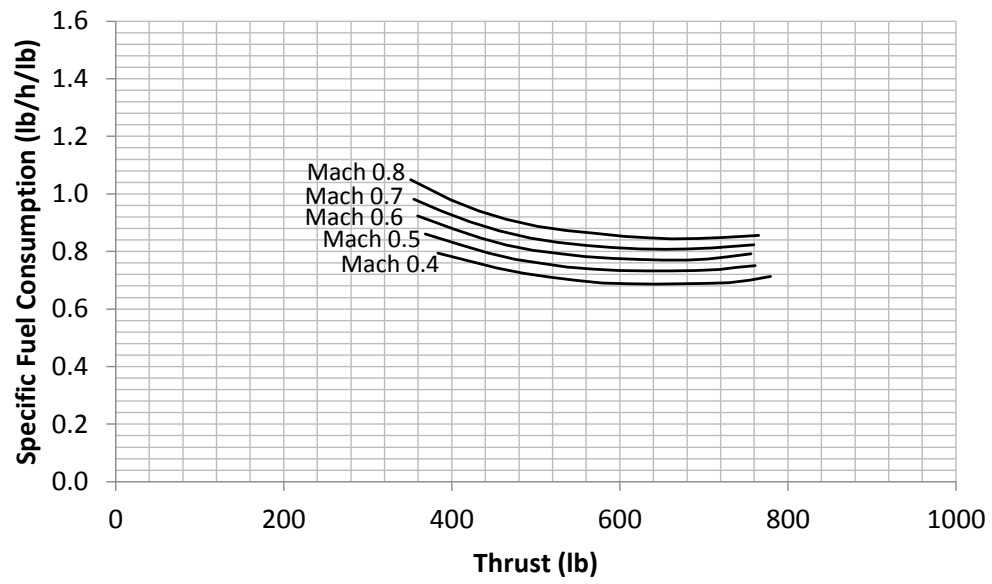Figure A.5. TFE731-2 data at 36,089 ft (adapted from Nicolai & Carichner, 2010).

Figure A.6. TFE731-2 data at 40,000 ft (adapted from Nicolai & Carichner, 2010).